NASA CONTRACTOR
REPORT

NASA CR-1339

AERODYNAMIC EFFECTS
OF BULBOUS BASES

by Lars E. Ericsson and J. Peter Reding

0060513

NASA CR-1339

AERODYNAMIC EFFECTS OF BULBOUS BASES

By Lars E. Ericsson and J. Peter Reding

Distribution of this report is provided in the interest of information exchange. Responsibility for the contents resides in the author or organization that prepared it.

Issued by Originator as LMSC Report No. 4-17-68-4

NATIONAL AERONAUTICS AND SPACE ADMINISTRATION

ABSTRACT

An exploratory study has been made of the effect that a bulbous base can have on the aerodynamic characteristics of blunt space capsules and slender reentry bodies. It is found that the base has a profound effect and can cause drastic loss of dynamic stability. A careful examination of available experimental data reveals that the often complex effects of bulbous bases can be explained using quasi-steady separated flow concepts. In general, a bulbous base adversely affects the vehicle dynamics but increases the static stability. Support interference is a serious problem that can prevent simulation in dynamic wind tunnel tests of full-scale vehicle dynamics. A possible means of measuring and correcting for this dynamic sting interference is outlined.

CONTENTS

FIGURES

vii

SUMMARY

A study of the aerodynamic characteristics of blunt and slender reentry vehicles has revealed that a bulbous base can have a profound effect and seriously degrade the vehicle dynamics. On a blunt reentry capsule, the undamping effects are realized when the wake from the forebody at high supersonic speeds starts to reattach on the bulbous base. On a slender reentry vehicle, the undamping effects of a rounded base are realized mainly at subsonic and transonic speeds through upstream communication effects from the wake recompression region. Model support interference is found to be a serious problem in dynamic wind tunnel tests.

1

Section 1

INTRODUCTION

Bulbous bases are a rather common characteristic of the modern reentry vehicles. The reentry capsules used in the civil space program usually comprise a blunt heat shield in the wake of which the valuable payload is shielded and supposedly completely hidden from a hostile environment. On the more slender reentry configurations used for military applications, convex rounded bases are used for other equally compelling reasons. Although it is true that the bulbous base in some cases may have little effect on the static characteristics (Ref. 1), it has been demonstrated repeatedly that the bulbous base still can have drastic effects on the vehicle dynamics, causing undamping in pitch (Refs. 2, 3, and 4) and a reentry characterized by circular limit-cycle oscillations (Ref. 5). In the present report, available experimental data on reentry vehicles with bulbous bases are examined. A conceptual flow picture is constructed and analytic relationships between dynamic and static characteristics are developed using quasi-steady concepts for unsteady separated flow.

Section 2

DISCUSSION

The transonic flow over a reentry vehicle with a composite bulbous base is sketched in Fig. 1. The flow separates first at the cone shoulder and reattaches on the conical boat tail before it again separates off of the rounded base to form the body wake. Two different types of forces induced by the separated flow are: (1) a force due to differential reattachment on the boat tail of the separated flow from the cone shoulder, and (2) a force due to differential (top and bottom) reseparation off the rounded base. Two examples of the reattaching flows are shown in the top insets of Fig. 1, viz., nose-induced separation on a blunt cylindrical body at transonic speeds and reattachment on the boat tail aft of a blunt forebody at supersonic speeds. A good example of differential separation off a rounded base is provided by the flow over a slender cone with bulbous base as shown in the bottom inset of Fig. 1.

2.1 FLOW REATTACHMENT EFFECTS

Probably the best known of the separated flow patterns as far as its dynamic effects are concerned is the nose-induced separation. The steady and unsteady aerodynamic characteristics of nose-induced separation have been described in Refs. 6, 7, and 8. Figure 2 illustrates how the separated flow pattern causes highly nonlinear aerodynamic characteristics at $M = 0.9$, and Fig. 3 shows the Mach number dependence of pitch damping and aerodynamic stiffness. A nonflared blunt-faced cylinder exhibits the same type of characteristics (Fig. 4 and Refs. 2, 9, and 10). These figures (Figs. 2, 3, and 4) illustrate the "signature" of nose-induced separation, viz:

- It is a subsonic flow phenomenon.
- It causes a large increase in static stability with a correspondingly larger decrease in dynamic stability usually resulting in dynamic instability.
- The effects are highly nonlinear and disappear fast for increased angle of attack and/or oscillation amplitude.

5
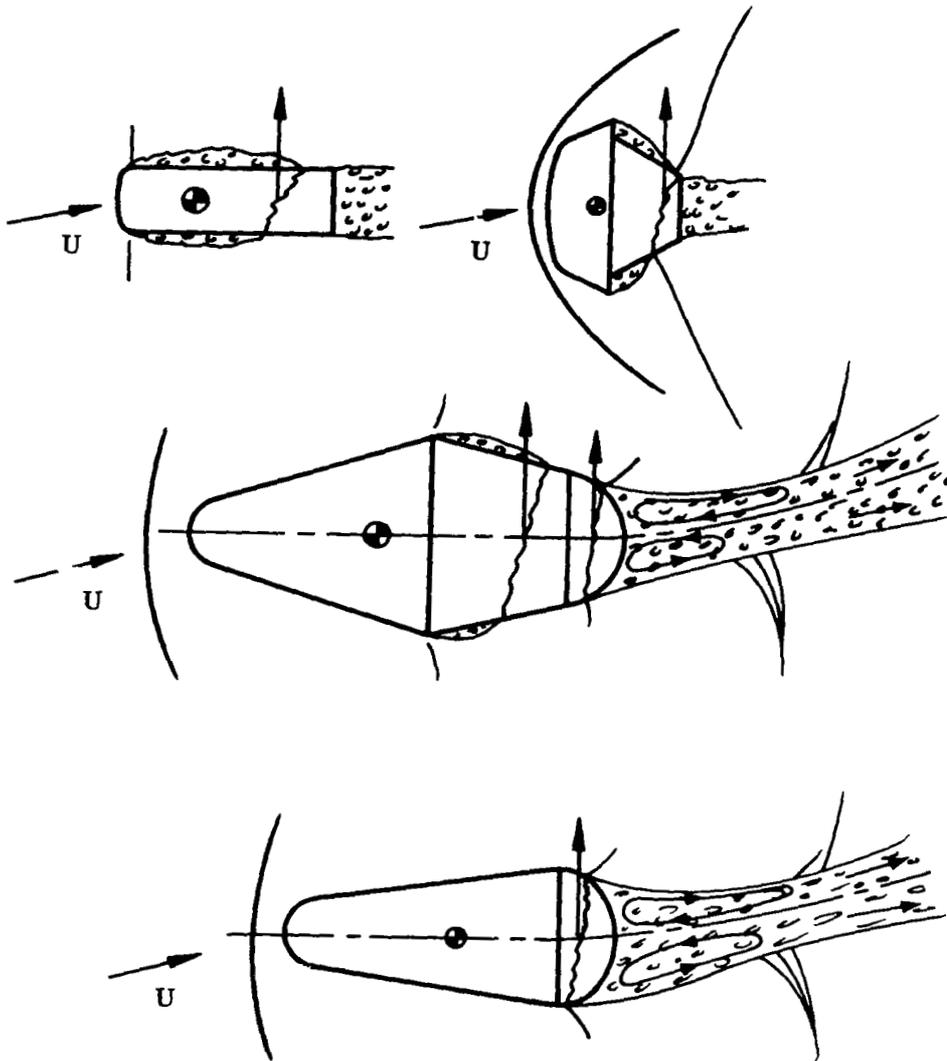
Fig. 1 Flow Over Bodies With Bulbous Bases
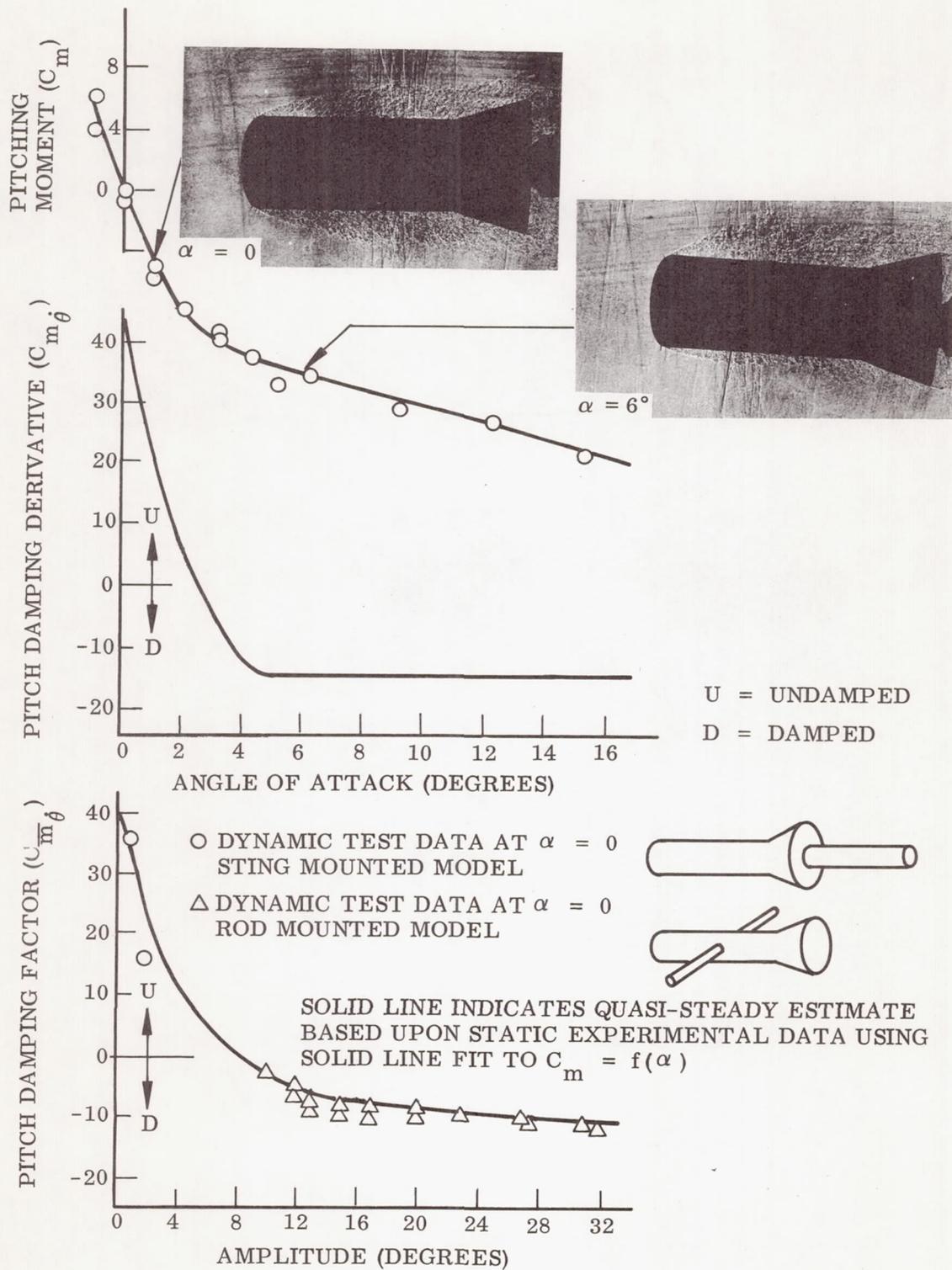
Fig. 2 Aerodynamic Characteristics of a Blunt Cylinder — Flare Body
With Nose Induced Separation at M = 0.9
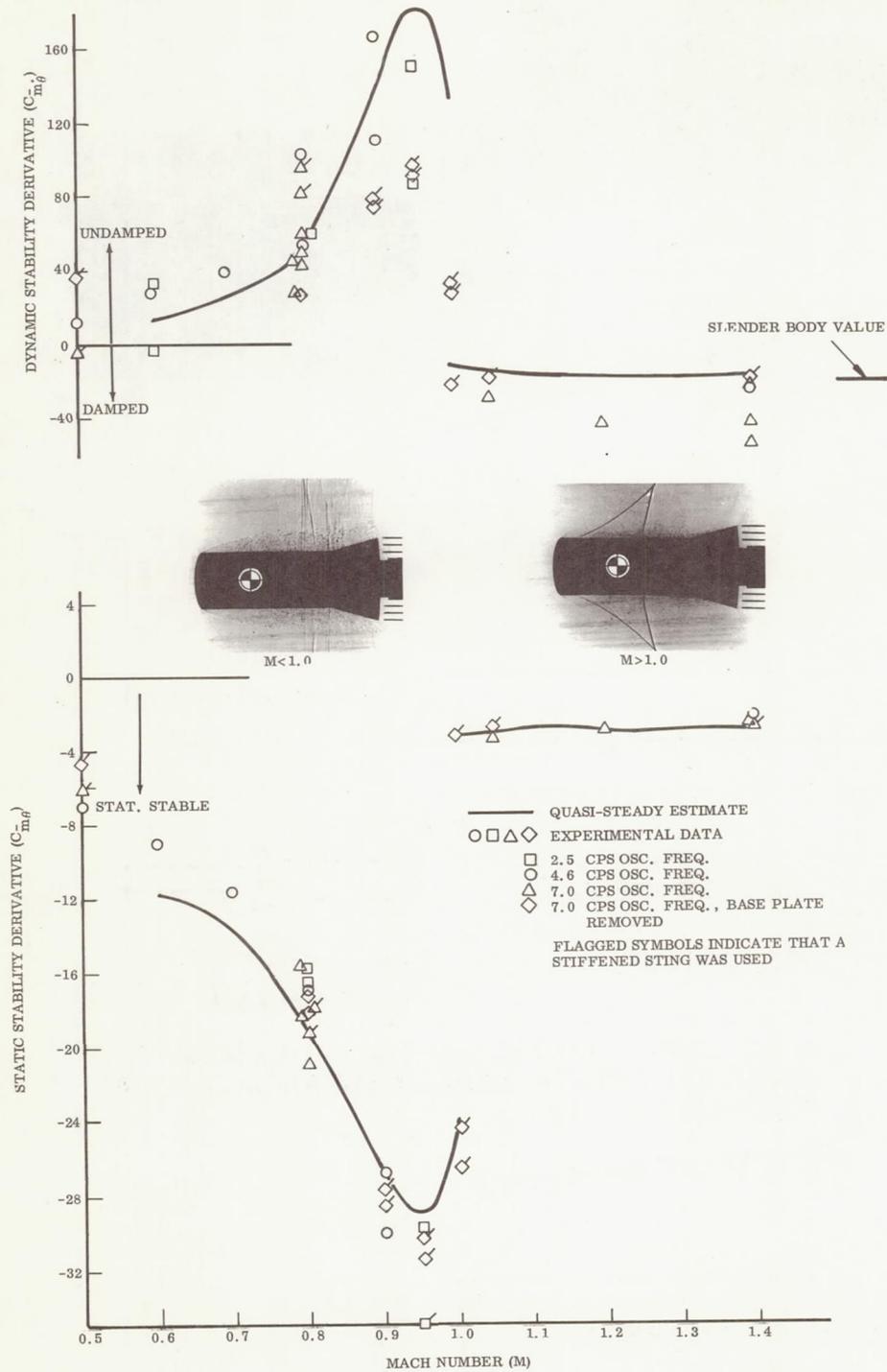
Fig. 3 Oscillatory Derivatives of a Blunt Cylinder — Flare Body
for 1.0-deg Amplitude Oscillations Around $\alpha = 0$

8
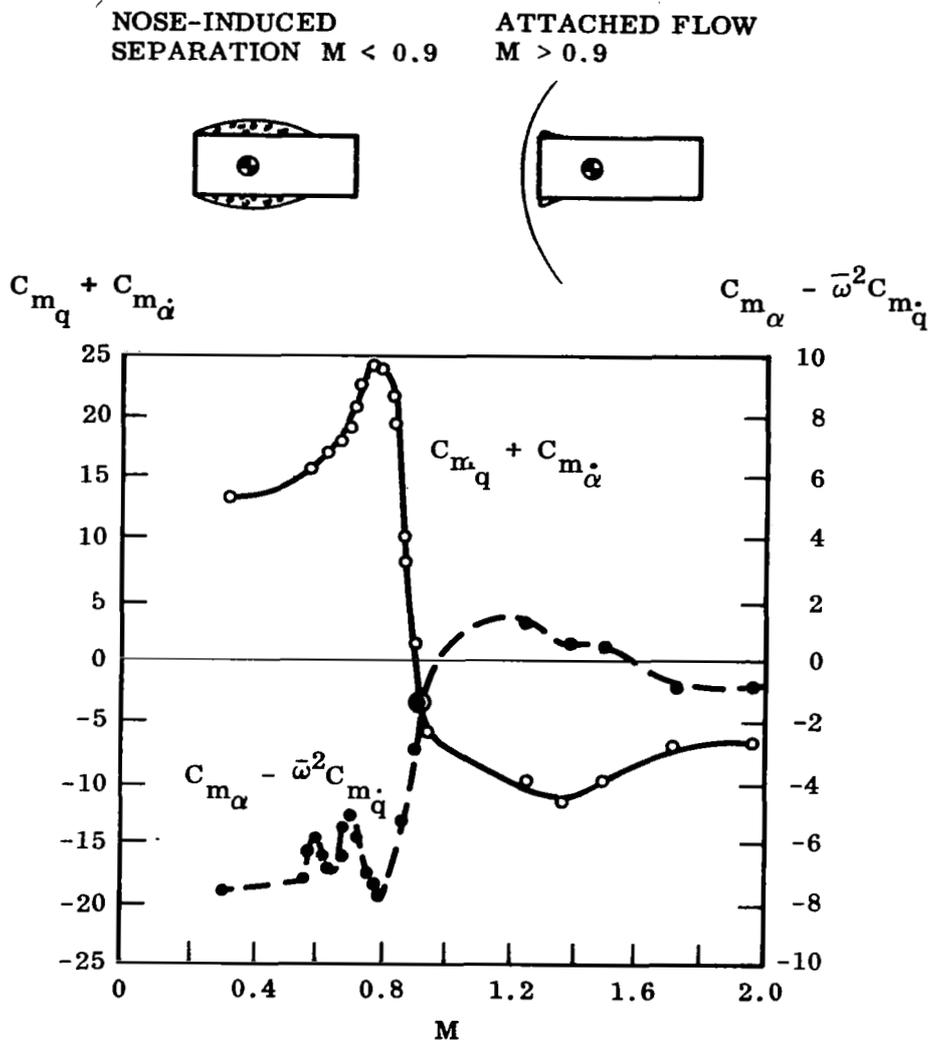
Fig. 4 Oscillatory Derivatives of a Flat Face Cylinder for 1.5-deg
Amplitude Oscillations Around $\alpha = 0$

9

The reversal between static and dynamic effects of the separation induced loads is due to time lag as has been described repeatedly in the past (e.g., Refs. 6, 7, and 8). That is, the separation induced force on the aft body at a certain time t is dependent upon the crossflow at the separation source, i.e., the nose, at an earlier time instant $t - \Delta t$. This means that when the body returns to zero angle of pitch, it has a residual force generated at an earlier time instant. If the separation induced force is statically stabilizing (i.e., increasing the aerodynamic spring), the residual spring effect will continue to drive the motion at zero pitch angle and an undamping effect results* (Fig. 5).

At supersonic speeds flow reattachment occurs on the aft body of the Mercury capsule (Ref. 11) resulting in dynamic instability and divergent oscillations (Fig. 6). On a similar blunt reentry capsule (Refs. 12 and 13), the wake converges with increasing Mach number until it reattaches on the cylindrical tail, resulting in increased aerodynamic spring and decreased damping, ultimately leading to dynamic instability at high Mach numbers (Fig. 7a). Similarly, for increasing angle of attack at constant Mach number, the windward side wake is pushed towards the aft body until wake impingement occurs, and increased static and decreased dynamic stability again results (Fig. 7b). If the aft body is flared (Refs. 14 and 15), the wake impingement occurs at all supersonic Mach numbers resulting in a dynamically unstable vehicle with a very large static stability margin (Fig. 7a). At low speeds, the wake generated by the blunt nose is not converging enough to reattach on the flare-end of the contracted aft body (Ref. 16)**. Even a pure boat tail, a truncated cone without cylindrical or flared tail end, will experience wake impingement when the Mach number is increased from subsonic (Ref. 16) to supersonic (Refs. 14 and 15) and the corresponding drastic changes of the stability derivatives occur (Fig. 8a). When the boat tail cone angle is

---

*It may be worth emphasizing that doubling the separation induced flare force, e.g., by increasing the flare size, will double both the statically stabilizing and the dynamically destabilizing effects of the nose-induced separation.
**Instead, the uncontracted "all-flare body" experiences the full effects of nose-induced separation.

$\alpha_{\text{static}} = 0; \quad q = 0$

$\Delta^i C_N$

$\alpha(t - \Delta t)$

U

$\alpha_{\text{static}} = \alpha(t - \Delta t); q = 0$

$\Delta^i C_N$

$-q$

U

$\alpha(t) = 0; q < 0$
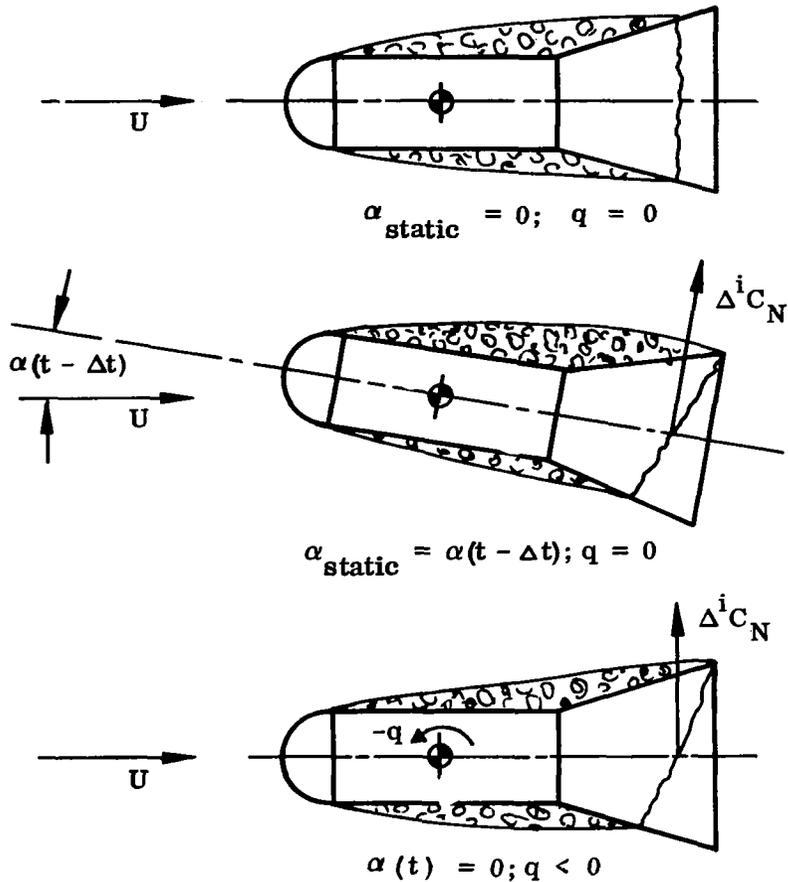
α DECREASED FROM $\alpha(t - \Delta t)$ to $\alpha = 0$
(Δt IS THE TIME REQUIRED FOR THE NOSE-INDUCED
SEPARATION TO TRAVEL FROM NOSE TO FLARE)

Fig. 5 Steady and Unsteady Flow Patterns of Nose
Induced Separation

11
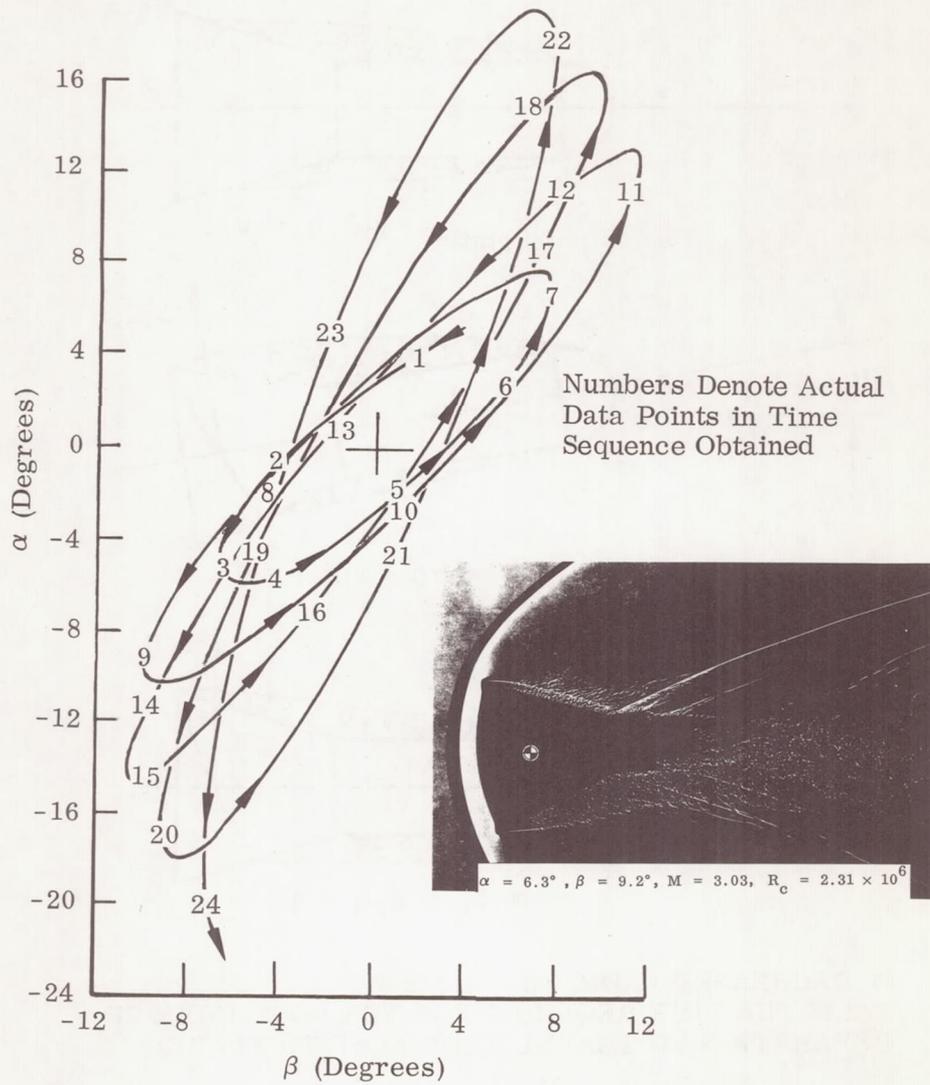
Fig. 6 Pitching and Yawing Motion of Mercury Capsule Model at
$2.53 \leq M \leq 3.14$, $1.88 \leq R_c \times 10^{-6} \leq 2.34$

12

a) $\Delta \alpha = 1.2°$, $\alpha = 0$

b) $M = 2.91$
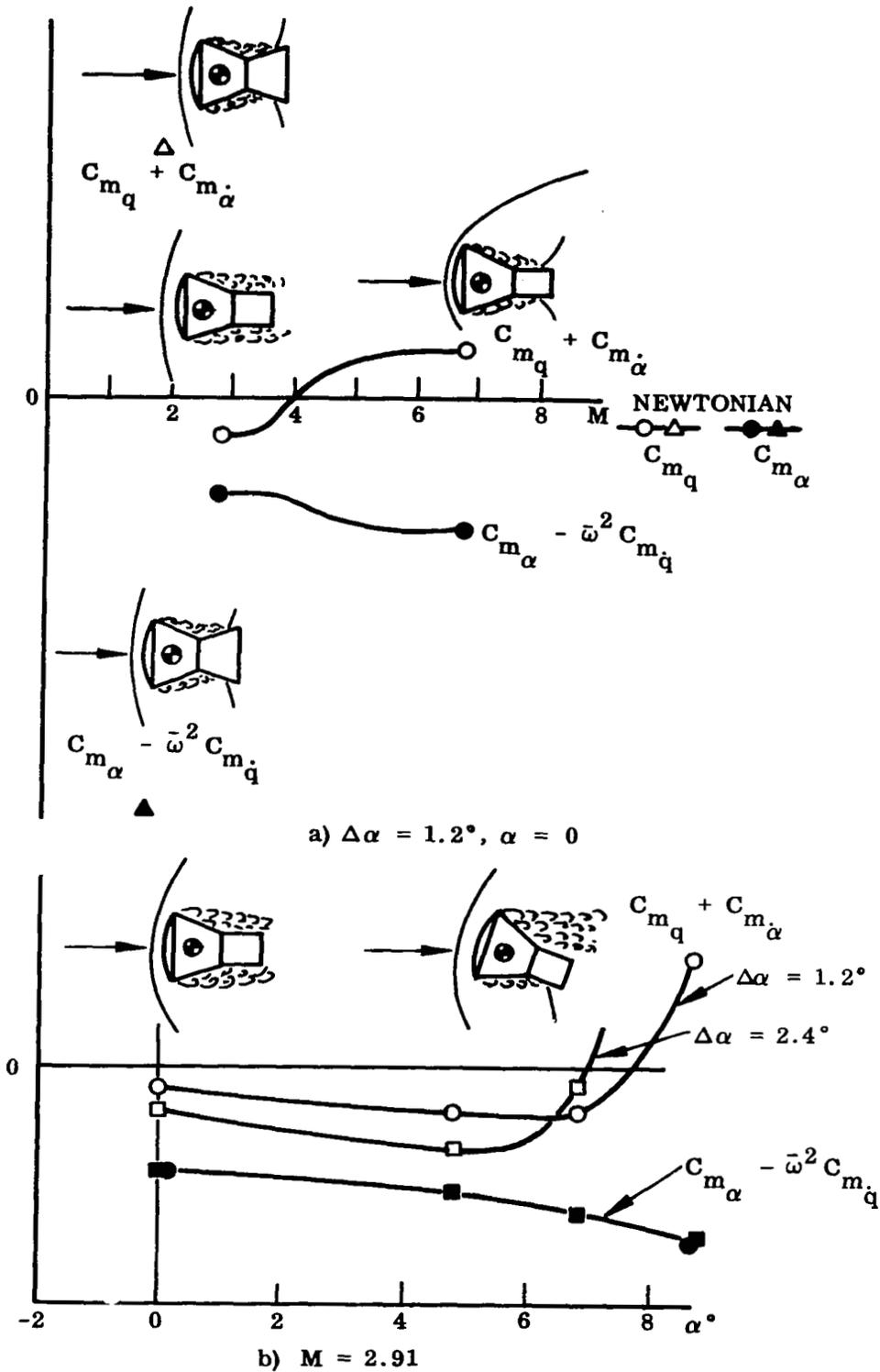
Fig. 7 Oscillatory Derivatives of a Blunt Reentry Capsule as Functions of Amplitude, Angle-of-Attack, and Mach Number ($R_c \approx 0.6 \times 10^6$)

13
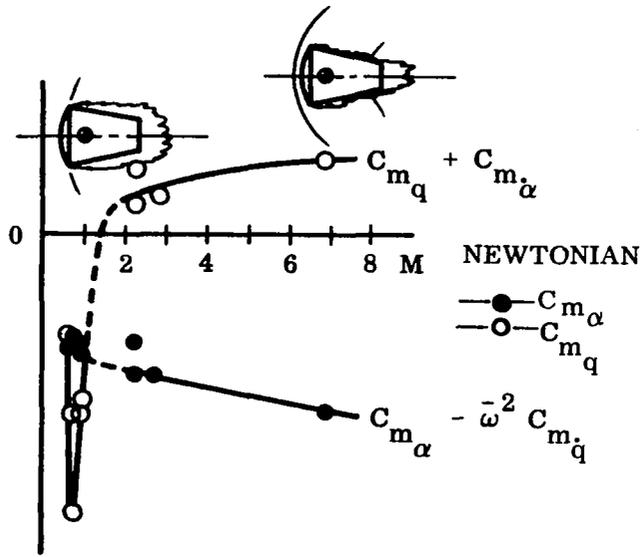
a) Boat-Tailed Spherical Segment
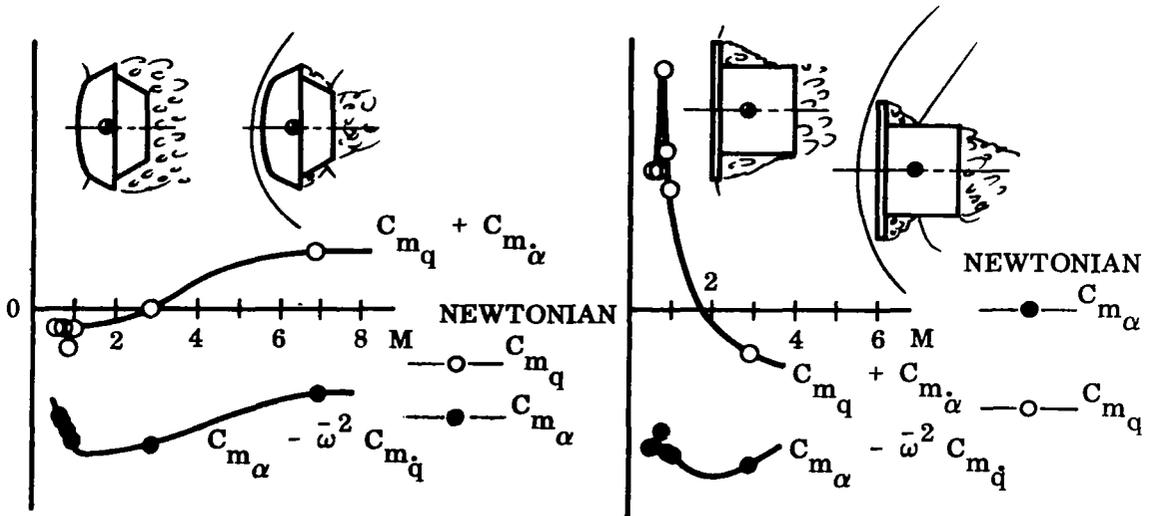
b) Blunt Body with Stepped Down Boat Tail

c) Flat Face Disk with Stepped Down Cylindrical Afterbody

Fig. 8 Oscillatory Derivatives of Blunt Bodies for 2-deg Amplitude Oscillations Around $\alpha = 0$ ($R_c \approx 0.6 \times 10^6$)

increased, only windward side wake impingement can occur at low supersonic Mach numbers (Ref. 17). However, if the boat tail is stepped down from the forebody (Refs. 14, 15, and 16), the wake attachment occurs at $\alpha = 0$ already at low supersonic speeds (Fig. 8b) and for some geometries even at subsonic speeds (Fig. 8c). In the latter case the undamping decreases with increasing Mach number as the wake impingement moves upstream over the base towards the oscillation center, until finally, when the Mach number is high enough, the undamping due to wake impingement is not sufficient to cancel the forebody (flat face) damping and the body becomes damped. If the stepped-down aft body is very short, however, it has no effect at subsonic speeds (Ref. 18).

The supersonic wake impingement on a bulbous base produces the same nonlinear aerodynamic characteristics (Fig. 9 and Ref. 19) as the subsonic nose-induced separation on blunt cylinder-flare bodies (Fig. 2 and Ref. 6). The effect of oscillation-center location is also the same (Ref. 19) as for nose-induced separation (Refs. 6, 7, and 8). That is, the undamping increases when the oscillation center moves back of the wake source, due to the addition of mechanical phase lag to the time-lag effect (Ref. 7). Beam and Hedstrom (Ref. 19) also investigated what effect yaw angle had on the oscillation in pitch (Fig. 9). At relatively small angles of yaw, the leeward side is blanked, i.e., no wake attachment occurs, and the windward side experiences full-wake impingement. The result is that the top and bottom portions of the aft body have a flow that is rather insensitive to pitch oscillations once the yaw angle has exceeded a certain value. It appears that this critical yaw angle, β_L, which eliminates the nonlinear boat tail effect, is of the same magnitude as the critical angle of attack, α_L. That is, in free flight the body shown in Fig. 9 would describe a circular motion with an absolute angular envelope $|\alpha + i\beta|$ of approximately 2 deg at $M = 3.5$ and maybe 3 to 4 deg at $M = 2.5$. These are minimum values; i.e., circular limit-cycle amplitudes that are obtainable only if the body flies at a constant Mach number long enough. Before that limit is reached, the body could reach amplitudes in planar motion that are almost an order of magnitude larger (Ref. 6). The trend towards increasing undamping for decreasing Mach number would tend to aggravate the oscillations of a reentering vehicle, and large amplitude oscillations could be expected.

Numbers Denote Actual Data
Points in Time Sequence Obtained
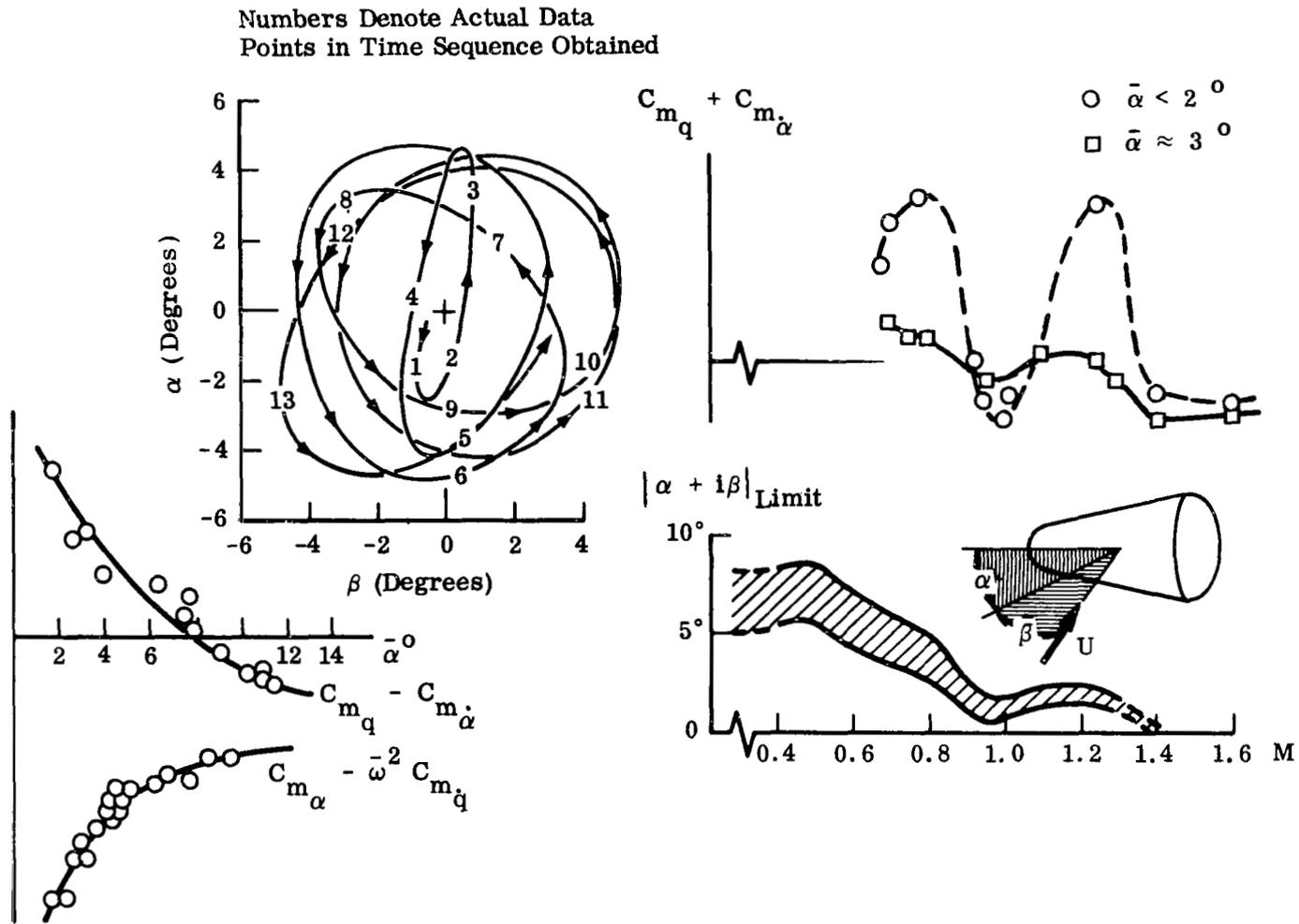
Fig. 10 Ballistic Range Data for a Slender Cone With Rounded Base

18
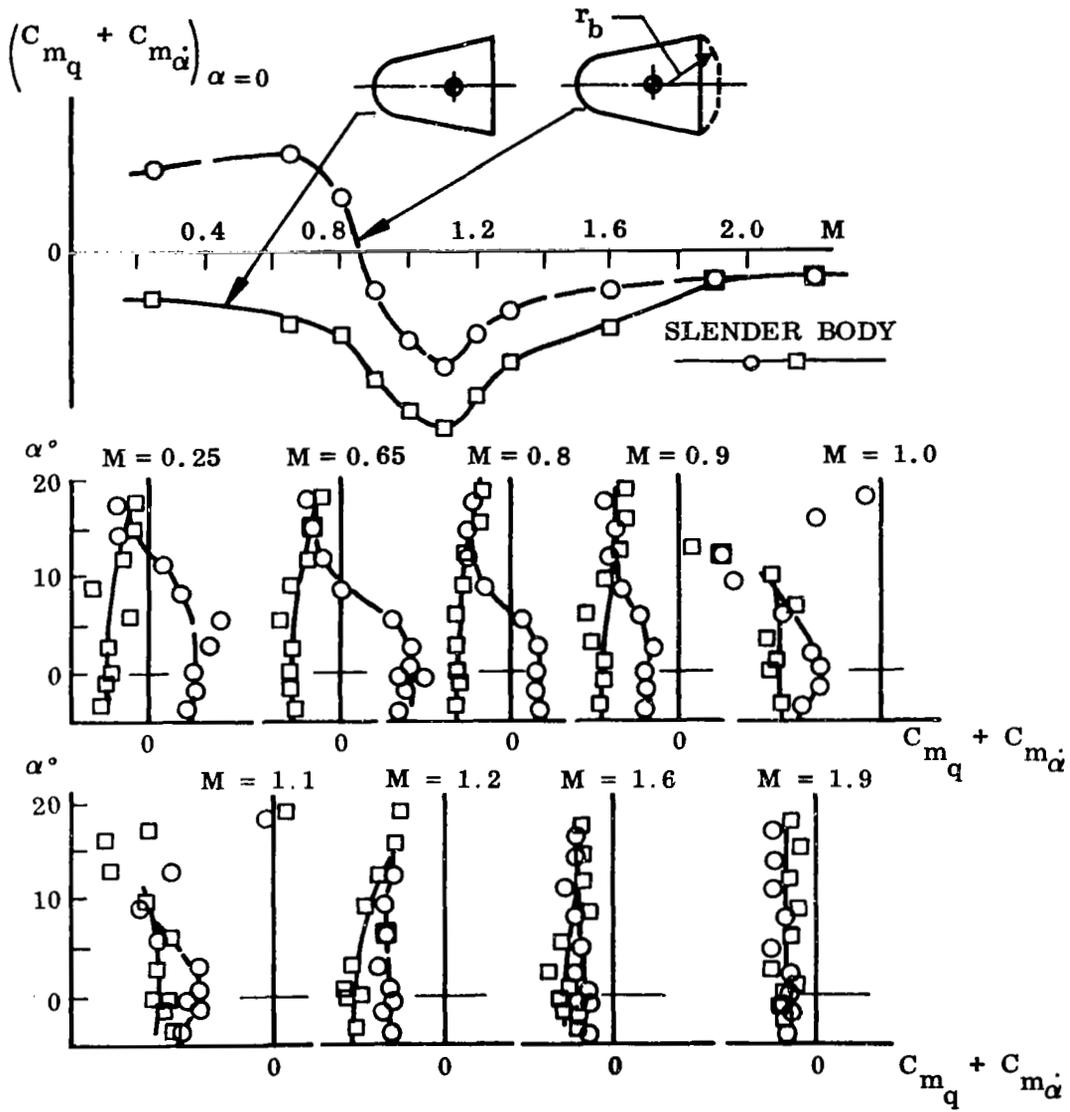
Fig. 11 Effect of Rounded Base on the Pitch Damping of
a Blunted Cone for 3.5-deg Amplitude Oscillations

- Causing increased static stability with a correspondingly large decrease of dynamic stability usually resulting in dynamic instability.
- Highly nonlinear and disappears fast for increased angle of attack and/or oscillation amplitude.

Hence, the reversal between dynamic and static effects of base roundness is almost certainly due to time lag effects.

2.2.1 Forces Induced on the Bulbous Base

Surprisingly enough, the induced load on the rounded base must be positive to supply the observed static-stability increment. This is, of course, in opposition to the usual attached-flow boat tail effect. The results of some recent exploratory tests conducted by Lockheed indicate that the load on the rounded base is indeed positive (Fig. 12).*
It is also apparent from these data that there is a large sting interference effect. Oddly enough, the sting effect furnishes the first clue to the aerodynamic phenomenon responsible for the observed base effect.

The sting induces a positive normal force on the rounded base by affecting the location of the wake separation point. When the sting is pitched, there is an increase in the strength of the windward-side wake-recompression pressure which, in turn, increases the return mass flow rate and causes a forward movement of the windward-side separation point. Opposite effects occur on the leeward side and, as a result, a positive load is induced on the base (Fig. 13a). Similar reasoning can be used to explain the positive base load for a free wake. The lift developed over the forebody initially directs the wake downward. Because the wake is eventually swept back in the direction of the free-stream velocity vector, a transverse pressure gradient is established in the wake to accomplish the turning. This pressure gradient produces a difference in the windward-to-leeward side wake-recompression pressure, causing a positive force to be induced on the base (Fig. 13b) in the same manner as for the sting-mounted body. The sting is capable of sustaining a larger normal pressure differential than is the free wake, thus explaining the greater base force on the sting-mounted bodies.

_____

*The M = 1.5 data points in Fig. 12 may be in error as the result of wind tunnel wall interference.
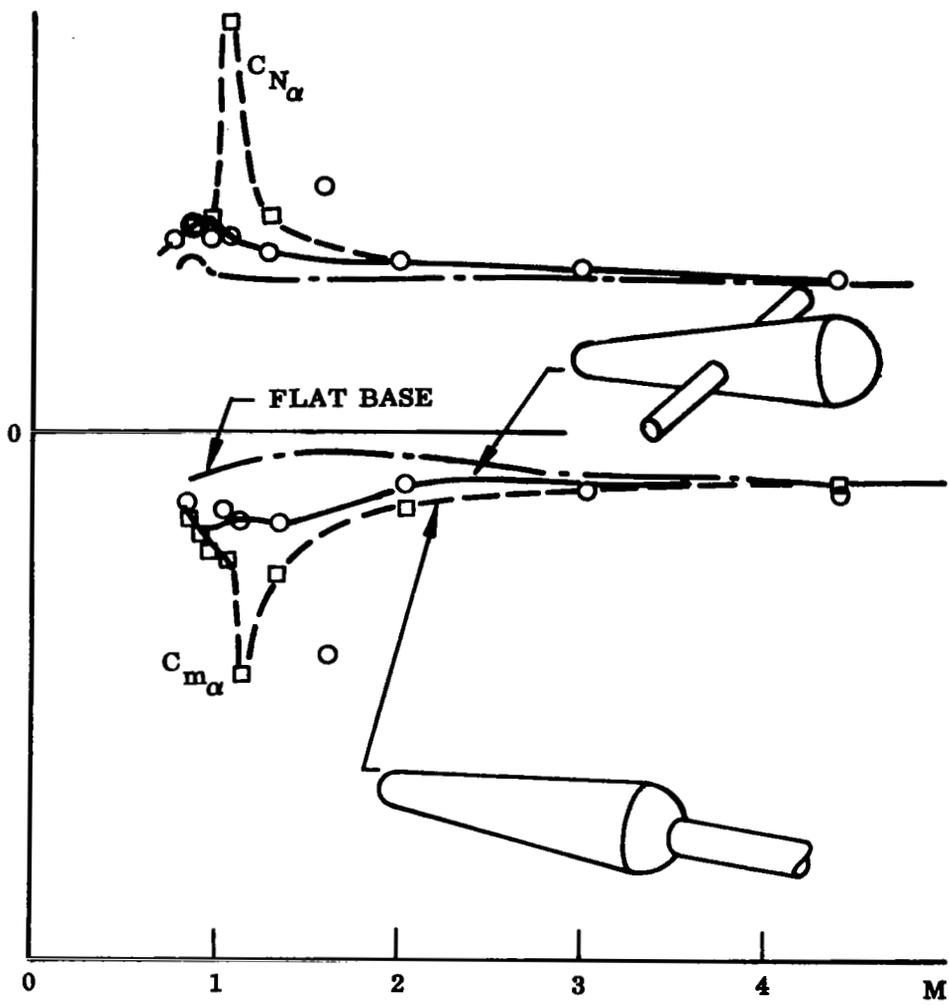
Fig. 12 Static Derivatives at $\alpha = 0$ of a Slender Cone With Hemispherical Base

21

a) Sting Supported Wake

$$\Delta^i C_{N_{STS}} + \Delta^i C_{N_u}$$

b) Free Wake

$$\Delta^i C_{N_u}$$
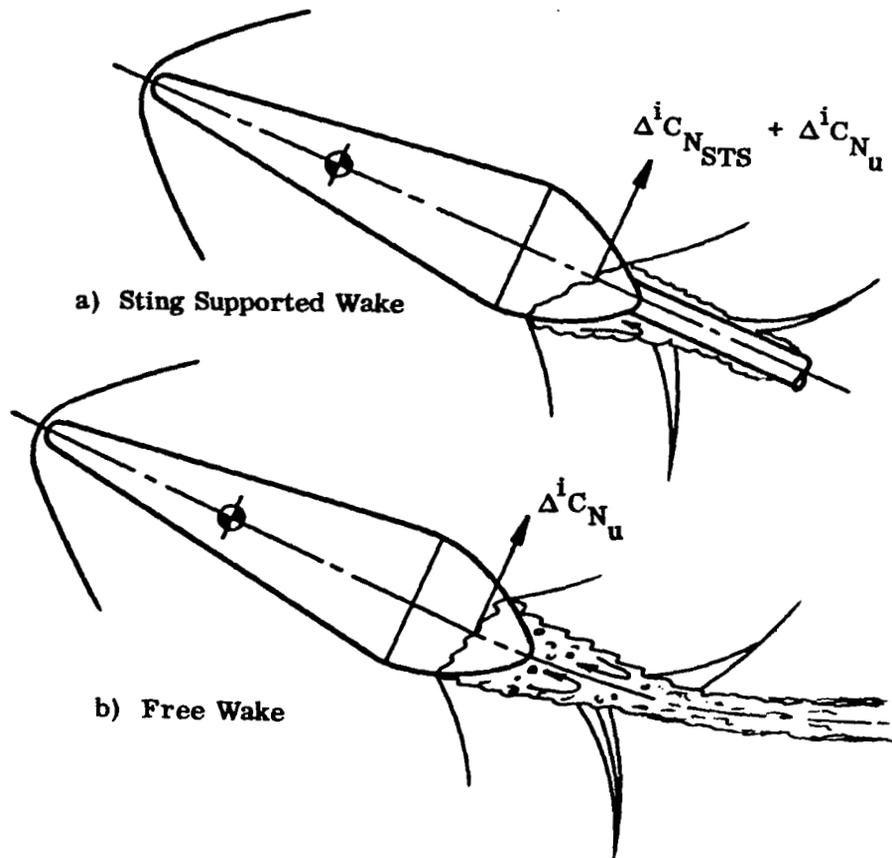
Fig. 13 Forces Induced on a Large Bulbous Base Through Upstream Communication From Wake Recompression Region

22

The shadowgraph and flow sketch in Fig. 14* not only substantiate that the windward-side wake-recompression shock is strengthened, but shows also that it is closer to the base, thus further facilitating the windward-side upstream communication.

It is obvious that a time lag will occur between the instant that the body is perturbed and the resulting change in the separation location takes place. This time lag can be large as it involves propagation downstream to the wake neck and return (back to the base) through the low-velocity wake recirculation region.** The residual force that results from the time lag will cause the statically-stabilizing upstream communication load to produce the undamping (compare with Fig. 5) observed experimentally (Fig. 15).

In addition to these upstream effects of the wake recompression (Fig. 16a), forebody crossflow also influences the base load (Fig. 16b). Forebody crossflow acts to thicken and weaken the leeward boundary layer through collection of low-energy fluid swept from the windward side. Simultaneously, the windward boundary layer is thinned and strengthened. The resulting promotion of separation on the leeward side and reduction on the windward side generates a negative induced base load, i.e., $\Delta^i C_N < 0$ (Fig. 16b). These two opposing effects vary in relative importance such that the wake effects dominate at one Mach number and forebody crossflow effects dominate at another (Fig. 17).***

The drastic variation of the aerodynamic effects of the bulbous base between $M = 0.8$ and $M = 1.2$ (Fig. 17) can be explained as follows: Figure 18 shows how the base pressure and minimum surface pressure on slender cones and cone-cylinder bodies vary with Mach number (Refs. 22, 23, and 24). It is immediately apparent that at subsonic speeds a sizable compression is needed to get from shoulder pressure to base pressure. Such an adverse pressure gradient will cause the flow to separate

---

*The flow sketch in Fig. 14 shows the salient flow-field characteristics free of the extraneous out-of-plane sting effects (see inset sketch).

**Compare the effects with a submerged body at the wake neck, Refs. 20 and 21.

***As in Fig. 12, the $M = 1.5$ data points are suspect because of possible shock reflection on wind tunnel wall effects.
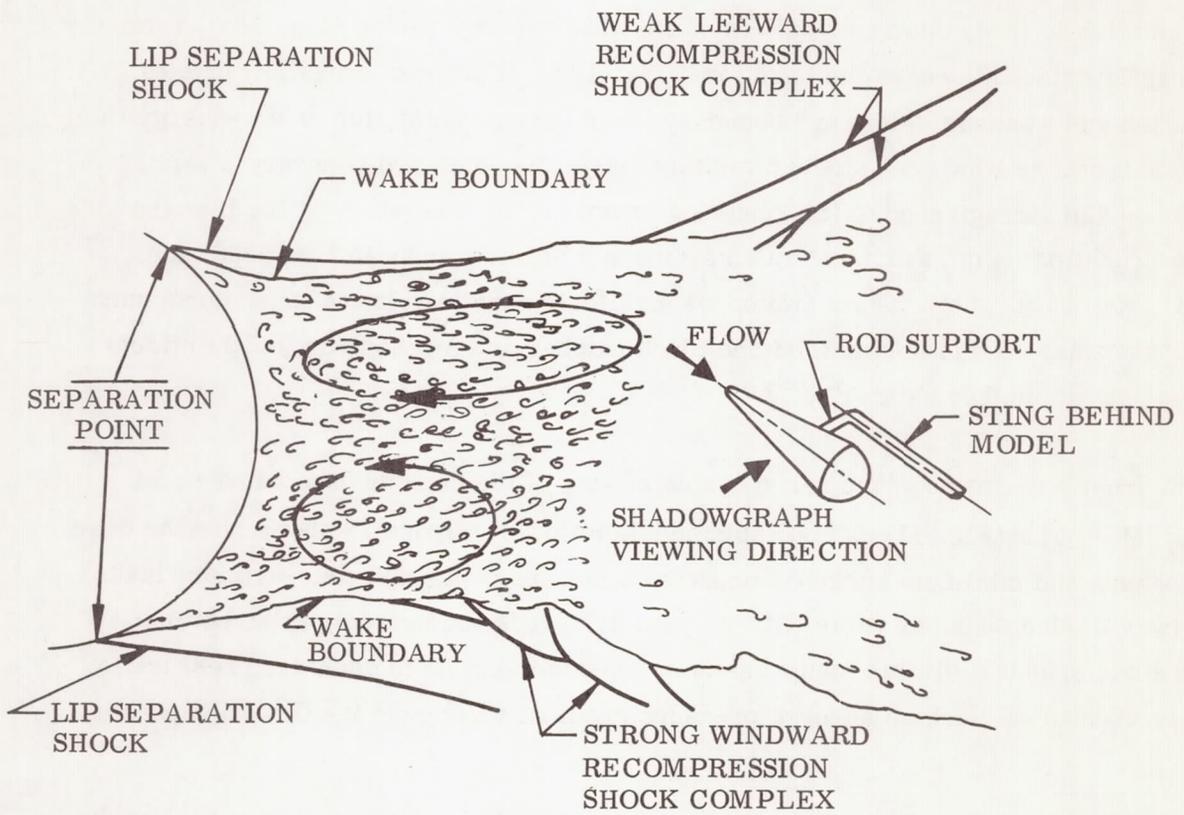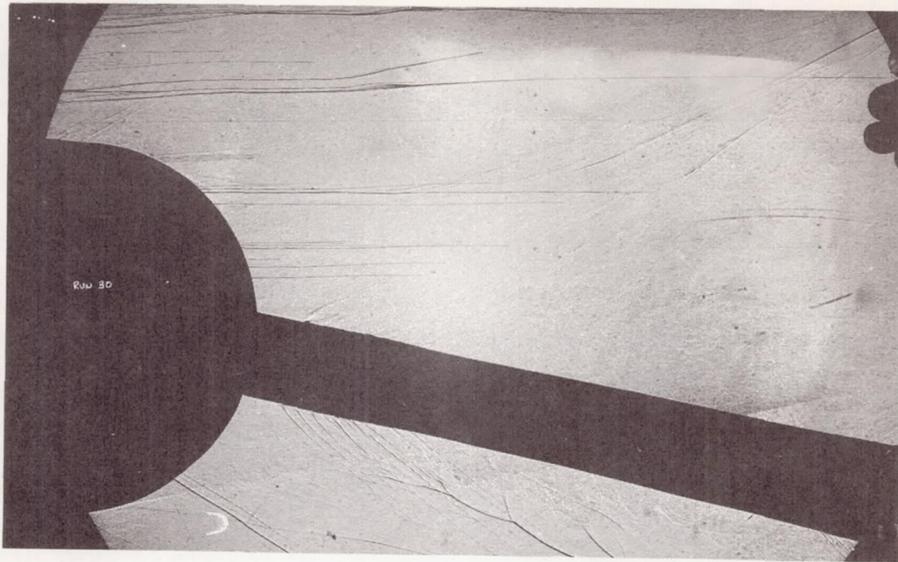
Fig. 14 Near Wake Flow Pattern of a Slender Cone With Rounded Base, M = 2.0, α = 12 deg
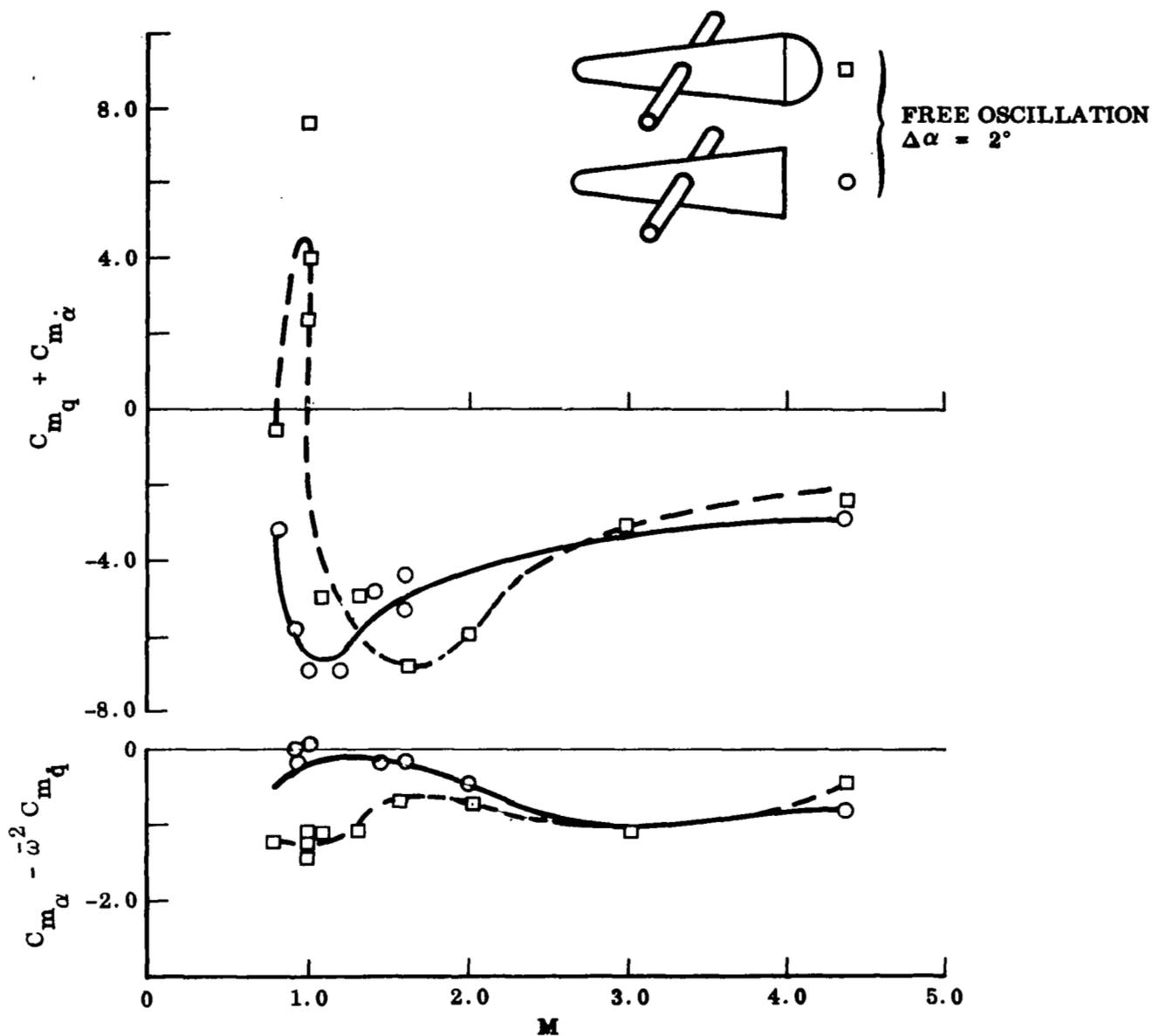
Fig. 15. Effect of Hemispherical Base on Oscillatory Derivatives of a Slender Cone for Small Amplitude Oscillations Around $\alpha = 0$
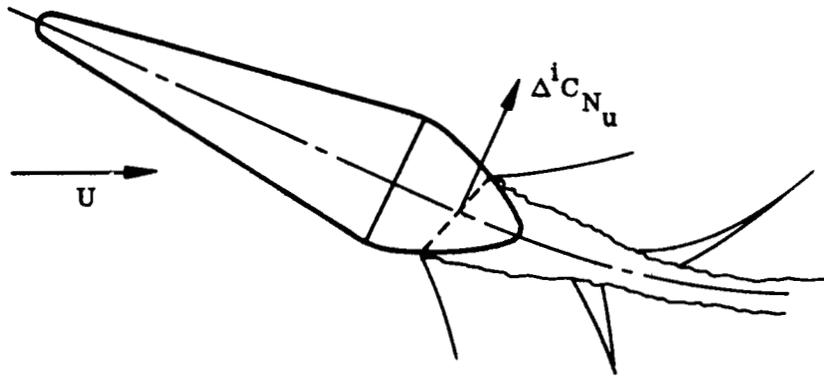
a) Upstream Communication
Effect From Wake Neck
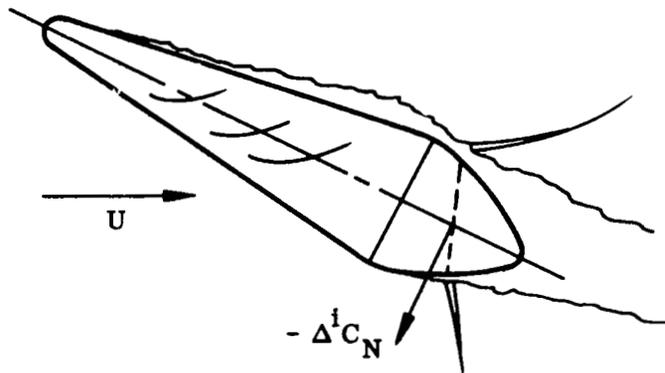
b) Downstream Boundary Layer
Collection Effect

Fig. 16 Forces Induced on a Large Bulbous Base
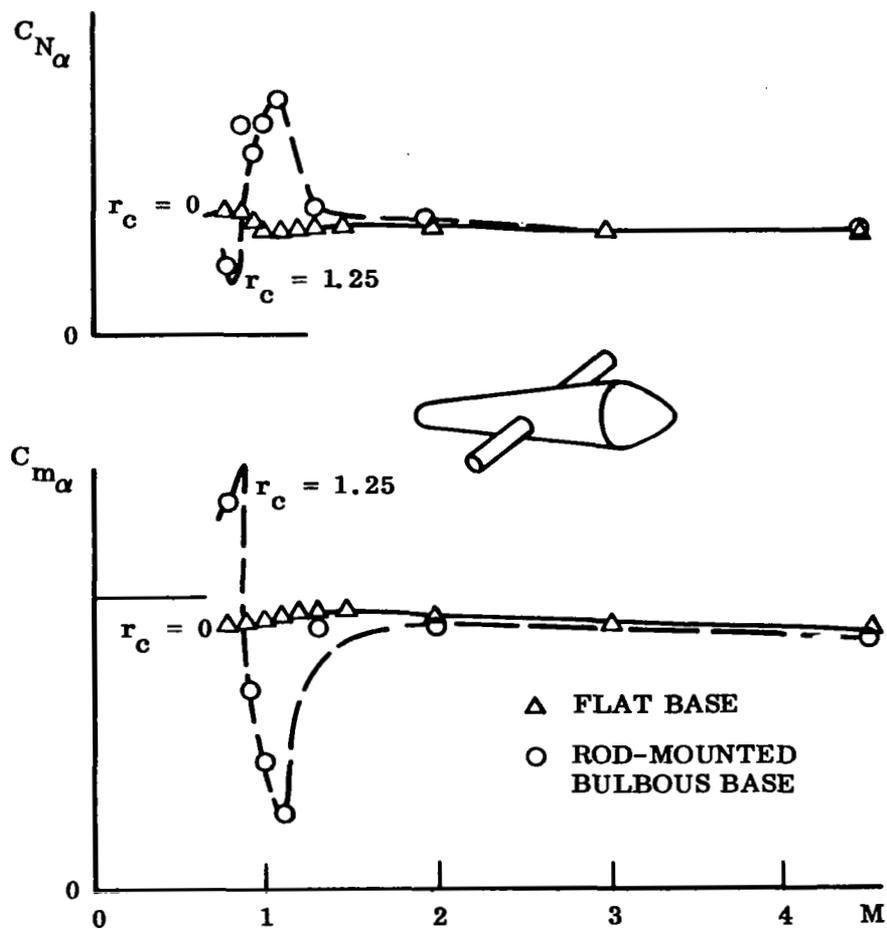
Fig. 17 Effect of a Large Bulbous Base on Static Derivatives of a Slender
Cone at $\alpha = 0$
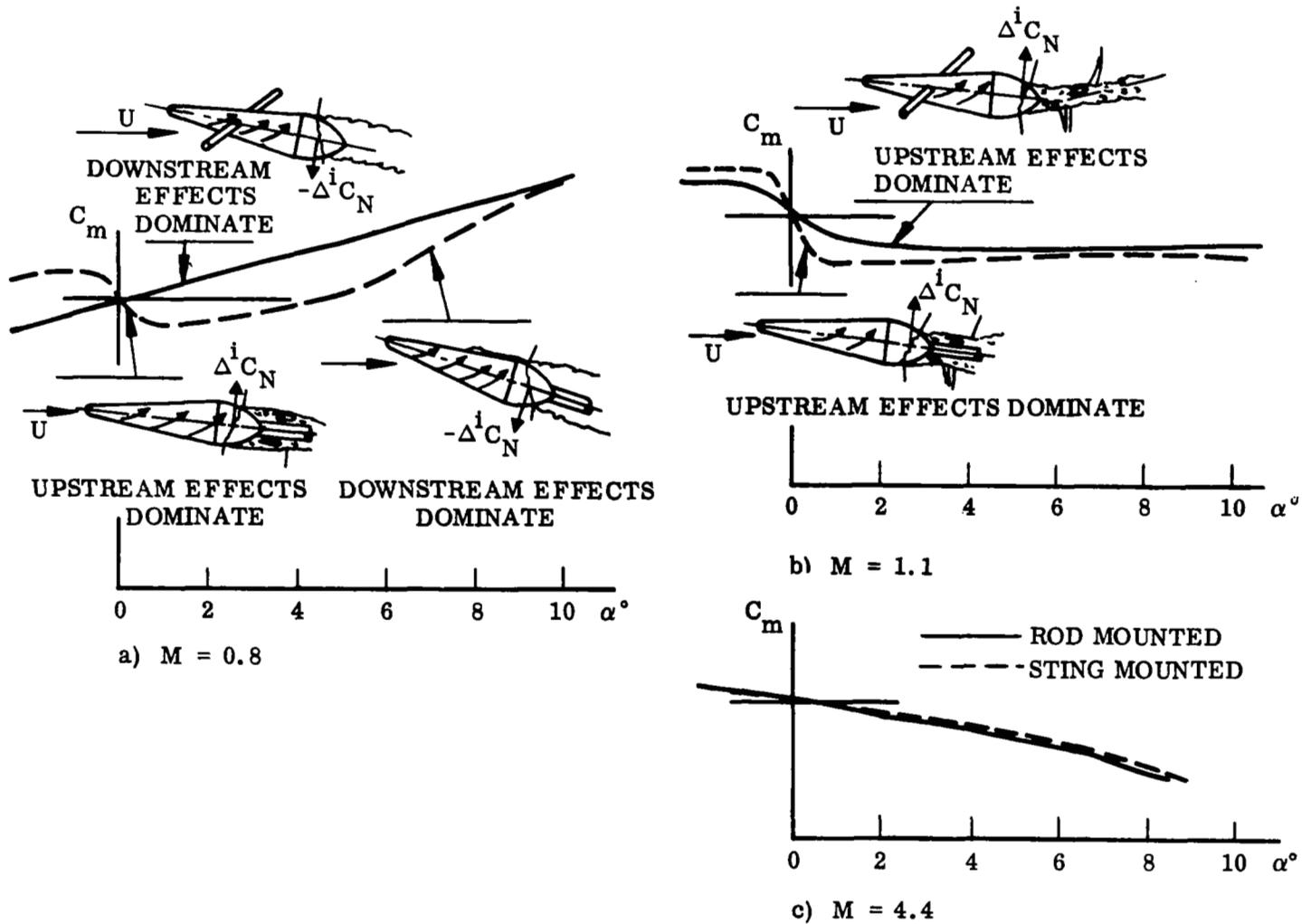
Fig. 19 Sting Interference Effects on the Static Stability Characteristics of a Slender
Cone With a Large Bulbous Base

attack. The viscous effect becomes relatively stronger with increasing angle of attack until it eventually dominates. At low supersonic speeds ($M = 1.1$), the upstream-communication effects dominate at low α for both the free-wake and the sting-mounted body. At higher α the viscous effects tend to cancel the static upstream-communication effect. As Mach number is increased, both effects tend to diminish as less of the base is affected by separated flow (Fig. 19c and Figs. 12, 15, and 17).

2.2.2 Forces Induced Forward of the Base

Even without base roundness ($r_c = 0$) the cone in Fig. 11 experiences a loss of both static and dynamic stability* when the Mach number is decreased below sonic. (See also Ref. 29.) This can best be illustrated by examining the supersonic and subsonic load distributions in Fig. 20. Subsonically, the presence of the base is felt upstream causing a reduction in both pressure and normal force relative to the supersonic case. This, of course, reduces both the static stability (C_{m_α}) and the "local" damping (C_{m_q}). Furthermore, since the flow is subsonic, the transverse pressure gradient within the wake affects the flow forward of the base producing a positive aft body load. Wehrend's static stability data (Ref. 4) shows that the loss of attached flow lift can be larger than this induced lift gain for the configuration shown in Fig. 11, resulting in a loss of static stability at subsonic speeds. The unsteady effect of the induced lift gain is undamping due to time lag effects**. When this is added to the loss of "local damping, the large decrease of dynamic stability shown in Fig. 11 results.

Rounding off the sharp shoulder between the conical forebody and the flat base will, of course, facilitate the propagation of wake effects upstream of the base. Consequently, small amounts of shoulder roundness (often too small to have been thought

---

*The undamping trends shown in Fig. 11 are attenuated by sting interference, as will be shown later.
**Supersonically, the upstream communication can take place only through the boundary layer and is, therefore, usually negligible (see Fig. 20).
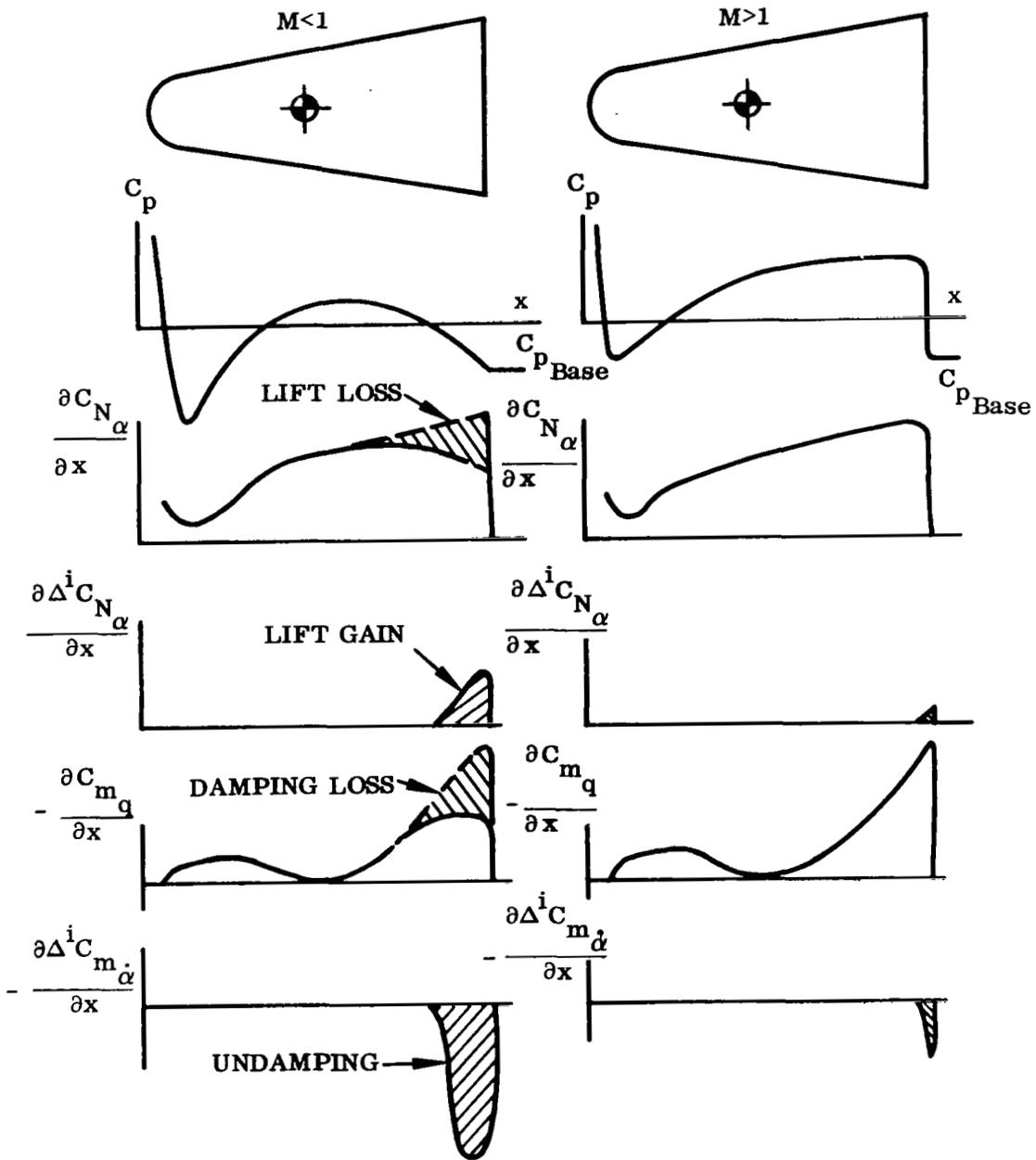
Fig. 20 Comparison Between Subsonic and Supersonic Aerodynamic
Characteristics

of as being of any aerodynamic significance) can have large undamping effects on the subsonic and transonic aerodynamic characteristics. This is illustrated by the wind tunnel test results shown in Fig. 21.

2.2.3 Forces Induced at High Speeds and Low Density

The subsonic forebody load modification which is insignificant at supersonic Mach numbers again becomes important at hypersonic speeds. This is really an enhancement of the normally negligible supersonic boundary layer communication effect (Fig. 20), facilitated by a thick laminar boundary layer. Thickening the boundary layer (e.g., by decreasing unit Reynolds number) promotes forebody load modification[*] (Ref. 30) as does shoulder roundness (Fig. 22).

Ward (Ref. 31) has shown another mechanism for forebody load modification, i.e., the effect of boundary layer transition. On a sharp cone, the leeward side boundary layer collection induces early transition generating a negative viscous interaction force (Fig. 23a). Contributing to early transition is the adverse pressure gradient caused by the lip shock. The local overexpansion at the base is recompressed back to base pressure via the lip shock (Ref. 32). Increasing the thickness of the viscous layer[**] causes the wake recompression to gradually merge with the lip shock, thereby greatly increasing the adverse pressure gradient. This lip-shock-induced adverse-pressure gradient is increased by the leeward-side boundary layer collection, further

---

[*]The loads induced on the base itself may not be insignificant for the largest shoulder radius, $r_c = 0.21$.
[**]E. g., by decreasing Reynolds number (Ref. 32).
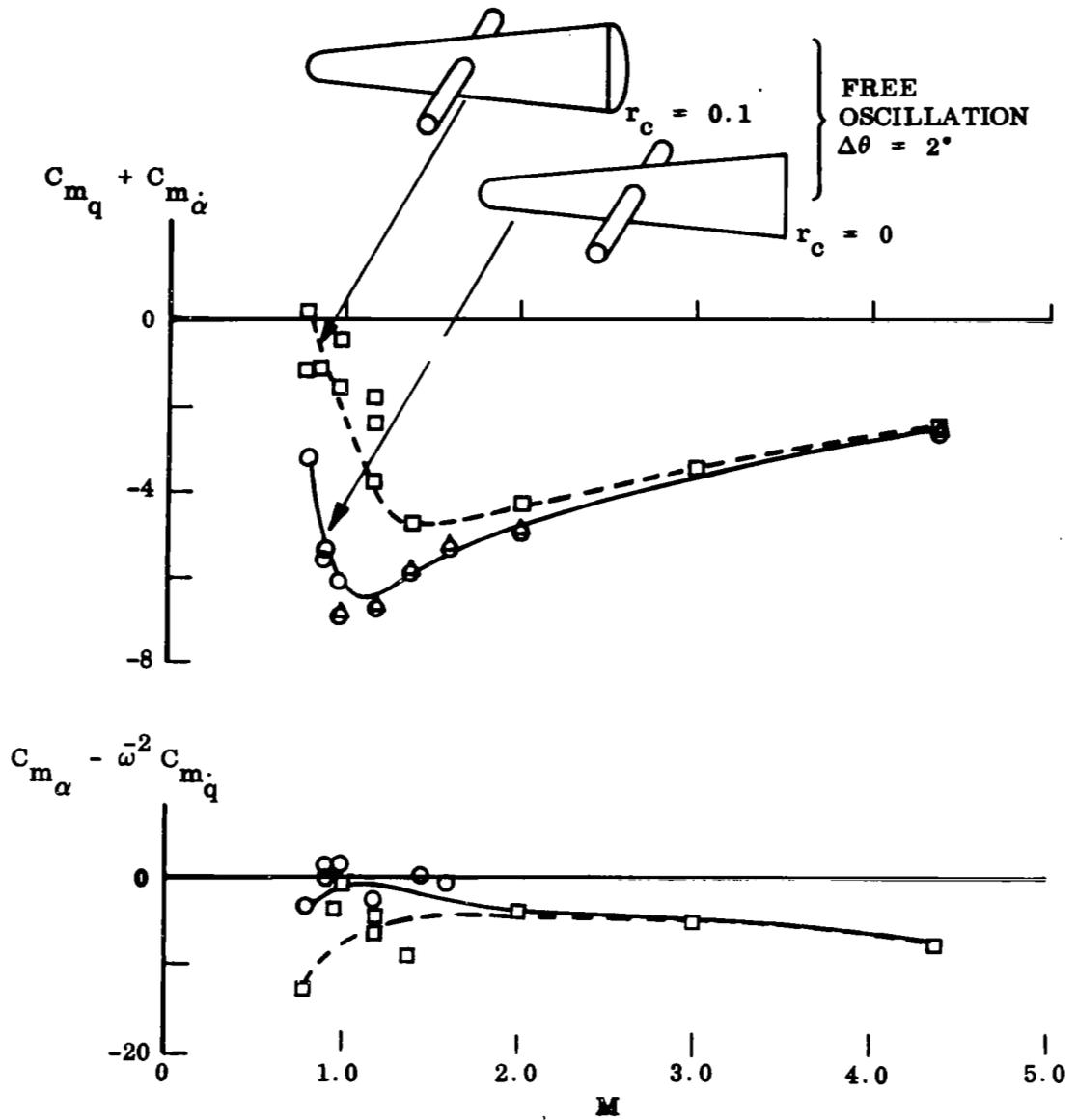
Fig. 21 Effect of Base Shoulder Radius on an Oscillatory Derivatives of a Slender Cone for Small Amplitude Oscillations at $\alpha = 0$
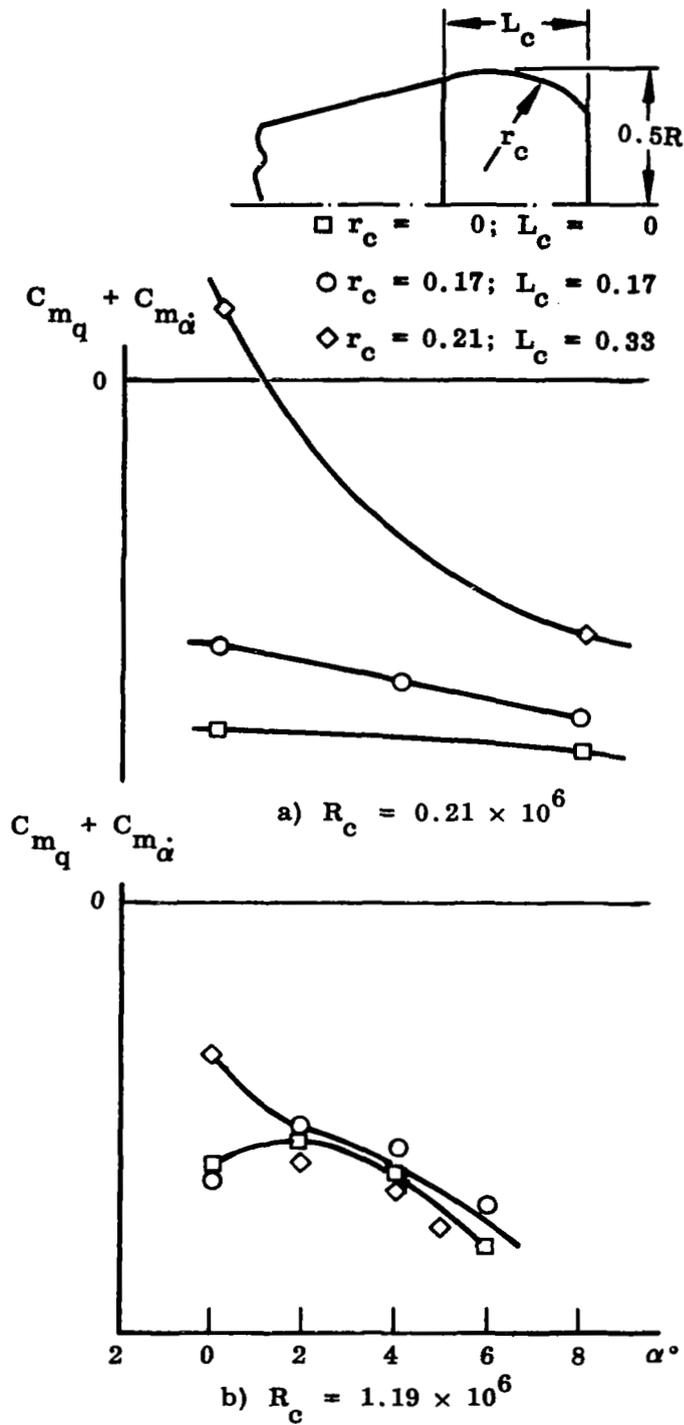
Fig. 22 Effect of Base Shoulder Curvature on the Pitch Damping of a Slender
Body for Small Amplitude Oscillations at M = 10

a) Effect of α, $R_L = 8 \times 10^6$

b) Effect of Reynolds Number, $\alpha = 0$, $\Delta\alpha = 1.8°$
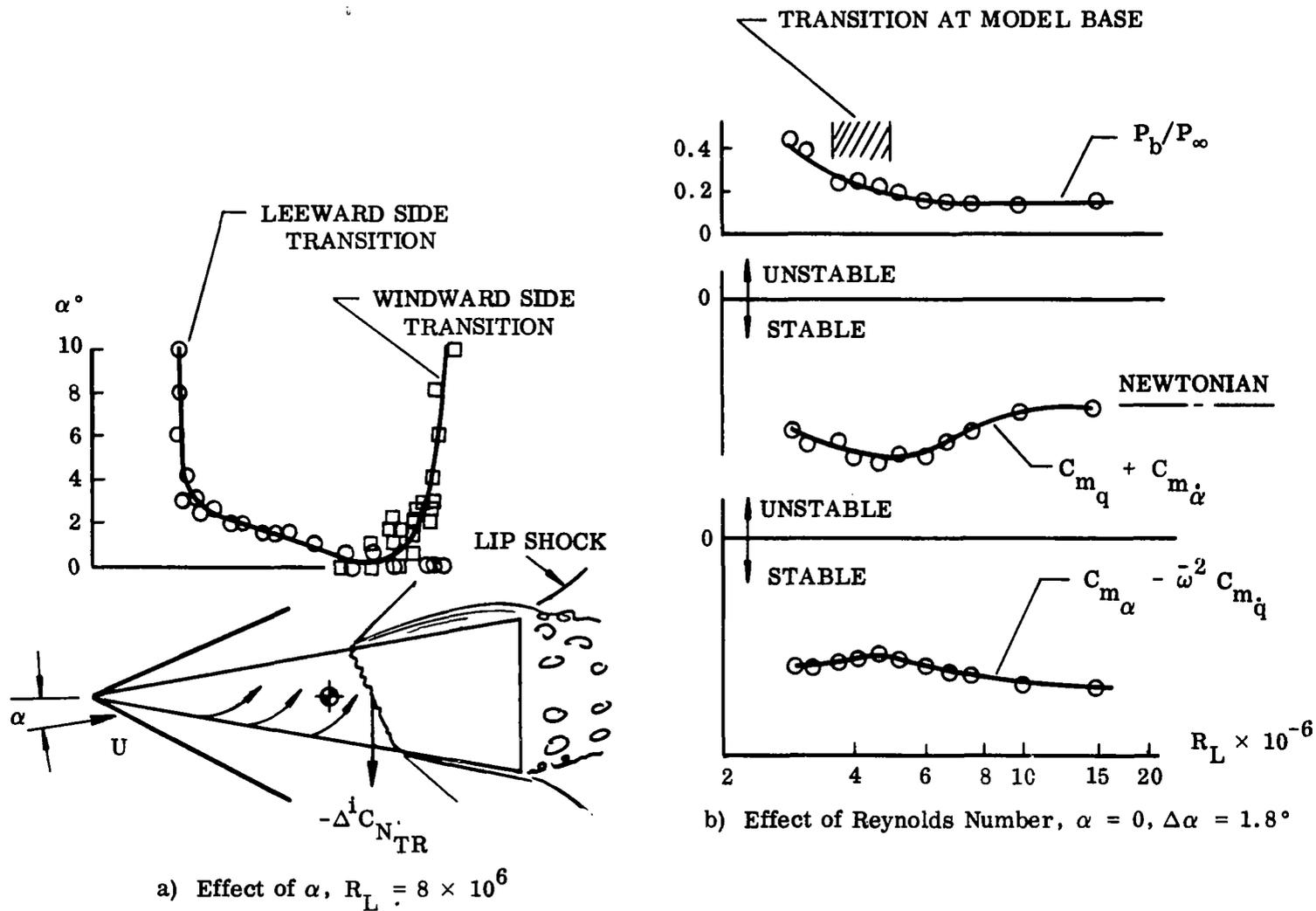
Fig. 23 Effect of Angle-of-Attack and Reynolds Number at $M = 6$ on Boundary Layer
Transition and Oscillatory Derivatives for a Sharp, Slender Cone With a
Flat Base

promoting early leeward-side transition. The effect would be statically destabilizing but dynamically stabilizing due to viscous time-lag effects (Ref. 33),* and the effect would be maximum when transition takes place near the base, all in agreement with the measured effect (Fig. 23b).

On the more slender blunted cone discussed earlier (Figs. 12—17) the effect of boundary layer transition is more pronounced (Ref. 35 and Fig. 24)**. The transition induced increase in boundary layer slope is more effective on the more slender cone (cone half angle 40 percent less than that of Ward's model). Also, the favorable pressure gradient induced by the large nose bluntness could cause appreciable changes in the α-sensitivity of the boundary layer transition. At more moderate nose bluntnesses, for which sharp cone pressures are reached on the aft body, a reversal of this boundary layer transition effect is possible. Cleary (Ref. 36) has shown that the impingement of the nose-induced entropy layer on the windward side causes earlier windward than leeward side transition. That the entropy swallowing has a dominating influence on boundary layer transition was demonstrated recently by Softley, et al (Ref. 37). This effect of nose blunting has been observed experimentally at hypersonic Mach numbers on rod-mounted models for both flat and curved bases. It was even found that nose bluntness could change the effect of a curved base from undamping on a sharp cone to damping on a blunted cone. This results from the coupling between boundary-layer transition and the base-flow separation. On the sharp cone forebody, boundary layer collection promotes early leeward-side transition, thus making the boundary layer approaching the base relatively stronger on the

---

*In the unsteady case, accelerated flow effects on transition may be significant (Refs. 27 and 34).

**At M = 6 the effect might have been even greater, but the Reynolds number capability of the tunnel could not produce transitition on the model at this Mach number. $Re_L > 50 \times 10^6$ would have been needed.
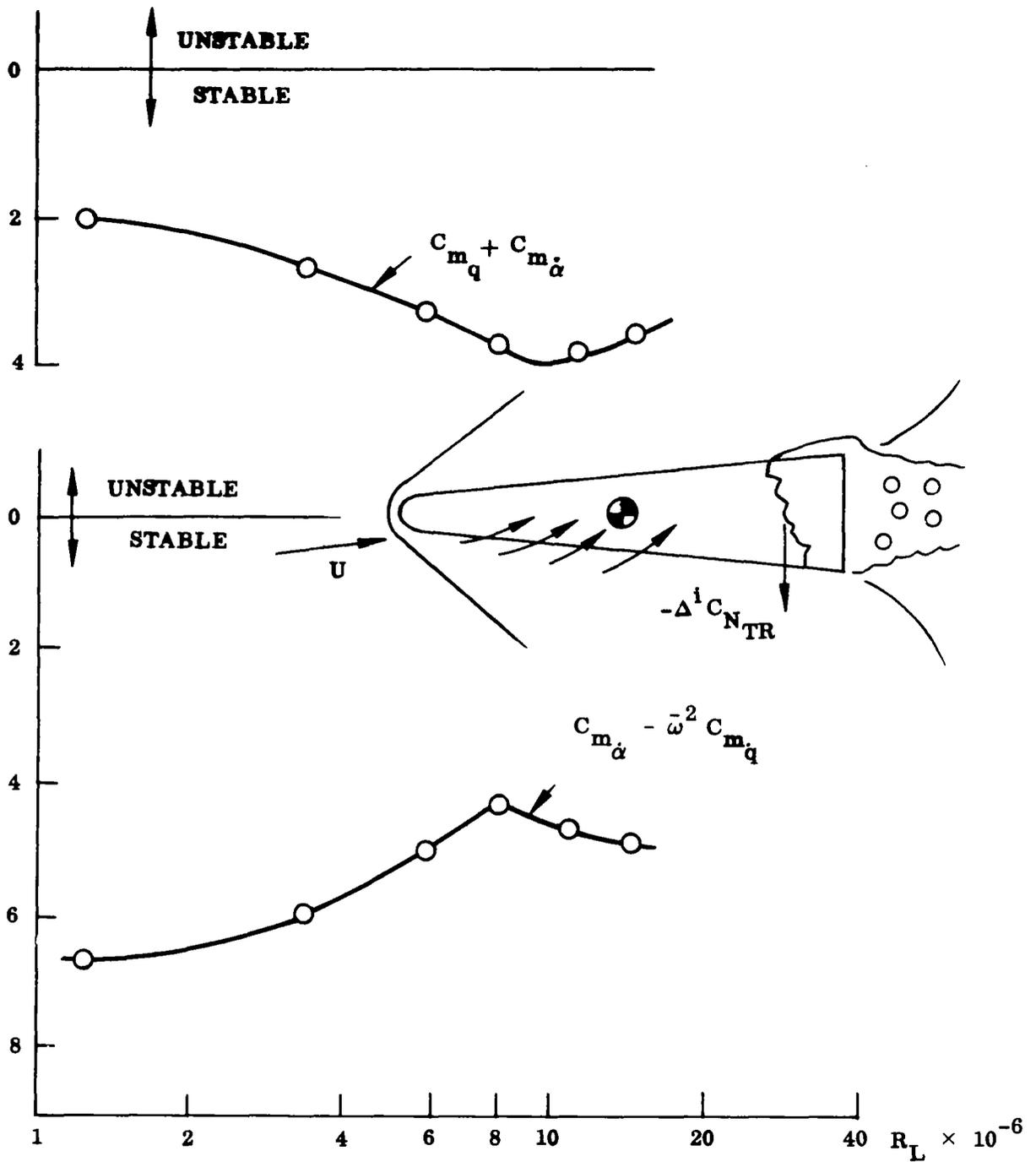
Fig. 24 Effect of Reynolds Number at M = 4 on Oscillatory Derivatives
of a Blunted Slender Cone With Flat Base

leeward side. As a result, the leeward-side separation is delayed* and a statically-stable/dynamically-unstable base load is generated (Fig. 25a). Nose bluntness reverses the boundary layer transition and, consequently, causes a statically-unstable/dynamically-stable base load (Fig. 25b).

The resurgence of the base effect at hypersonic speeds is very disconcerting. This is the speed range where ablation effects become important (Refs. 33 and 39), thus further complicating an already complicated flow field.

2.3 SUPPORT INTERFERENCE

In the previous discussion, the static sting interference effects have proven useful in explaining the effects of the upstream communication from the wake-recompression region. However, support interference is undesirable because it precludes simulation of the true flight vehicle characteristics. It has been amply demonstrated that wake submerged support systems can have a profound effect on the static stability of bulbous-based bodies. Due to time lag effects one would expect an even greater impact on the aerodynamic damping. For some cases transverse rod support systems have been observed to have a significant effect on the wake geometry (Refs. 40 and 41), whicn in turn will affect the damping. The interference effects are highly sensitive to the support configuration, and each type of support system has a unique effect on measured stability.

2.3.1 The Cylindrical Sting

The slender cylindrical sting presents the simplest example of support interference. All dynamic data discussed so far, unless otherwise stated, are believed to be influenced by this type of interference. Statically, the cylindrical sting enhances the free-wake-induced load (Fig. 26a and b), while dynamically the sting interference usually

---

*Similar effects of transition have been observed on cone-cylinder-flare bodies (Ref. 38).
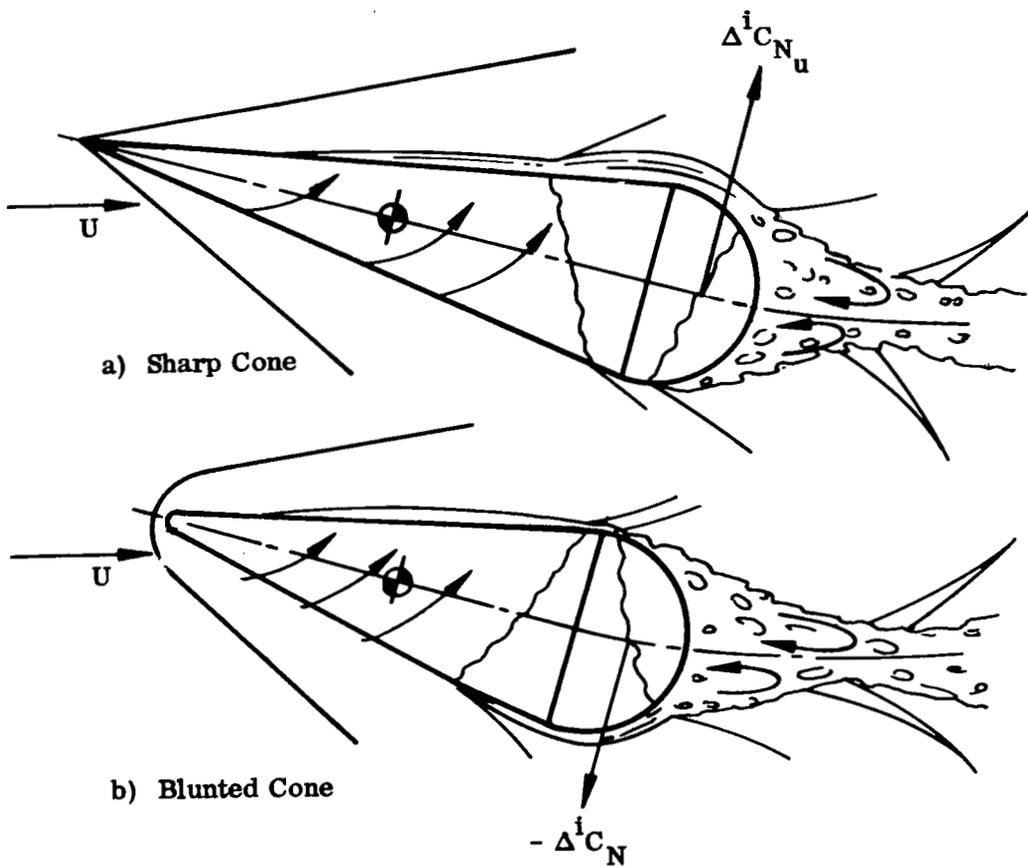
Fig. 25 Effect of Nose Bluntness on Hypersonic Boundary Layer Transition
and Base Flow Over a Slender Cone With a Rounded Base

a) Static Sting Support

b) Free Wake

c) Dynamic Sting Support
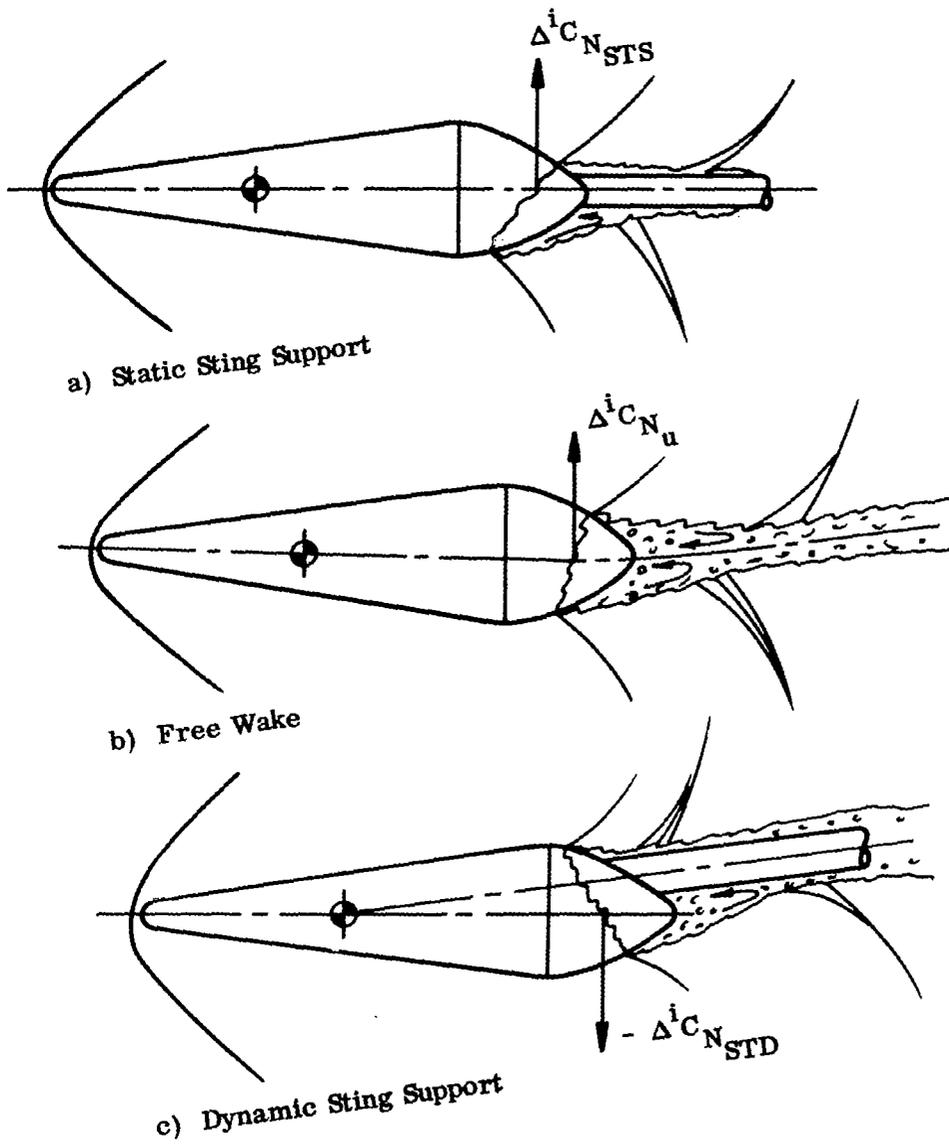
Fig. 26 Effect of Sting on Forces Induced on a Bulbous Bases

opposes the free-wake effect (Figs. 26b and c)*. This is true since it is usual practice to pitch the model-sting combinations together when obtaining static data, whereas in dynamic testing, the model usually pitches about a rigid sting.

In the static case, the sting reinforces the upstream-communication effect, as it can support a greater transverse pressure gradient than the free wake. At high subsonic speeds, $M = 0.8$, the sting may reverse the true base effect by causing the upstream communication effect from the wake to overpower the downstream-boundary layer collection effect (Fig. 19a)**. At higher Mach numbers the sting interference disappears with the same rate as the true base effect (Fig. 19c) but will, of course, recur for hypersonic low density flow where the wake configuration becomes extremely sensitive to downstream influences (as indicated by the shadowgraphs of bodies in hypersonic laminar wakes, [Ref. 42]).

Thus, the sting causes a magnification of the static effects of the upstream communication from the wake; however, in dynamic tests the opposite is true. The model base oscillates in both pitch and translation relative to the fixed sting (Fig. 26c). Consequently, the interference will be even greater dynamically, and will be further magnified by time lag effects. Thus, the rather small differences between rod- and sting-mounted aerodynamic spring measurements (Fig. 27)*** result in large differences in the damping. The cylindrical sting, therefore, is seen to provide an erroneous and unconservative measure of the damping of bulbous-based bodies. Whenever the possibility of upstream communication exists, dynamic sting interference may prevent valid simulation of full-scale vehicle dynamics. As an example, the

---

*The sting interference effects $\Delta^i C_{N_{STS}}$ and $\Delta^i C_{N_{STD}}$ are greatly exaggerated in Fig. 26 and, for simplicity, illustrated as additional forces to the free-wake force $\Delta^i C_{N_u}$, i.e., the true force on the base with sting would be $\Delta^i C_{N_u} + \Delta^i C_{N_{ST}}$ and the true flow pattern would differ correspondingly.

**The fact that this condition can have a distorting effect and greatly magnify any aerodynamic hysteresis is indicated by other subsonic test results.

***The results from the rod-mounted model are believed to be more nearly representative of the free wake results although they, too, may be somewhat affected by support interference.
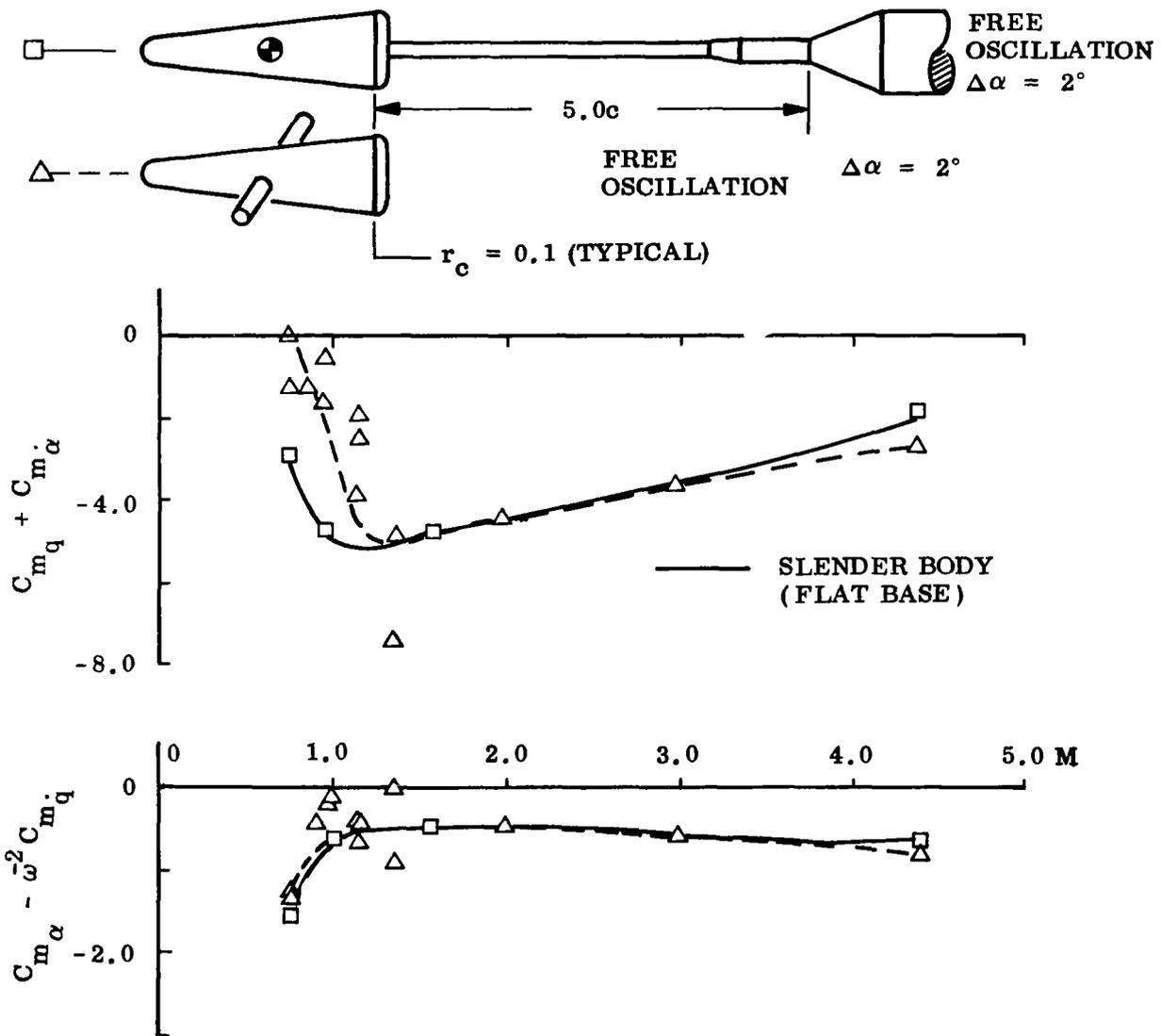
Fig. 27 Dynamic Support Interference Effects for a Hemispherical Base

subsonic dynamic characteristics of a blunt cylinder-flare body are radically distorted by sting interference (Fig. 28 and Ref. 43). Sting interference first materializes when the outer portion of the separated flow starts to re-attach on the sting without first impinging on the flare. This happens at α = 2 deg in Fig. 28. Addition of a rounded base (also where nose induced separation is concerned) has the usual undamping effect*.

2.3.2 The Flared Sting

While the cylindrical sting provides rather straightforward interference effect, the effects of the flared sting are more subtle. Data recently obtained at the NASA Langley Research Center** (Fig. 29) indicate the usual opposition between static and dynamic results; however, the sting interference moment ($C_{m_{\delta_S}}$) is statically stabilizing and appears to be responsible for much of the observed undamping of the bulbous-based bodies. The interference moment was obtained statically by deflecting the sting relative to the model by an angle δ_S (Fig. 30) and pitching the model sting combination. The results were then carpet-plotted (Figs. 31 and 32 and Refs 44 and 45) to yield the interference derivatives $C_{N_{\delta_S}}$ and $C_{m_{\delta_S}}$.*** The interference derivatives $C_{N_{\delta_S}} > 0$ and $C_{m_{\delta_S}} < 0$, indicate a flared sting interference that is opposite to the interference caused by a cylindrical sting.

The nonlinear increase of the static interference moment ($C_{m_{\delta_S}}$) (as the rotation center is moved forward) indicates that more than a simple moment arm increase is involved (Fig. 33). As the rotation center is moved forward, the model base approaches the asymmetric flared portion of the sting (since the distance to the balance pivot [Fig. 30]

---

*In view of these results, the good correlation between quasi-steady estimates and test data in Ref. 6 may not be due to negligible upstream communication effects from the flare, but could be the fortuitous result of dynamic sting interference cancelling a non-negligible upstream communication effect from the flare.

**This work was accomplished by Mr. J. Adcock under the direction of Mr. H. Wiley (both of the Full-Scale Research Division) in connection with the subject contract.

***Statically (when the model and sting pitch together) the flared sting induced moment ($C_{m_{\delta_S}}$) is opposed by the stabilizing effect of the bulbous base. This results, for some configurations, in a complete cancellation of the sting interference affect on C_{m_α}. Thus, C_{m_α} in itself does not necessarily reveal the existence of sting interference effects. Consequently one must rely on the direct measurement of the sting interference ($C_{N_{\delta_S}}$ and $C_{m_{\delta_S}}$).
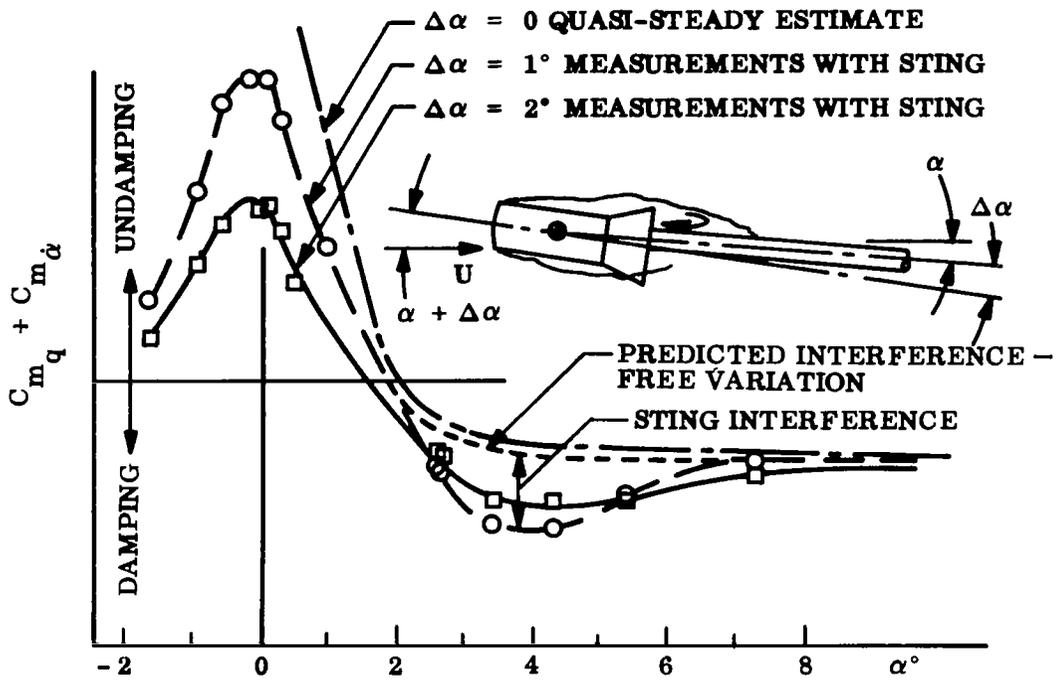
Fig. 28 Effect of Sting on a Pitch Damping of a Flared Cylinder
at M = 0.65
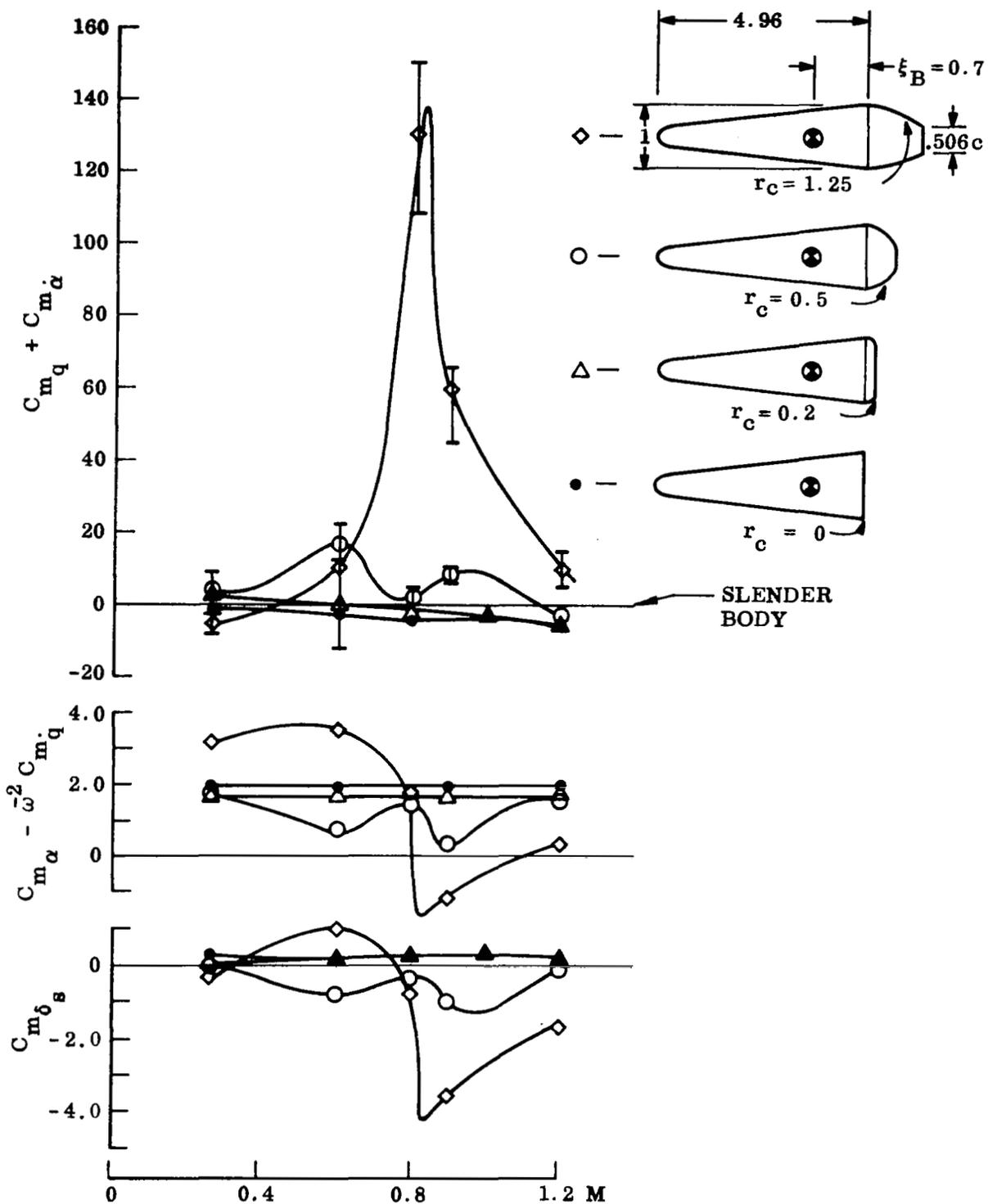
Fig. 29 Correlation of Sting Support Induced Moment with Static and Dynamic Stability
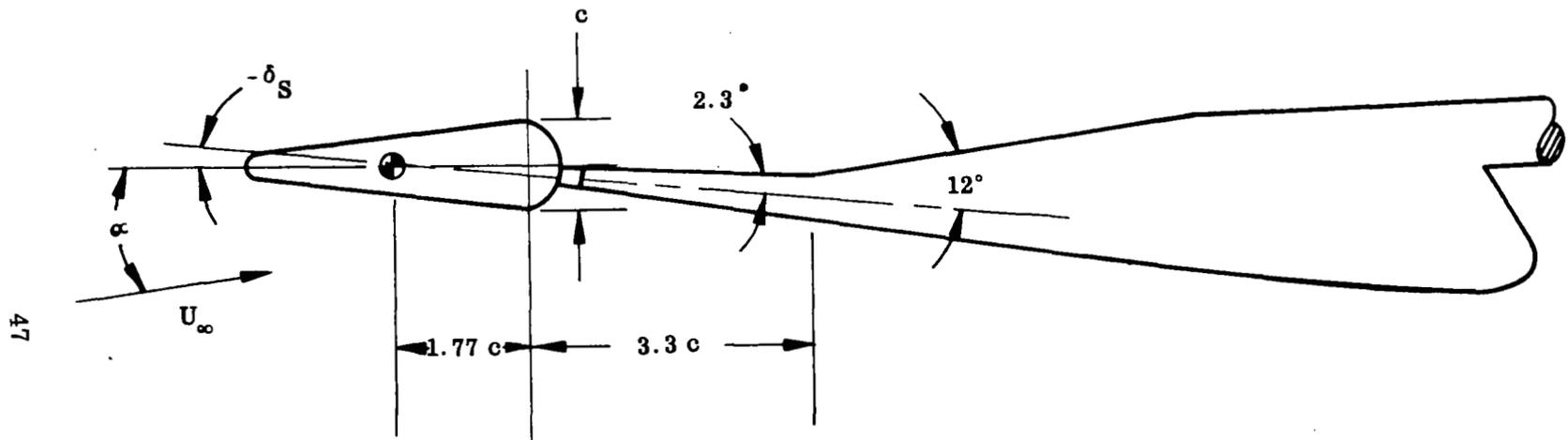
Fig. 30 Langley Model — Sting Arrangement
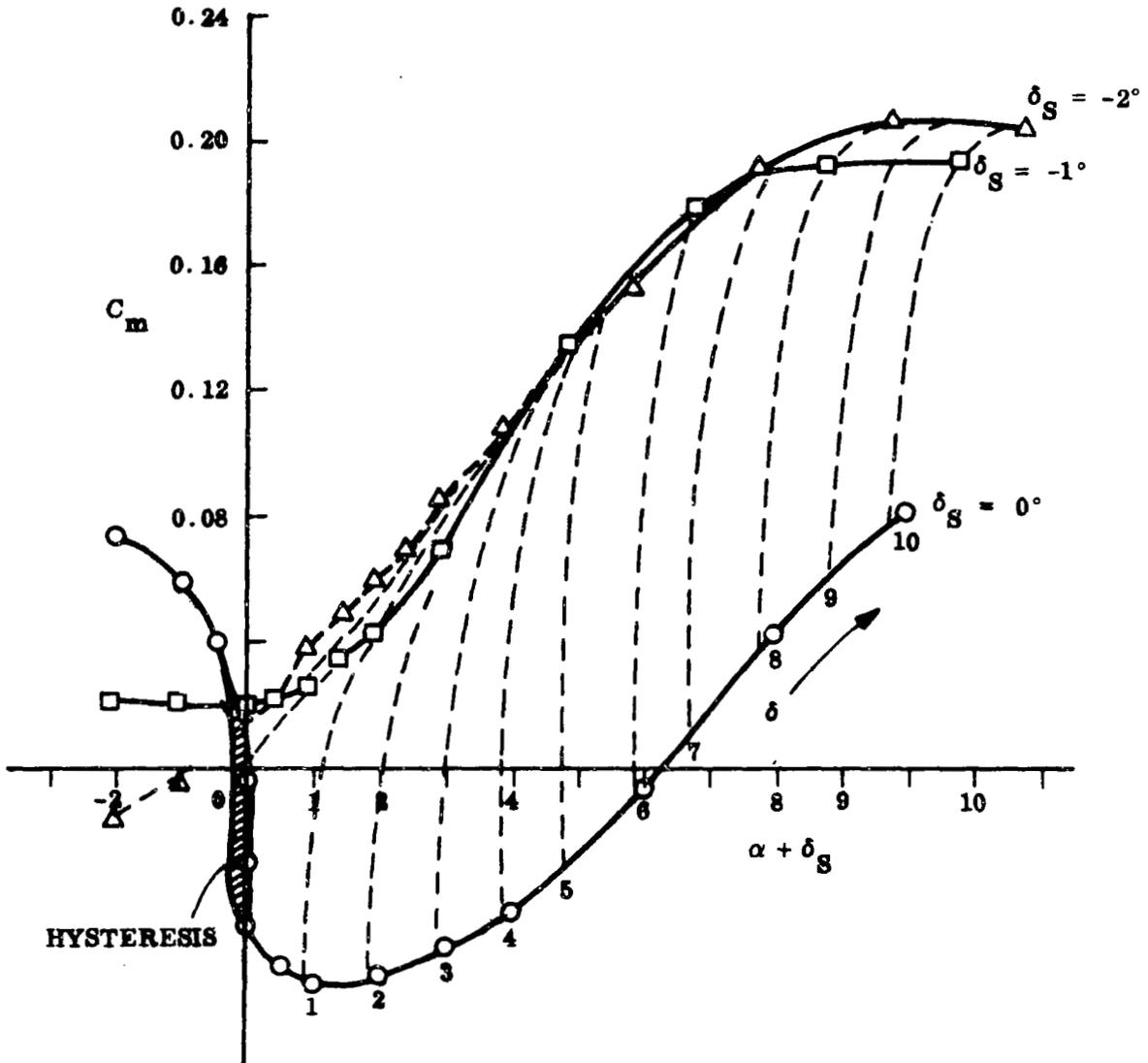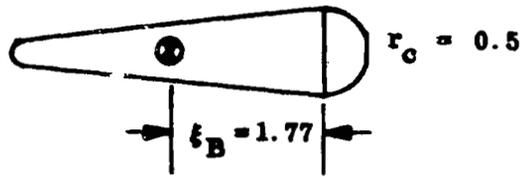
Fig. 32 Sample Pitching Moment Carpet Plot for M = 0.26
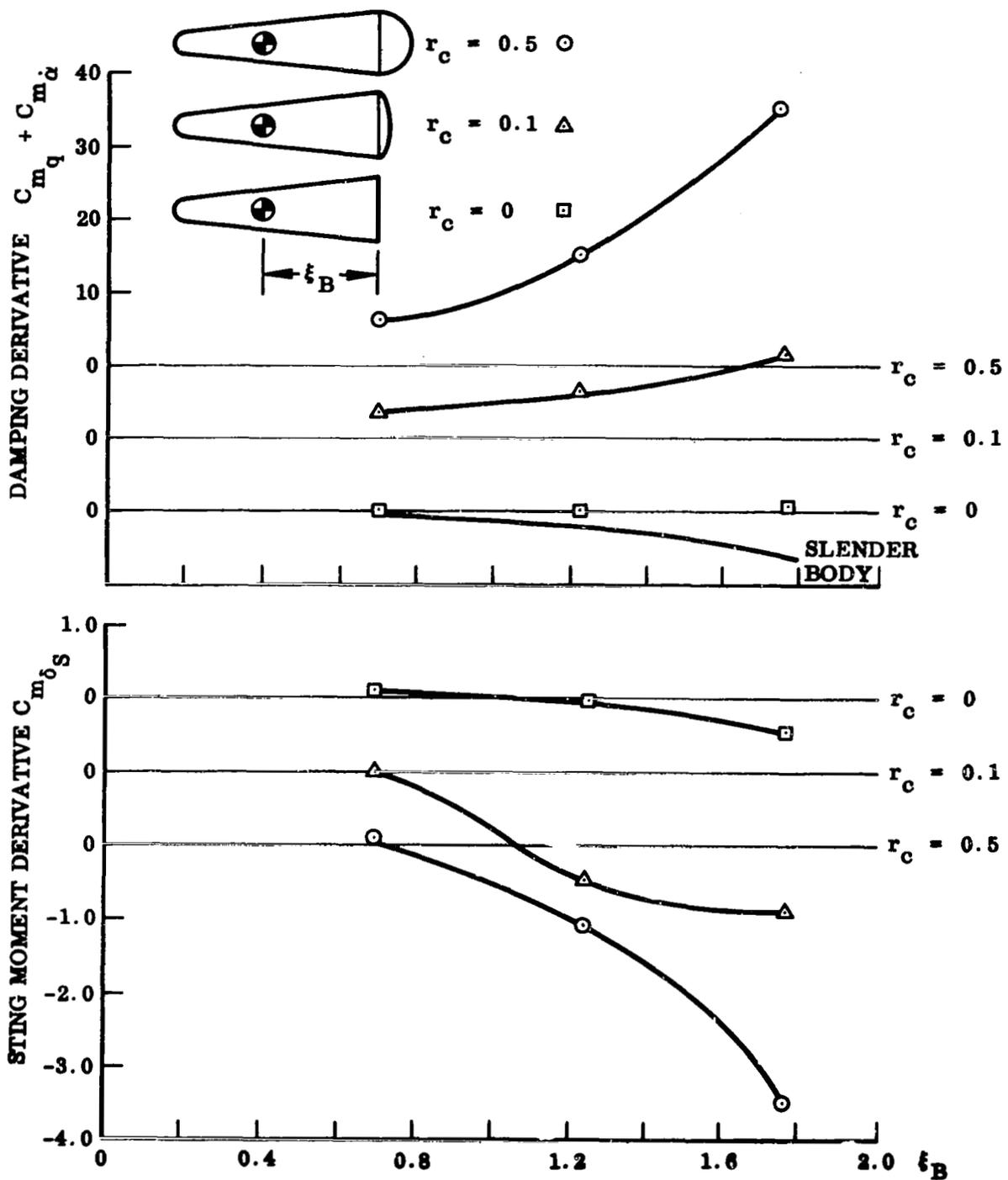
Fig. 33a Effect of Rotation Center on Support Interference M = 0.26
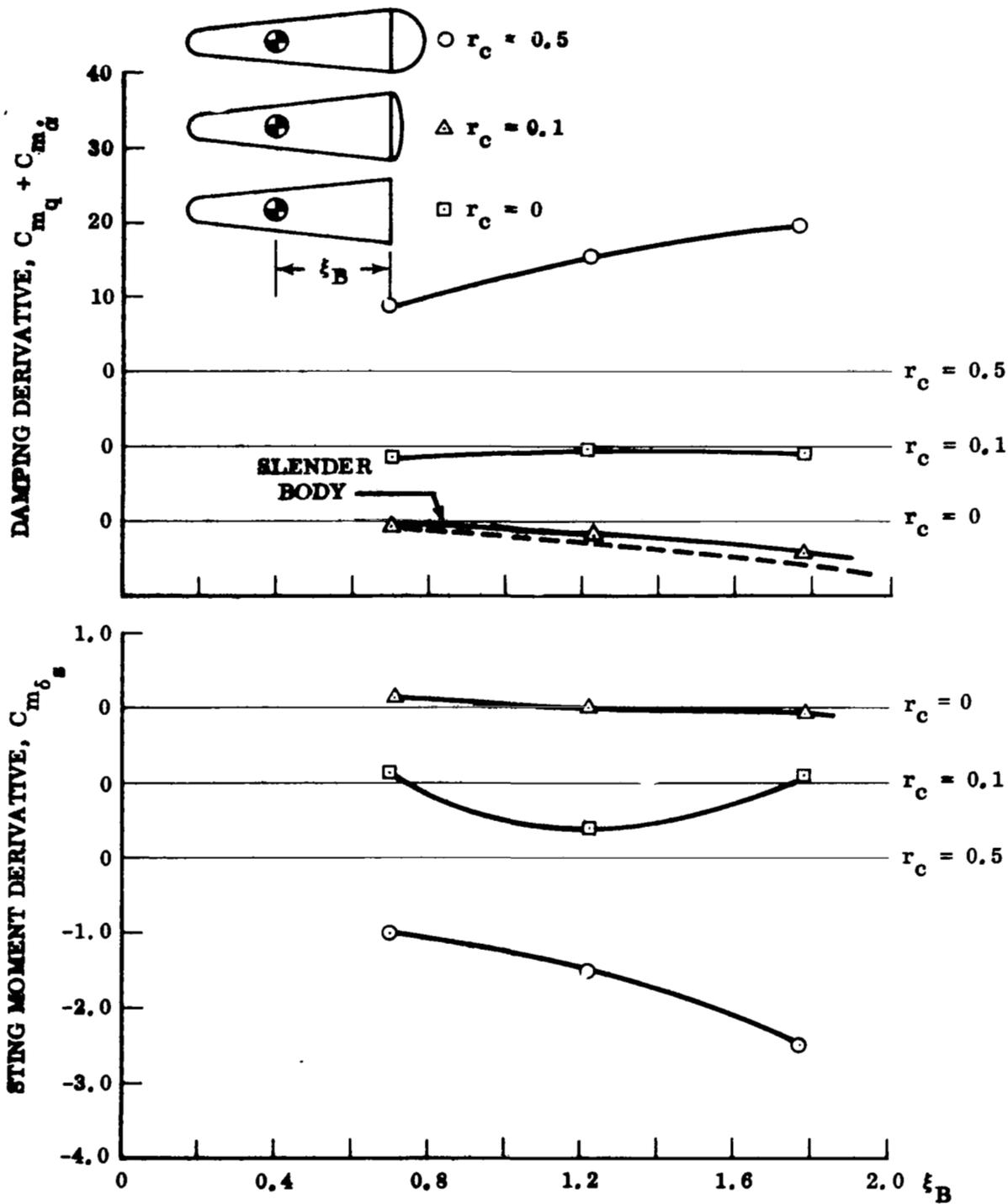
Fig. 33b Effect of Rotation Center on Support Interference M = 0.9
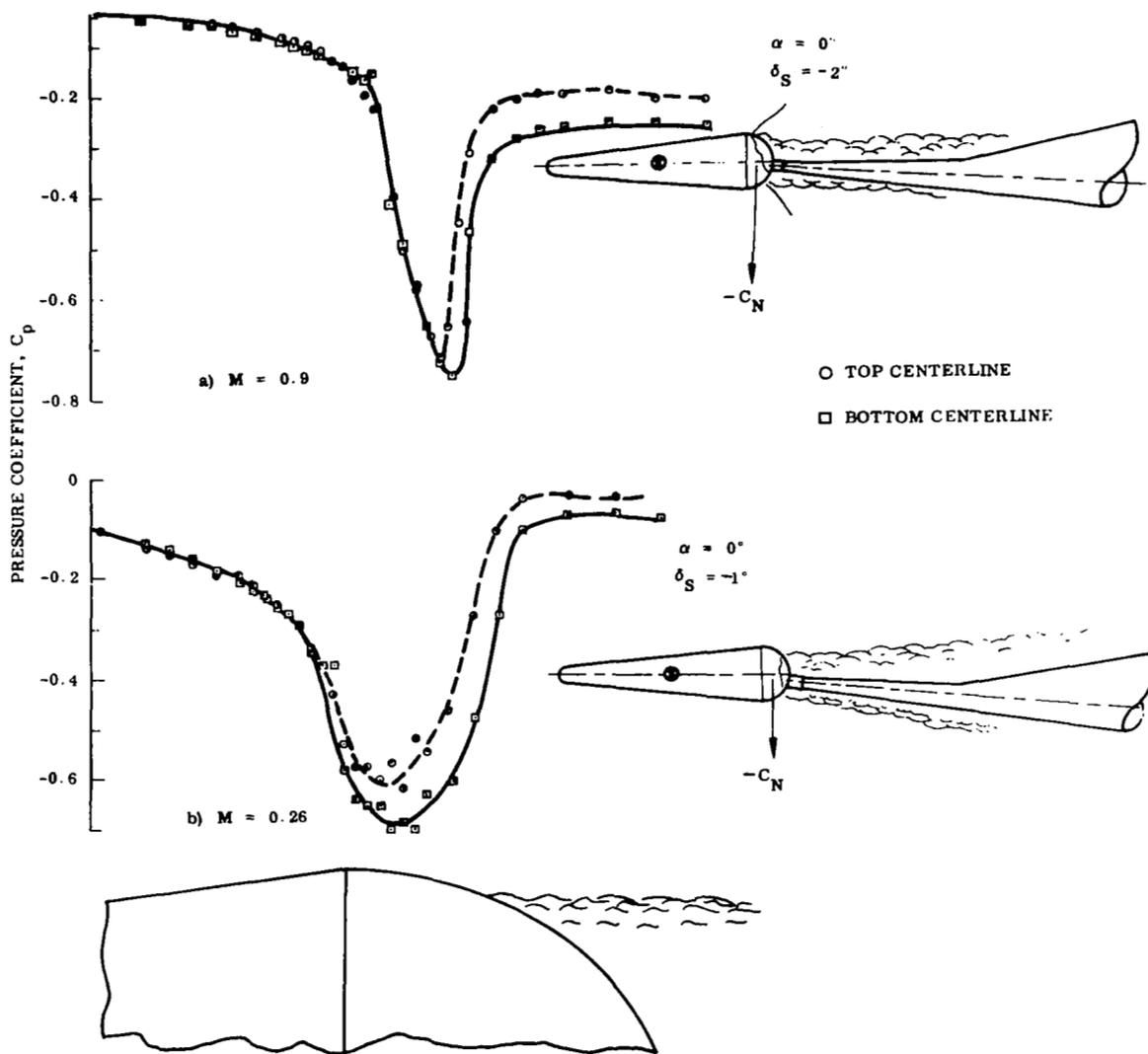
Fig. 34 Pressure Distribution on Hemispherical Base, $\alpha = 0$, $\delta_S < 0$
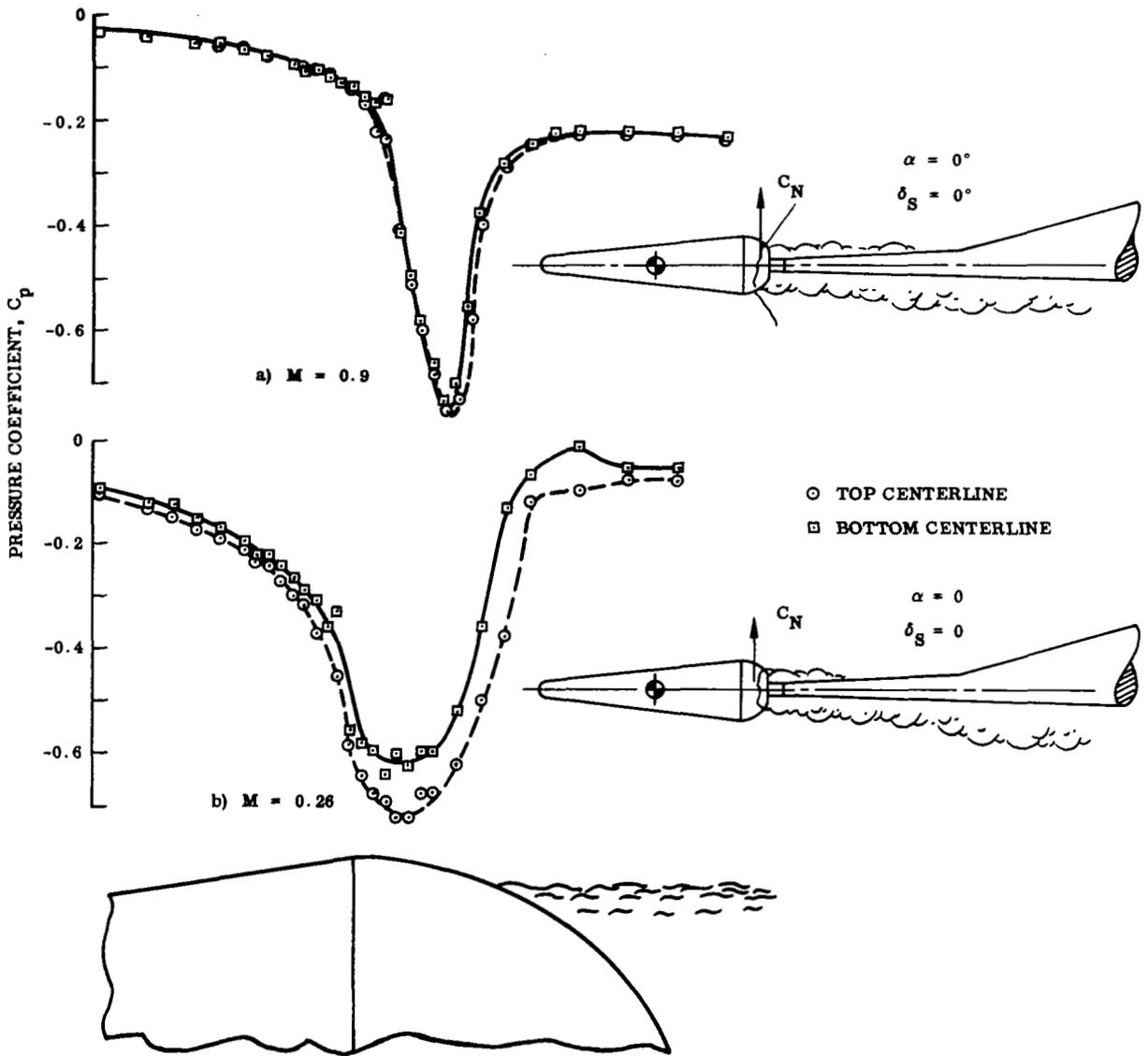
Fig. 35 Pressure Distribution on Hemispherical Base $\alpha = 0$, $\delta_S = 0$

54
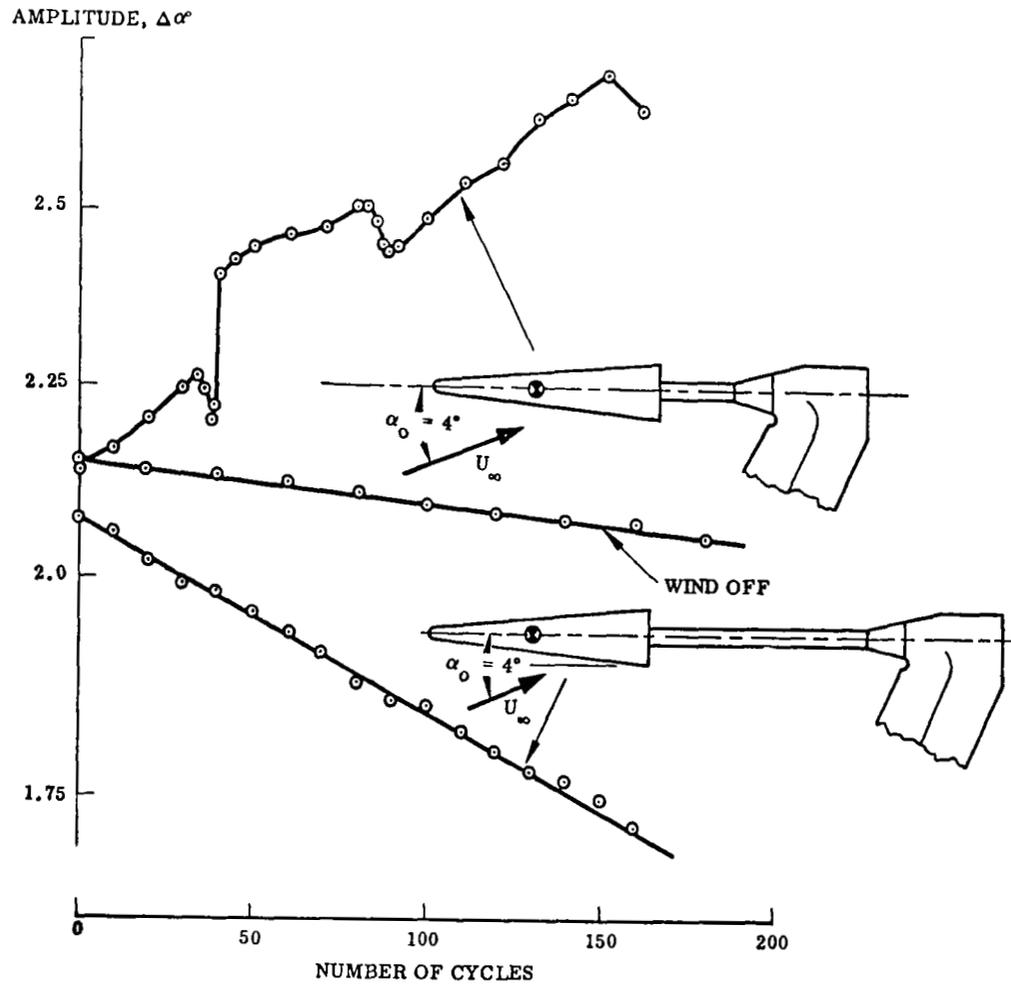
Fig. 36 Dynamic Hypersonic Support Interference, M = 14 (Ref. 49)

a) SHORT STING
WITHOUT SPLITTER
PLATE

b) LONG STING
WITHOUT SPLITTER
PLATE

c) LONG STING
WITH SPLITTER
PLATE
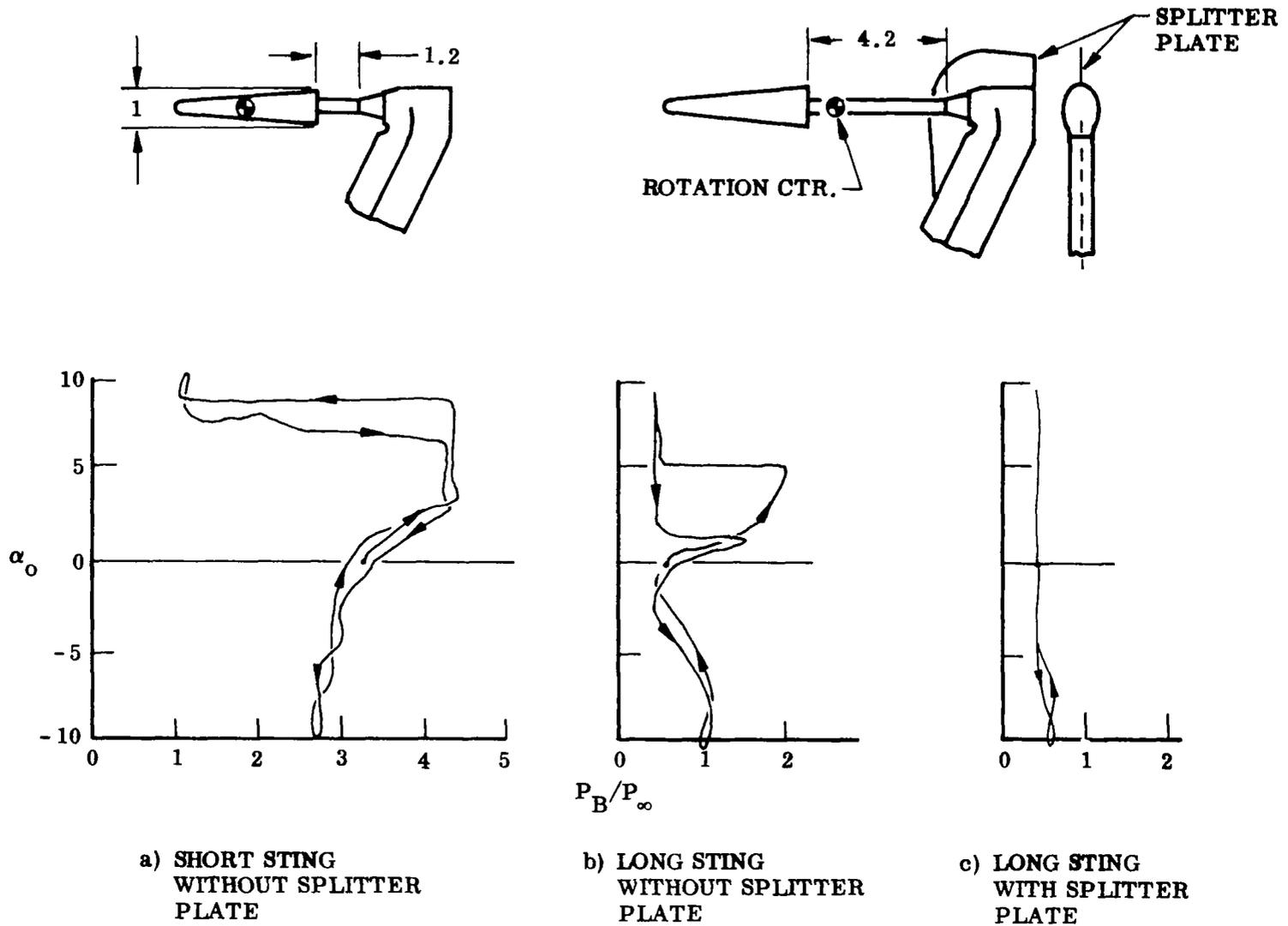
Fig. 37 Static Hypersonic Support Interference, M = 14
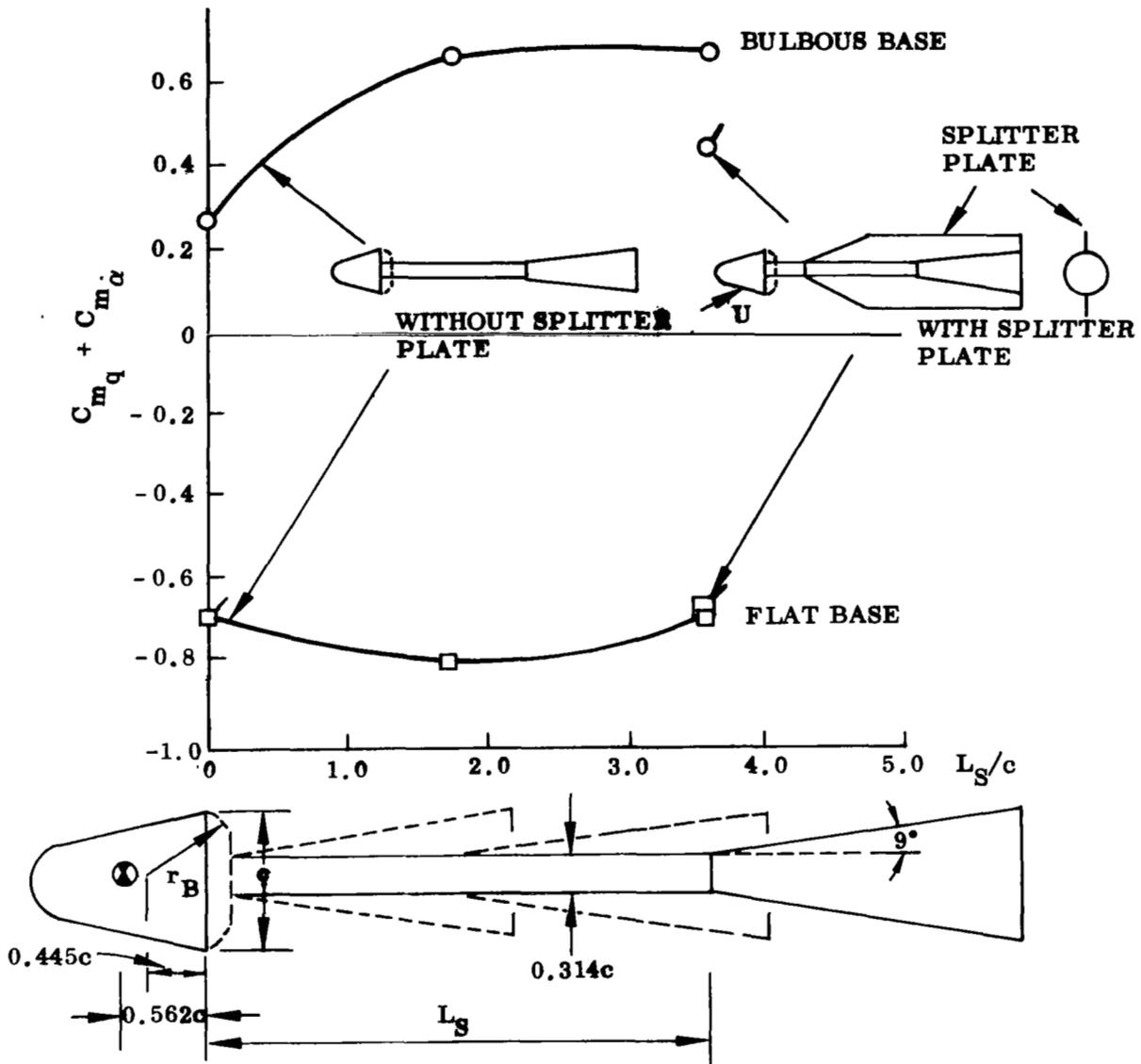
Fig. 38 Effect of Sting Flare and Splitter Plate on Damping, M ≈ 0.65

57

effects of a flared sting are a combination of wake flipping and cylindrical sting interference*. Thus, as the sting size is increased relative to the flare, the cylindrical sting interference tends to dominate**, yielding the damping trend with sting size shown by Wehrend (Fig. 39 and Ref. 49).

2.3.3 The Transverse Rod Support

One obvious solution to the problem of sting support interference is to use a transverse rod support. It has been amply demonstrated that a rod (Ref. 41) or even a slender wire (Ref. 40) located near the separation point can have a profound effect on the wake geometry and, hence, the stability. However, the effect of a forward rod is less clear. Dayman (Ref. 40) shows that at $M = 4.64$, a wire support located at the mid-point of a 30-deg cone serves to shorten the wake neck relative to the free flight cone, whereas at $M = 2.02$ there is no effect of the wire. This leads one to speculate that it may be the interaction of the wire shock with the wake that affects the wake geometry rather than a rod wake-base wake interaction. Certainly, the latter would tend to be less Mach number dependent.

To the best of the authors' knowledge, there exist no clear cut measures of transverse rod interference. Usually one can only compare rod data with sting data. This, however, may not be as futile as it first appears. For example; Fig. 40 reveals that the stability of a rod mounted slender blunted cone differs little from the sting-mounted results. The Langley results for an identical configuration indicate that for this sting length, sting-flare interference should be negligible***, and any sting interference

---

*For very short stings, the flare interference will act like a cylindrical sting producing increased damping (see Fig. 38 for zero length sting). This is the result of the wake flipping being counteracted by a tendency for the windward wake to expand relative to the leeward as the result of differential re-attachment pressures (Refs. 20 and 21)

**Of course, the sting will also serve to retard flipping, and the larger the sting the more the flipping is reduced.

***The Langley data indicate negligible flare interference on the flat based model for a 4.37 caliber sting length (0.7 rotation center in Figs. 29 and 33).
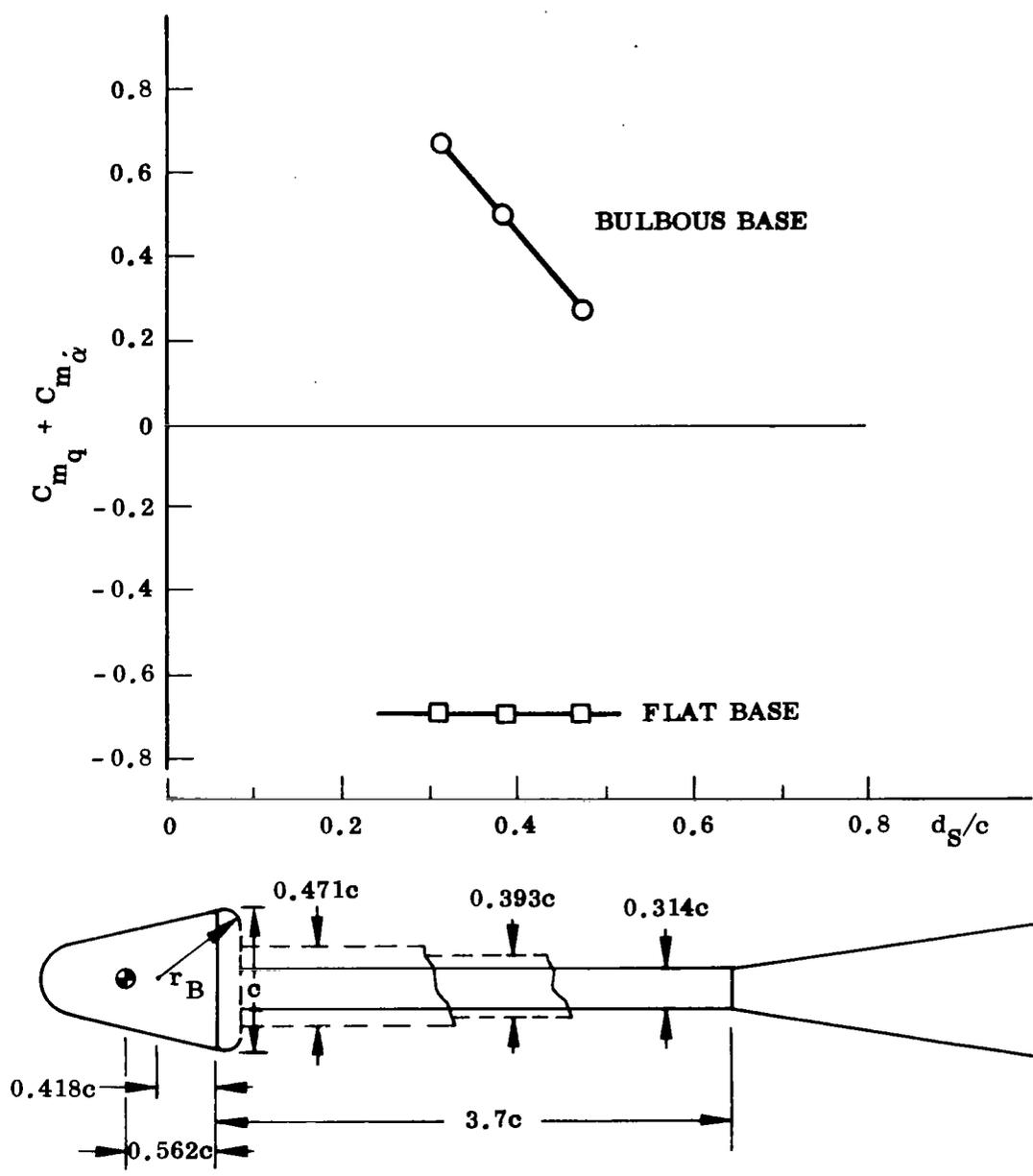
Fig. 39 Effect of Sting Diameter on Damping, M = 0.65
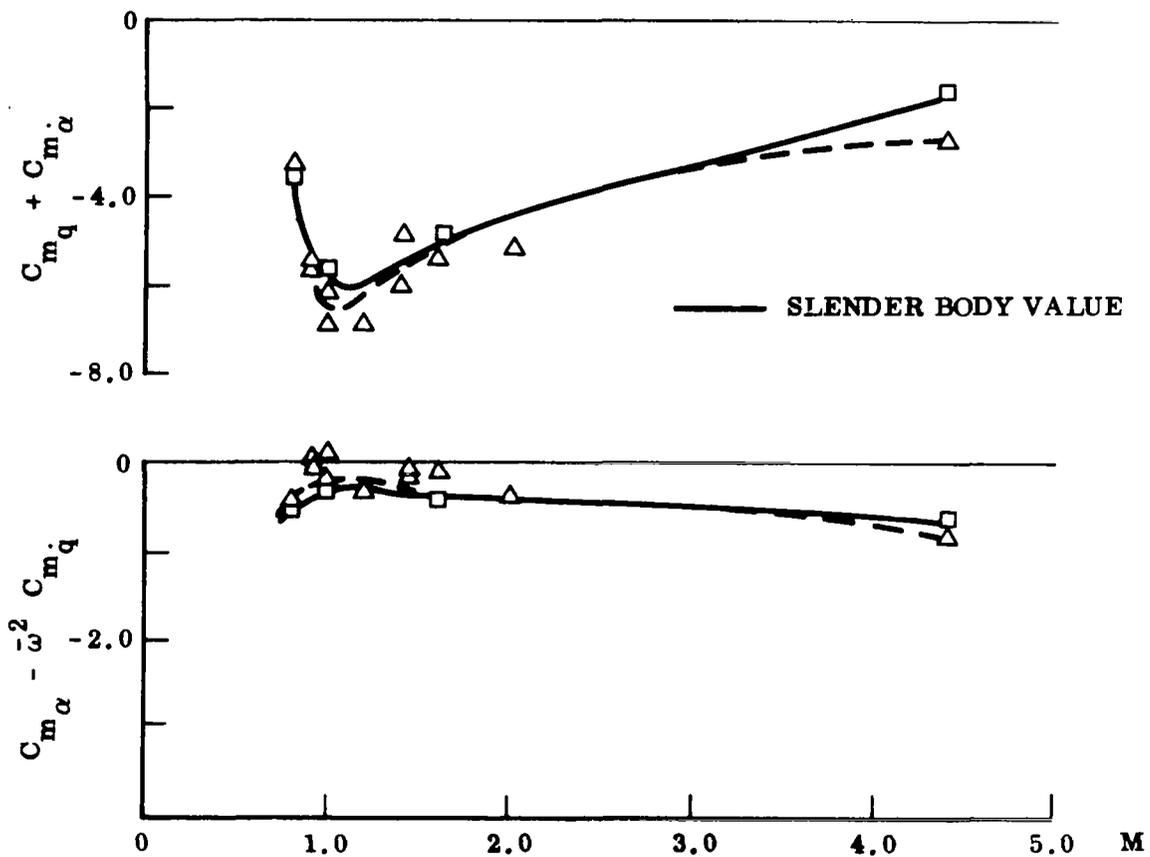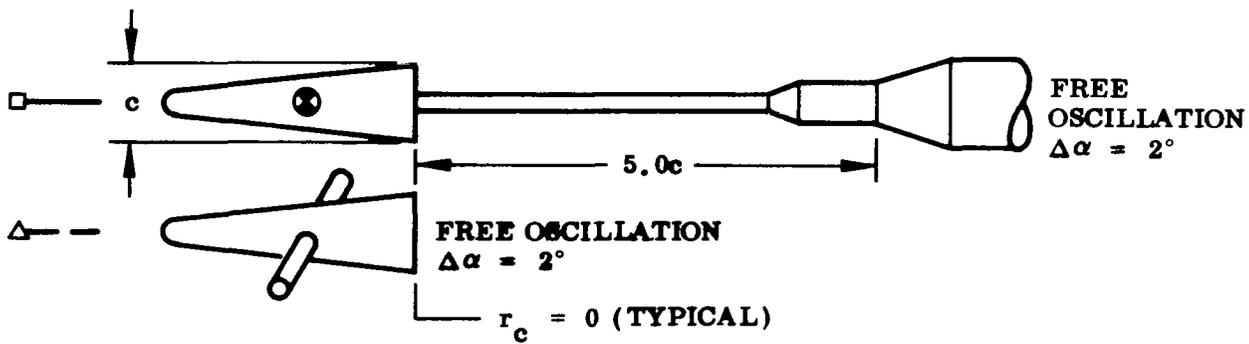
Fig. 40 Effect of Mounting Scheme on Dynamic Stability Results, Flat-Based Model

must be of the cylindrical variety. Any rod interference, whether it is a direct result
of the dynamic pressure in the rod wake or a contribution to the boundary layer collec-
tion, must also be small, since at low amplitudes the rod wake affects only the body
surface near the lateral meridians of the cone which has little effect on the normal loads.

However, the addition of a 0.1 caliber shoulder radius causes unequal sting and rod
interference effects (Fig. 41). It seems reasonable to assume that there is no sig-
nificant interference effect (either rod or sting) on the flat-based models, and that
slender sting interference occurs when shoulder radius is added. Some rod-induced
wake-shortening might also occur, but its effect is certainly small relative to the
sting interference. Thus, there is evidence that subsonic and transonic rod inter-
ference may be negligible for slender blunted cones at small angles-of-attack and
oscillation amplitudes*.

At higher angles-of-attack or oscillation amplitudes rod interference almost certainly
becomes more important. Flat-base sting mounted results reveal no change in
stability with increased oscillation amplitude (from 2 deg to 10 deg) while there is
a drastic change in the rod mounted results (Fig. 42). The high amplitude deviation
of rod-mounted stability (both static and dynamic) is undoubtedly the result of rod
interference. The presence of a time lag is indicated by the opposite static and
dynamic stability increments. The increased static stability for the rod-mounted
model results from the leeward side dynamic pressure reduction via the rod wake
(Fig. 43). The rod wake does not trail directly behind the rod, but is swept upward
as the result of the increased crossflow at the lateral meridians. The crossflow is,
of course, the result of the angle-of-attack. A time lag exists between the instantaneous
model pitch attitude and the realization of the induced-load resulting from the wake
sweeping. The reversal between static and dynamic stability increments is a result of
this time lag (Fig. 42).

---

*Certainly the rod mounted results are closer to the expected free wake results
 assumed earlier when discussing Fig. 27.
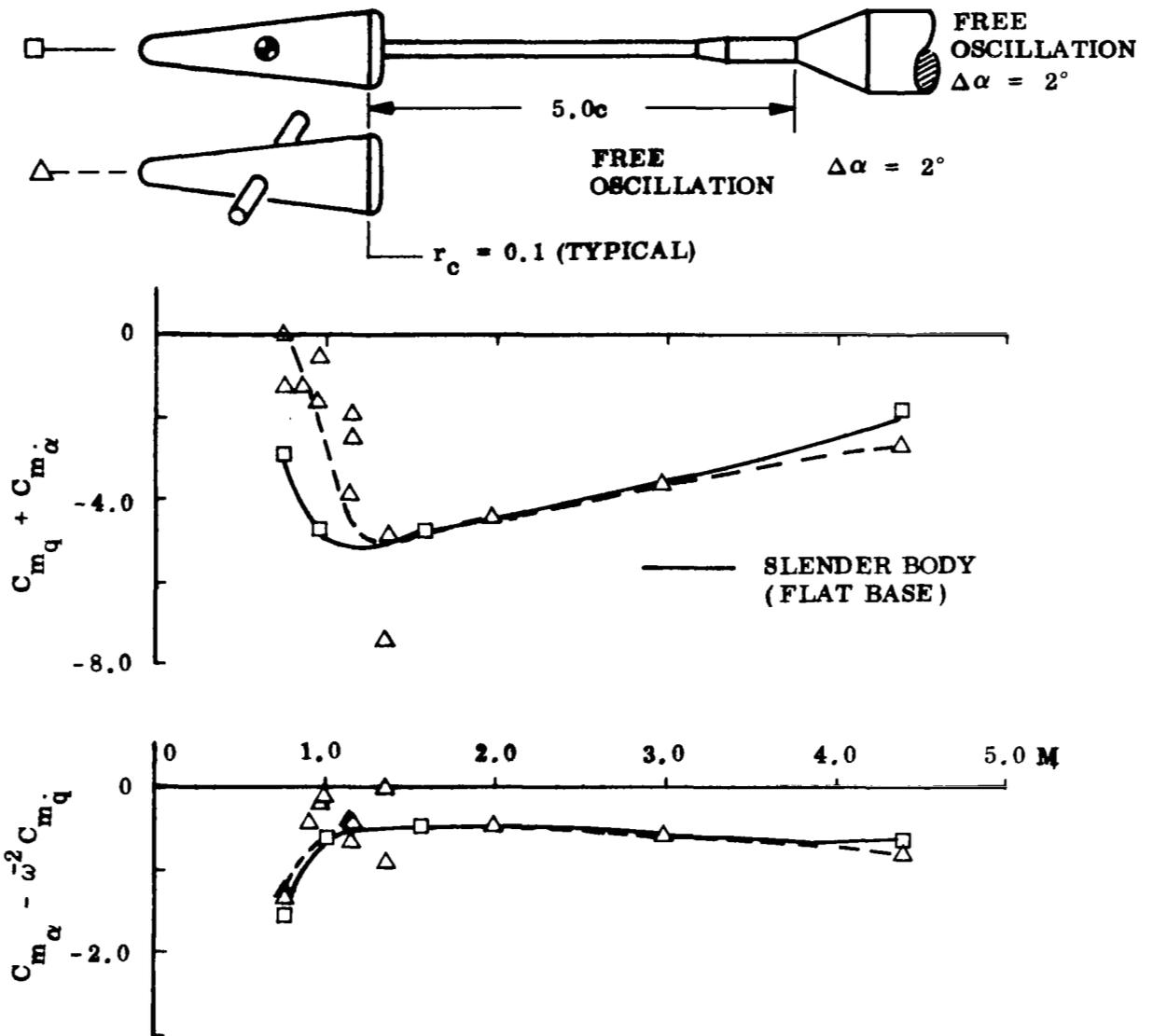
Fig. 41 Effect of Mounting Scheme on Dynamic Stability Results,
0.1 Shoulder Radius
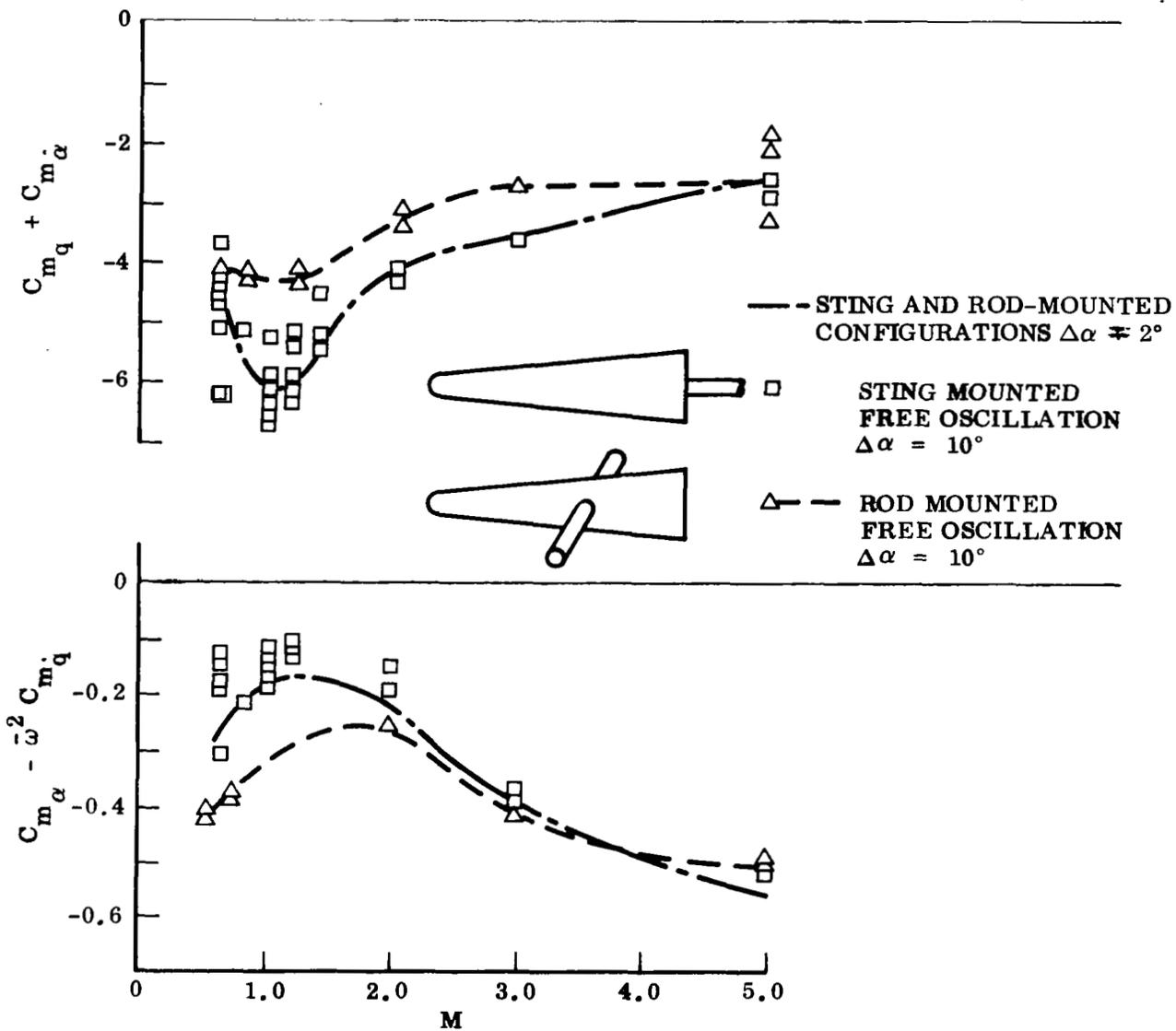
Fig. 42 Effects of Mounting Scheme on Dynamic Stability Results
at Large Amplitudes, Flat Base
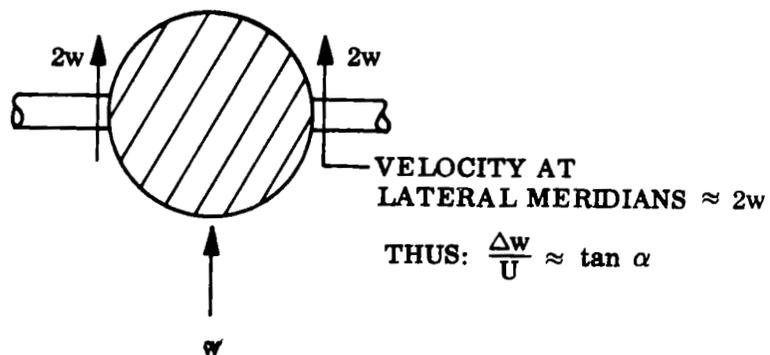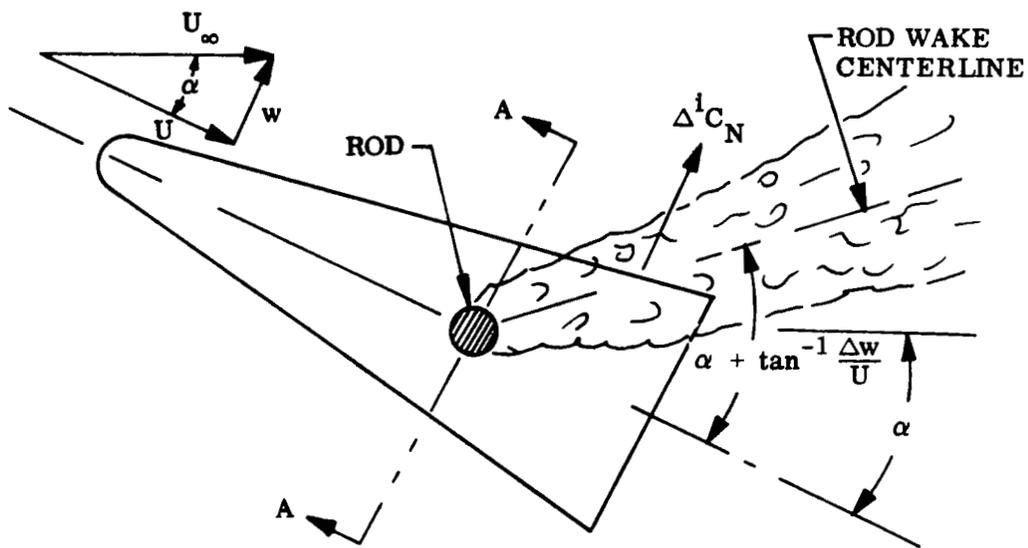
Fig. 43   Rod Wake Interference at Large Angles of Attack

In the light of the preceding discussion, it appears that support interference on bulbous-based configurations is unavoidable with conventional test techniques except for certain special test cases*. Support size may be minimized, but this course of action is restrained by support stiffness requirements to avoid the equally detrimental effects of sting plunging (Ref. 50). Half model testing has been used with success in the past and also more recently on bodies experiencing nose induced separation (Ref. 9) and wake impingement effects (Ref. 51). The problem is, of course, to account for the wall or mounting plate boundary layer, especially in regards to its effect on the near wake flow of the model. (The splitter plate problem discussed earlier). However, it may be possible through careful calibration steps to extrapolate to zero boundary layer thickness. Ballistic range simulation may present equal difficulties since pitch amplitude variations may be modulated by nonlinear Mach number effects due to the large decelerations involved. The free flight tunnel (Ref. 52) offers some improvements, since it allows heavier models (accelerations are lower), thereby reducing deceleration. It also presents better possiblities for deducing nonlinear effects because of its more nearly continuous recording of the model motion. (Camera speed limits the data point density rather than the spacing of discrete camera stations.) However, both the ballistic range and the free flight tunnel have the limitations of all flight tests. The full six-degree-of-freedom flight data do not provide the unambiguous information needed for basic phenomena research, nor do they permit the desired separation of variables. Magnetic suspension may provide a solution, but it faces a considerable development period before it becomes available for routine, production-type testing**. A more profitable solution would be to provide the means to account for the dynamic sting interference***. This could possibly be accomplished by use of quasi-steady analytica. techniques as outlined in the next section.

---

*Such as the slender transverse rod discussed earlier. However, this is by no means a certainty and further investigations must be carried out before this scheme can be used with confidence.

**An interim solution might be to use vertical free flight techniques in a magnetic suspension tunnel (Ref. 52) thereby completely eliminating the effects of deceleration.

***This would also permit correction of already available data.

Section 3
QUASI-STEADY ANALYSIS

The quasi-steady analysis follows the guidelines used earlier (Ref. 7). That is, the quasi-steady force is expressed as the product of a static force derivative and an effective angle-of-attack suitably modified to account for slow perturbations from the steady state value.

3.1 FREE FLIGHT ANALYSIS

In classical quasi-steady theory the force is defined as

$$C_{N_{Q.S.}} = C_N(\alpha_o) + C_{N_\alpha} \tilde{\alpha} \tag{1}$$

where

$\tilde{\alpha}$ = $\theta + \dot{z}/U$

α_o = trim angle of attack

θ = angular perturbation from α_o

$\dot{z}$ = translatory (plunging) velocity

U = vehicle velocity

$\alpha_o + \tilde{\alpha}$ is the local instantaneous cross flow angle. This formulation is valid for aerodynamic forces dependent upon local flow conditions only. As was indicated earlier, however, a large portion of the bulbous base load is dependent upon both upstream and downstream flow conditions. This separation induced loading can be expressed in the following form.

$$\Delta^i C_{N_{Q.S.}}(t) = \Delta^i C_N(\alpha_o) + \Delta^i C_{N_\alpha} \tilde{\alpha}_i(t - \Delta t) \qquad (2)$$

That is, the separation-induced load at time t is determined by the separation-inducing generalized angle of attack at an earlier time, $t - \Delta t$.

If we consider the rigid body in Fig. 44 describing one degree of freedom oscillations in pitch around its C.G., the unsteady aerodynamic load on the bulbous base has the following composition

$$C_{N_B} = C_{N_{B_{att.}}} + \Delta^i C_{N_{B_S}} \qquad (3)$$

where

$$C_{N_{B_{att.}}} = \text{attached flow (boat-tail) load}$$

$$\Delta^i C_{N_{B_S}} = \text{separation induced base load}$$

The separation induced base load has the following composition

$$\Delta^i C_{N_{B_S}} = \Delta_\delta^i C_{N_B} + \Delta_a^i C_{N_B} + \Delta_p^i C_{N_B} + \Delta_c^i C_{N_B} + \Delta_w^i C_{N_B} \qquad (4)$$

$$\Delta_\delta^i C_{N_B} = \text{effect of boundary layer buildup}$$

$$\Delta_a^i C_{N_B} = \text{accelerated flow effect}$$

$$\Delta_p^i C_{N_B} = \text{base plunging effect}$$
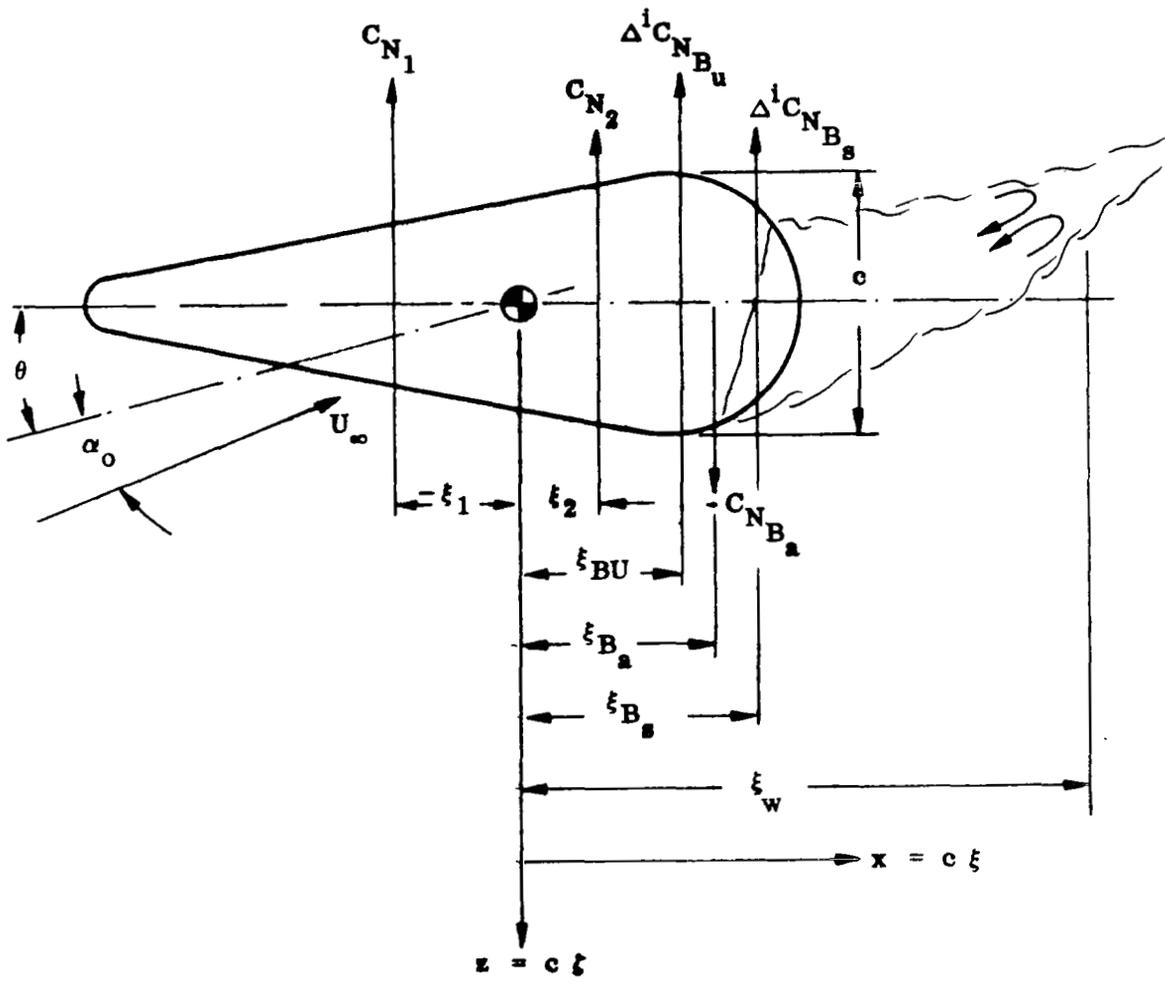
Fig. 44 Coordinate System and Definitions

68

$\Delta_c^i C_{N_B}$ = effect of pitch rate induced apparent base curvature

$\Delta_w^i C_{N_B}$ = effect of upstream communication from the wake recompression

The effect of boundary layer buildup has been described before (Refs. 7, 8, and 33). Following the approach taken in Ref. 33, the forebody cross flow effect is represented by the local crossflow at the lumped (attached flow) load centers ξ_1 and ξ_2. Thus $\Delta_\delta^i C_{N_B}$ becomes

$$\Delta_\delta^i C_{N_B}(t) = \Delta_\delta^i C_{N_B}(\alpha_o) + \Delta_\delta^i C_{N_{\alpha_{B_1}}} \tilde{\alpha}_1(t - \Delta t_1) + \Delta_\delta^i C_{N_{\alpha_{B_2}}} \tilde{\alpha}_2(t - \Delta t_2) \quad (5)$$

where

$$\tilde{\alpha} = \theta + \xi \frac{c\dot{\theta}}{U_\infty}$$

$$\Delta t_1 = c(\xi_{B_s} - \xi_1)/\overline{U}$$

$$\Delta t_2 = c(\xi_{B_s} - \xi_2)/\overline{U}$$

and $\overline{U}$ is the convection velocity in the boundary layer, $0.8 \le \overline{U}/U \le 1$ for a turbulent boundary layer (Refs. 53 and 54).

The accelerated flow effect delays the base separation. When the angle-of-attack is increasing, the flow on the leeward side is accelerated, causing a decrease in the adverse pressure gradient. This lag of the adverse pressure gradient acts similarly to a time lag. The induced force change $\Delta_a^i C_{N_B}$ can be expressed as follows (Refs. 25 and 26).

$$\Delta_a^i C_{N_B} = \frac{\partial \Delta^i C_{N_B}}{\partial P_{\xi_{B_s}}} \frac{\partial P_{\xi_{B_s}}}{\partial \frac{c\dot\alpha}{U_e}} \frac{c\dot\alpha}{U_e} \tag{6}$$

where

$$P_{\xi_{B_s}} = \left(\frac{\partial P}{\partial \xi}\right)_{\xi = \xi_{B_s}}$$

$$U_e = \text{boundary layer edge velocity}$$

The base plunging effect could (for a hemispherical or other round base) be envisioned as sketched in Fig. 45a. That is, the base crossflow angle due to plunging causes a corresponding rotation of the base stagnation point, i.e.,

$$\Delta\varphi \approx \frac{\dot z_{B_s}}{U_\infty} = \xi_{B_s} \frac{c\dot\theta}{U_\infty} \tag{7}$$

and

$$\Delta_p^i C_{N_{B_1}} = \frac{\partial C_{N_B}}{\partial \varphi} \xi_{B_s} \frac{c\dot\theta}{U_\infty} \tag{8}$$

If the base portion embedded in the wake does not have a small axial extent, another base plunging effect is realized (Fig. 45b). It is similar to the subsonic effect on hammerhead boat-tails when the boat-tail is embedded in separated flow (Refs. 55 and 56). The boat-tail acts as a "negative flare" in separated (shear) flow (compare positive flare effect in Refs. 6 and 7), and a negative boat-tail load $\Delta_p^i C_{N_{B_2}}$ is generated. In quasi-steady notation the load can be expressed as follows:
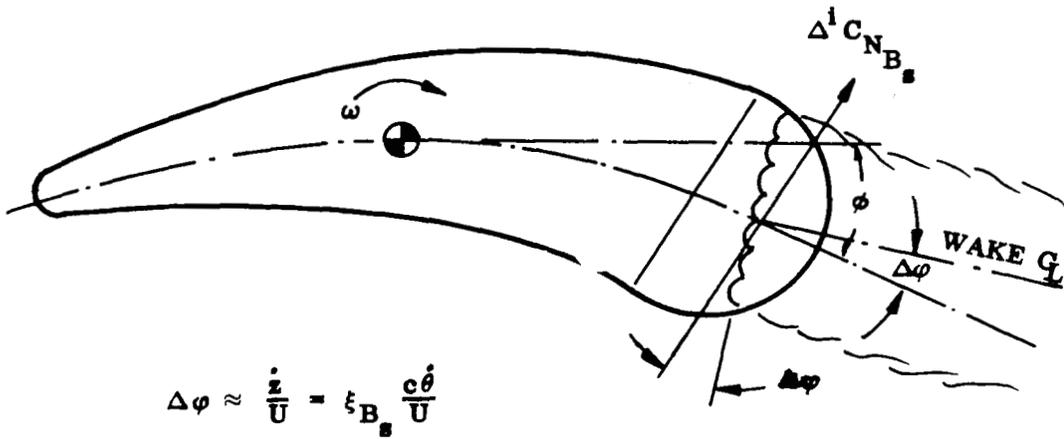
$$\Delta \varphi \approx \frac{\dot{z}}{U} = \xi_{B_s} \frac{c\dot{\theta}}{U}$$

a) BASE PLUNGING EFFECT
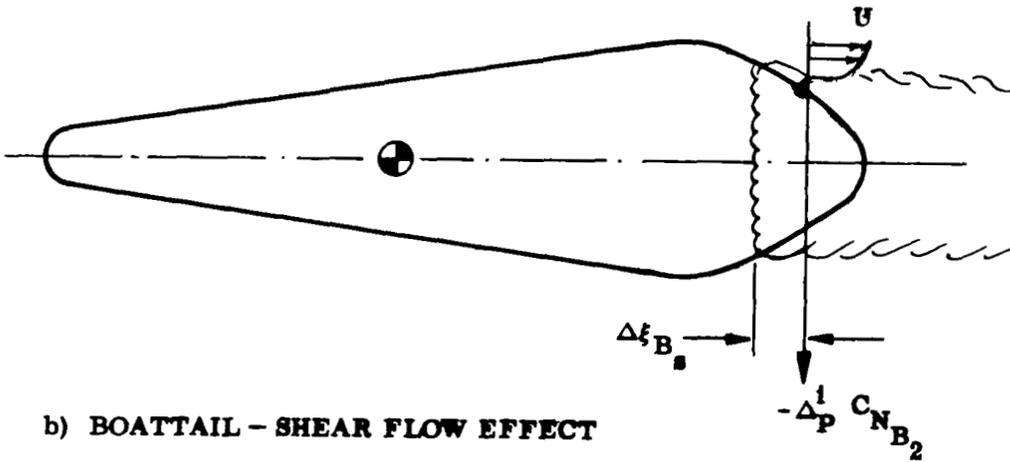
b) BOATTAIL – SHEAR FLOW EFFECT

Fig. 45 Effect of Base Plunging and Taper

$$\Delta_p^i C_{N_{B_2}}(t) = \Delta_p^i C_{N_{B_2}}(\alpha_o) + \Delta_p^i C_{N_{\alpha_{B_2}}} \tilde{\alpha}_{B_s}(t - \Delta t_p) \tag{9}$$

where

$$\tilde{\alpha}_{B_s} = \theta + \xi_{B_s} \frac{c\dot{\theta}}{U_\infty}$$

$$\Delta t_p = c \Delta \xi_{B_s} / \overline{U}_d$$

$\overline{U}_d$ = effective convection velocity in the outer wake.

The pitch rate induced apparent base curvature can be visualized as illustrated in Fig. 46. Because the more aft portions of the base move down faster than the forward portions the flow feels an apparent increase of the bottom base radius and a corresponding decrease of the top radius of curvature. The apparent change ΔR in local radius of curvature is

$$\frac{\Delta R}{R} = \frac{\frac{1}{U_\infty} \frac{\partial \dot{z}}{\partial x}}{\frac{\partial \theta_b}{\partial x}} = \frac{\dot{\theta}}{U_\infty \frac{\partial \theta_b}{\partial x}} \tag{10}$$

This apparent curvature change will cause the separation to be delayed on the bottom of the downgoing base and hastened on the top surface. The corresponding base force $\Delta_c^i C_{N_B}$ can be expressed

$$\Delta_c^i C_{N_B} = \frac{\partial \Delta_c^i C_{N_B}}{\partial R} \frac{R/c}{\left(\frac{\partial \theta_b}{\partial x}\right)_{\xi = \xi_{B_s}}} \frac{c\dot{\theta}}{U_\infty} \tag{11}$$

72
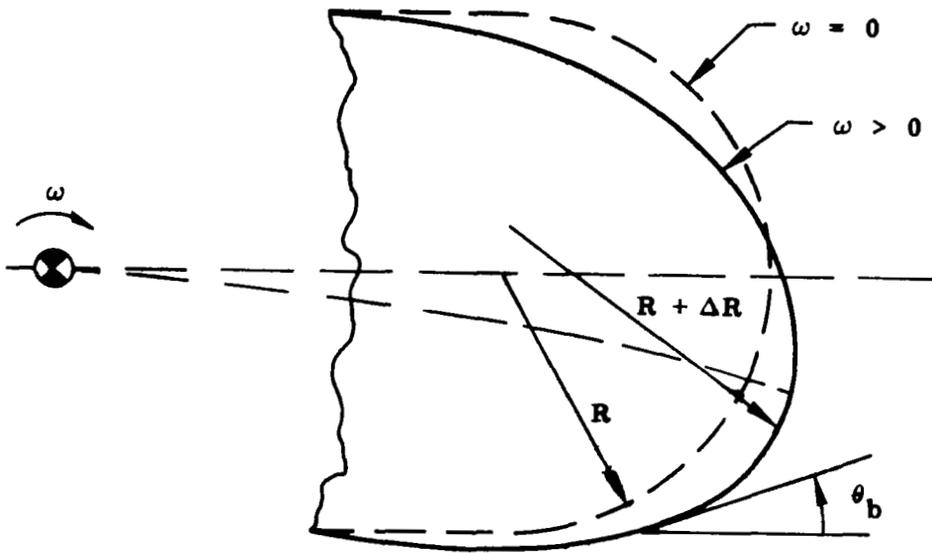
Fig. 46 Effect of Base Curvature

Finally, the effect of upstream communication from the wake recompression is directly related to the forebody lift developed at an earlier time instant. The effect has been described at length earlier in the discussion implying the following expression for $\Delta_w^i C_{N_B}$

$$\Delta_w^i C_{N_B}(t) = \Delta_w^i C_{N_B}(\alpha_o) + \Delta_w^i C_{N_{\alpha_{B_1}}} \tilde{\alpha}_{B_s}\left(t - \Delta t_{w_1}\right) + \Delta_w^i C_{N_{\alpha_{B_2}}} \tilde{\alpha}_{B_u}\left(t - \Delta t_{w_2}\right)$$

(12)

where

$$\tilde{\alpha}_{B_s} = \theta + \xi_{B_s} \frac{c\dot{\theta}}{U_\infty}$$

$$\tilde{\alpha}_{B_u} = \theta + \xi_{B_u} \frac{c\dot{\theta}}{U_\infty}$$

$$\Delta t_{w_1} = \left(\frac{U_\infty}{\overline{U}_d} + \frac{U_\infty}{\overline{U}_u}\right)_1 c\left(\xi_w - \xi_{B_s}\right)\Big/ U_\infty$$

$$\Delta t_{w_2} = \left(\frac{U_\infty}{\overline{U}_d} + \frac{U_\infty}{\overline{U}_u}\right)_2 c\left(\xi_w - \xi_{B_u}\right)\Big/ U_\infty$$

$\overline{U}_d$ = downstream convection velocity in outer wake

$\overline{U}_u$ = upstream convection velocity in inner wake.

For the slow oscillations of interest, $(\omega c/U_\infty)^2 \ll 1$, $\tilde{\alpha}(t - \Delta t)$ can be approximated as follows:

$$\tilde{\alpha}(t - \Delta t) = \theta(t) - \Delta t \dot{\theta}(t) + \xi \frac{c\dot{\theta}(t)}{U_\infty}$$

(13)

74

Defining

$$C_{N_\theta} = \frac{\partial C_N}{\partial \theta}$$

and

$$C_{N_{\dot\theta}} = \frac{\partial C_N}{\partial \left(\dfrac{c\dot\theta}{U_\infty}\right)}$$

Equations (5) through (12) give the following separation induced base force derivatives

$$\left. \begin{aligned} \Delta_\delta^i C_{N_{B_\theta}} &= \Delta_\delta^i C_{N_{\alpha_{B_1}}} + \Delta_\delta^i C_{N_{\alpha_{B_2}}} \\[2em] \Delta_\delta^i C_{N_{B_{\dot\theta}}} &= \Delta_\delta^i C_{N_{B_\theta}} \xi_{B_s} - \frac{U_\infty}{\overline{U}}\left[\Delta_\delta^i C_{N_{\alpha_{B_1}}}\left(\xi_{B_s} - \xi_1\right) + \Delta_\delta^i C_{N_{\alpha_{B_2}}}\left(\xi_{B_s} - \xi_2\right)\right] \end{aligned} \right\} \quad (14)$$

$$\left. \begin{aligned} \Delta_a^i C_{N_{B_\theta}} &= 0 \\[2em] \Delta_a^i C_{N_{B_{\dot\theta}}} &= \frac{\partial \Delta^i C_{N_B}}{\partial P_{\xi_{B_s}}} \frac{\partial P_{\xi_{B_s}}}{\partial \dfrac{c\dot\alpha}{U_e}} \frac{U_\infty}{U_e} \\[2em] P_{\xi_{B_s}} &= \left(\frac{\partial P}{\partial \xi}\right)_{\xi = \xi_{B_s}} \end{aligned} \right\} \quad (15)$$

75

$$\Delta_p^i C_{N_{B_\theta}} = \Delta_p^i C_{N_{\alpha_{B_2}}}$$

$$\Delta_p^i C_{N_{B_{\dot\theta}}} = \frac{\partial C_{N_B}}{\partial \phi} \xi_{B_s} + \Delta_p^i C_{N_{\alpha_{B_2}}} \left(\xi_{B_s} - \Delta\xi_{B_s} \frac{U_\infty}{\overline{\overline{U}}_d} \right)$$

$$\left.\right\} \quad (16)$$

$$\Delta_c^i C_{N_{B_\theta}} = 0$$

$$\Delta_c^i C_{N_{B_{\dot\theta}}} = \frac{\partial \Delta_c^i C_{N_B}}{\partial R} \frac{R/c}{\partial \theta / \partial x}$$

$$\left.\right\} \quad (17)$$

$$\Delta_w^i C_{N_{B_\theta}} = \Delta_w^i C_{N_{\alpha_{B_1}}} + \Delta_w^i C_{N_{\alpha_{B_2}}}$$

$$\Delta_w^i C_{N_{B_{\dot\theta}}} = \Delta_w^i C_{N_{\alpha_{B_1}}} \left[\xi_{B_s} - \left(\frac{U_\infty}{\overline{\overline{U}}_d} + \frac{U_\infty}{\overline{\overline{U}}_u} \right)_1 \left(\xi_w - \xi_{B_s} \right) \right]$$

$$+ \Delta_w^i C_{N_{\alpha_{B_2}}} \left[\xi_{B_u} - \left(\frac{U_\infty}{\overline{\overline{U}}_d} + \frac{U_\infty}{\overline{\overline{U}}_u} \right)_2 \left(\xi_w - \xi_{B_u} \right) \right]$$

$$\Delta_w^i C_{N_{\alpha_B}} = \left[\left(\partial \Delta_w^i C_{N_{\alpha_{B_1}}} \middle/ \partial C_{L_\alpha} \right) + \partial \Delta_w^i C_{N_{\alpha_{B_2}}} \middle/ \partial C_{L_\alpha} \right] C_{L_\alpha}$$

$$\left.\right\} \quad (18)$$

When C_{L_α} reverses sign, e.g., goes negative for a short blunt body, the wake induced effect $\Delta_w^i C_{N_{\alpha_B}}$ would also reverse sign. In addition to $\Delta_w^i C_{N_{\alpha_B}}$ the axial force moment contributions $\Delta_w^i C_{m_{A_{\alpha_B}}}$ would also have to be considered for the short blunt body.

For the slender configuration shown in Fig. 44, the unsteady aerodynamics of the attached flow region forward of the base flow separation (ξ_{B_s}) can be determined using slender body theory (e.g., Ref. 6).

$$\left. \begin{array}{l} C_{N_\theta} = C_{N_\alpha} \\[2em] C_{N_{\dot\theta}} = C_{N_\alpha} \xi_{B_s} \end{array} \right\} \tag{19}$$

The moment derivatives are simply

$$\partial C_m / \partial = -\xi \, \partial C_N / \partial \tag{20}$$

The separation induced forces on the slender configuration in Fig. 44 would mainly be due to boundary layer buildup and wake recompression effects, Eqs. (14) and (18). The base plunging effect is probably not large, Eq. (16). The accelerated flow effect would be small, Eq. (15), compared to the boundary layer buildup effect, Eq. (14) unless the body is of the short blunt variety (Ref. 57). This is also true for the apparent curvature effect, Eq. (17). For a short blunt body, however, this effect could become dominant, at least in some critical Reynolds number range judging by the data in Ref. 58.

Consequently, the unsteady aerodynamic characteristics of the slender body shown in Fig. 44 can be approximated as follows.

77

$$C_{m_{\theta_{total}}} = C_{M_{\alpha_{att.}}} + \Delta^i_\delta C_{m_\alpha} + \Delta^i_w C_{m_\alpha}$$

$$C_{m_{\dot\theta_{total}}} = C_{m_{\dot\theta_{att.}}} + \Delta^i_\delta C_{m_{\dot\theta}} + \Delta^i_w C_{m_{\dot\theta}}$$

$$C_{m_{\alpha_{att.}}} = -\xi_1 C_{N_{\alpha_1}} - \xi_2 C_{N_{\alpha_2}} - \xi_{B_a} C_{N_{\alpha_{B_{att.}}}}$$

$$C_{m_{\dot\theta_{att.}}} = -\xi^2_{B_s}\left(C_{N_{\alpha_1}} + C_{N_{\alpha_2}} + C_{N_{\alpha_{B_{att.}}}} \right)$$

$$\Delta^i_\delta C_{m_\alpha} = -\xi_{B_s}\left(\Delta^i_\delta C_{N_{\alpha_{B_1}}} + \Delta^i_\delta C_{N_{\alpha_{B_2}}} \right)$$

$$\Delta^i_\delta C_{m_{\dot\theta}} = -\xi_{B_s}\left\{ \Delta^i_\delta C_{N_{\alpha_{B_1}}}\left[\xi_{B_s} - \frac{U_\infty}{\overline{\overline{U}}}\left(\xi_{B_s} - \xi_1 \right) \right] \right.$$

$$\left. + \Delta^i_\delta C_{N_{\alpha_{B_2}}}\left[\xi_{B_s} - \frac{U_\infty}{\overline{\overline{U}}}\left(\xi_{B_s} - \xi_2 \right) \right] \right\}$$

$$\Delta^i_w C_{m_\alpha} = -\xi_{B_s} \Delta^j_w C_{N_{\alpha_{B_1}}} - \xi_{B_u} \Delta^i_w C_{N_{\alpha_{B_2}}}$$

(21)

$$\Delta_w^i C_{m_{\dot{\theta}}} = -\xi_{B_s} \Delta_w^i C_{N_{\alpha_{B_1}}} \left[\xi_{B_s} - \left(\frac{U_\infty}{\overline{\overline{U}}_d} + \frac{U_\infty}{\overline{\overline{U}}_u} \right)_1 \left(\xi_w - \xi_{B_s} \right) \right]$$

$$-\xi_{B_u} \Delta_w^i C_{N_{\alpha_{B_2}}} \left[\xi_{B_u} - \left(\frac{U_\infty}{\overline{\overline{U}}_d} + \frac{U_\infty}{\overline{\overline{U}}_u} \right)_2 \left(\xi_w - \xi_{B_u} \right) \right] \qquad (21)$$

where

$$1.0 \leq \frac{U_\infty}{\overline{\overline{U}}} \leq 1.25$$

$$1.0 \leq \frac{U_\infty}{\overline{\overline{U}}_d} < \frac{U_\infty}{\overline{\overline{U}}_u}$$

$$\Delta_w^i C_{N_{\alpha_{B_1}}} = \frac{\partial \Delta_w^i C_{N_{\alpha_{B_1}}}}{\partial C_{L_\alpha}} C_{L_\alpha}$$

$$\Delta_w^i C_{N_{\alpha_{B_2}}} = \frac{\partial \Delta_w^i C_{N_{\alpha_{B_2}}}}{\partial C_{L_\alpha}} C_{L_\alpha}$$

For base shapes that do not carry loads contributing to the pitching moment, e. g. , for the small shoulder roundness type base or the spherical base segment with its center coinciding with the oscillation center, the only induced effect of consequence is the upstream communication from the wake recompression to the area forward of the rounded base, i. e. , the effect of $\Delta_w^i C_{N_{\alpha_{B_2}}}$. We believe this to be the dominant undamping effect caused by a bulbous base on a slender vehicle. Consequently, efforts should be concentrated on obtaining the information necessary to better understand and

predict this upstream communication effect. However, this task is immeasurably complicated by the problem of support interference.

3.2 SUPPORT INTERFERENCE ANALYSIS

The sting support will, of course, affect the upstream communication effect from the wake recompression, while the rod interference will interact more with the boundary layer buildup effect $\Delta_\delta^i C_{N_B}$. Considering the dynamic sting interference first, the following interference effects can be defined (see Fig. 47).

$$\left(\Delta^i C_{N_{B_s}} \right)_{STD} = \left(\Delta_w^i C_{N_{B_s}} \right)_{SC} + \left(\Delta_w^i C_{N_{B_s}} \right)_{SF} \tag{22}$$

where

$$\left(\Delta_w^i C_{N_{B_s}} \right)_{SC} = \text{cylindrical sting interference (Fig. 47a)}$$

$$\left(\Delta_w^i C_{N_{B_s}} \right)_{SF} = \text{sting flare interference (Fig. 47b)}$$

The cylindrical sting interference (Fig. 47a) can in quasi-steady notation be expressed as

80
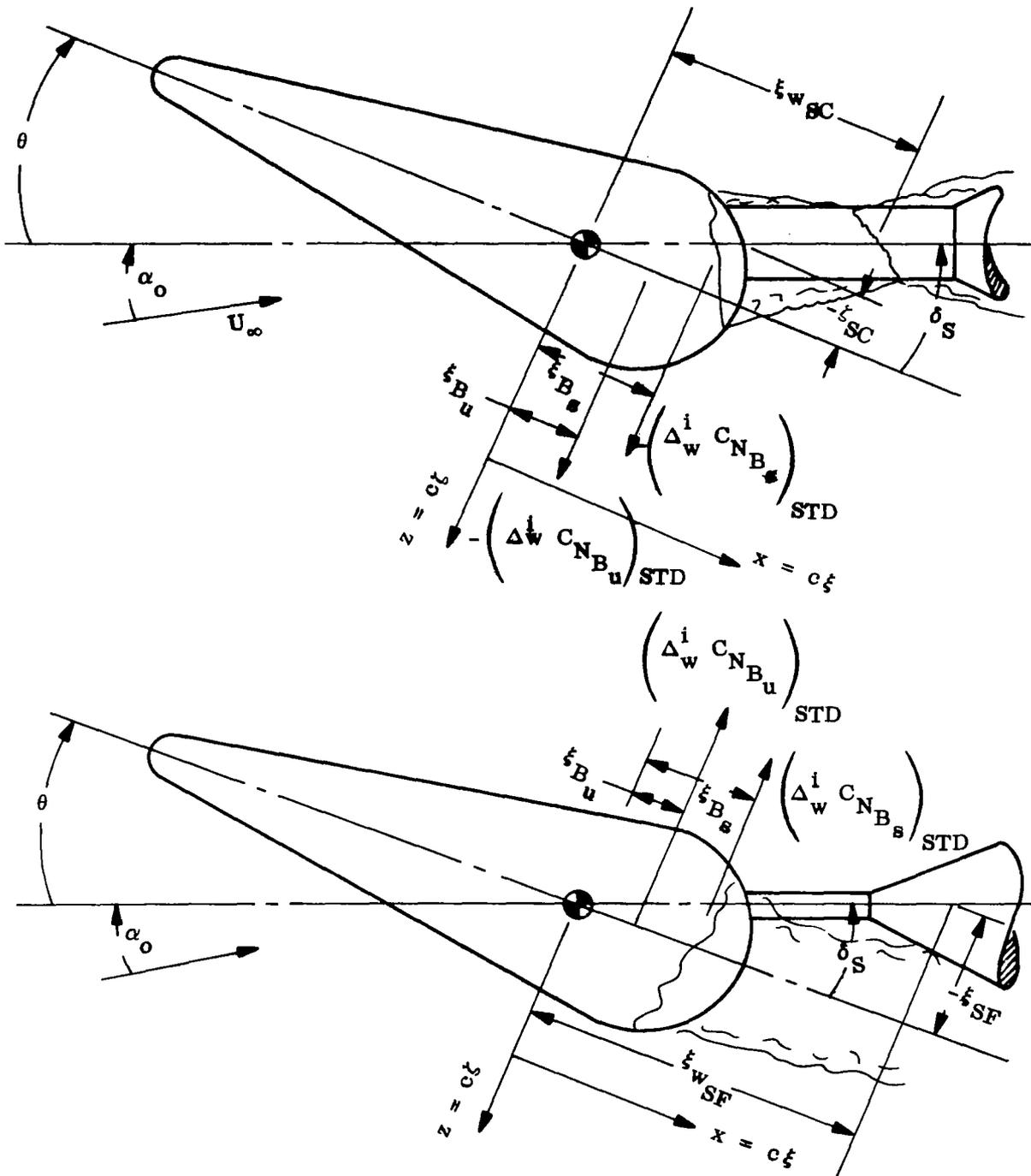
Fig. 47 Sting Interference Loads

$$\left[\Delta_w^i C_{N_{B_s}}(t)\right]_{SC} = \left[\Delta_w^i C_{N_{B_s}}(\alpha_o)\right]_{SC} + \left(\Delta_w^i C_{N_{\alpha_{B_s}}}\right)_{SC} \tilde{\alpha}_{B_s}\left(t - \Delta t_{1_{SC}}\right)$$

$$+ \left(\Delta_w^i C_{N_{\alpha_{B_u}}}\right)_{SC} \tilde{\alpha}_{B_u}\left(t - \Delta t_{2_{SC}}\right)$$

<div align="right">(23)</div>

where

$$\tilde{\alpha}_{B_s} = \theta + \xi_{B_s}\frac{c\dot{\theta}}{U_\infty}$$

$$\tilde{\alpha}_{B_u} = \theta + \xi_{B_u}\frac{c\dot{\theta}}{U_\infty}$$

$$\Delta t_{1_{SC}} = \left(\frac{U_\infty}{\overline{U}_d} + \frac{U_\infty}{\overline{U}_u}\right)_{1_{SC}} c\left(\xi_{w_{SC}} - \xi_{B_s}\right)\Big/ U_\infty$$

$$\Delta t_{2_{SC}} = \left(\frac{U_\infty}{\overline{U}_d} + \frac{U_\infty}{\overline{U}_u}\right)_{2_{SC}} c\left(\xi_{w_{SC}} - \xi_{B_u}\right)\Big/ U_\infty$$

Likewise the sting flare interference can be expressed as

$$\left[\Delta_w^i C_{N_{B_s}}(t)\right]_{SF} = \left[\Delta_w^i C_{N_{B_s}}(\alpha_o)\right]_{SF} + \left(\Delta_w^i C_{N_{\alpha_{B_s}}}\right)_{SF} \alpha_{B_s}\left(t - \Delta t_{1_{SF}}\right)$$

$$+ \left(\Delta_w^i C_{N_{\alpha_{B_u}}}\right)_{SF} \tilde{\alpha}_{B_u}\left(t - \Delta t_{2_{SF}}\right) \quad (24)$$

where

$\tilde{\alpha}_{B_s}$ and $\tilde{\alpha}_{B_u}$ are the same as in Eq. (23)

$$\Delta t_{1_{SF}} = \left(\frac{U_\infty}{\overline{U}_d} + \frac{U_\infty}{\overline{U}_u}\right)_{1_{SF}} c\left(\xi_{w_{SF}} - \xi_{B_s}\right)\Big/U_\infty$$

$$\Delta t_{2_{SF}} = \left(\frac{U_\infty}{\overline{U}_d} + \frac{U_\infty}{\overline{U}_u}\right)_{2_{SF}} c\left(\xi_{w_{SF}} - \xi_{B_u}\right)\Big/U_\infty$$

As was pointed out earlier, the cylindrical sting interference, Eq. (23), and the sting flare interference, Eq. (24), oppose each other. The sting interference α-derivatives can be expressed as*

$$\left(\Delta_w^i C_{N_{\alpha_B}}\right)_{STD} = \frac{\partial}{\partial \delta_S}\left(\Delta_w^i C_{N_B}\right)_{STD} + \frac{\partial}{\partial \xi_{STD}}\left(\Delta_w^i C_{N_B}\right)_{STD} \frac{\partial \xi_{STD}}{\partial \delta_S} \quad (25)$$

---

*Throughout the report, perturbations around the trim angle α_o are considered, i.e., all derivaties are, as a rule, functions of α_o.

For the cylindrical sting interference both the direct δ_S-effect and the ζ_S-effect are in the same direction. This is also true about the sting flare interference, if the flare is symmetric. If the sting flare is asymmetric, however, the sting flare interference will no longer by symmetric about $\alpha = 0$ and $\delta_S = 0$, but there will be an $\alpha - \delta_S$-region in which the δ_S and ζ_S-effects oppose each other. The result is a zero shift to a non-zero $(\alpha - \delta_S)$-symmetry point as was discussed in the previous section.

Again, using the slow oscillation approximation [Eqs. (13) and (18) earlier], gives the following sting induced base force derivatives.

$$\left(\Delta_w^i C_{N_{B_\theta}} \right)_{STD} = -\Delta_{STD} C_{N_{\alpha_{B_{att}}}} + \left(\Delta_w^i C_{N_{\alpha_{B_s}}} \right)_{SC} + \left(\Delta_w^i C_{N_{\alpha_{B_u}}} \right)_{SC}$$

$$+ \left(\Delta_w^i C_{N_{\alpha_{B_s}}} \right)_{SF} + \left(\Delta_w^i C_{N_{\alpha_{B_u}}} \right)_{SF}$$

$$\left(\Delta_w^i C_{N_{B_{\dot{\theta}}}}\right)_{STD} = -\xi_{B_a} \Delta_{STD} C_{N_{\alpha_{B_{att}}}} - \left(\Delta_w^i C_{N_{\alpha_{B_s}}}\right)_{SC} \left(\frac{U_\infty}{\overline{\overline{U}}_d} + \frac{U_\infty}{\overline{\overline{U}}_u}\right)_{1_{SC}} \left(\xi_{w_{SC}} - \xi_{B_s}\right)$$

$$- \left(\Delta_w^i C_{N_{\alpha_{B_u}}}\right)_{SC} \left(\frac{U_\infty}{\overline{\overline{U}}_d} + \frac{U_\infty}{\overline{\overline{U}}_u}\right)_{2_{SC}} \left(\xi_{w_{SC}} - \xi_{B_u}\right)$$

$$- \left(\Delta_w^i C_{N_{\alpha_{B_s}}}\right)_{SF} \left(\frac{U_\infty}{\overline{\overline{U}}_d} + \frac{U_\infty}{\overline{\overline{U}}_u}\right)_{1_{SF}} \left(\xi_{w_{SF}} - \xi_{B_s}\right)$$

$$- \left(\Delta_w^i C_{N_{\alpha_{B_u}}}\right)_{SF} \left(\frac{U_\infty}{\overline{\overline{U}}_d} + \frac{U_\infty}{\overline{\overline{U}}_u}\right)_{2_{SF}} \left(\xi_{w_{SF}} - \xi_{B_u}\right) \tag{26}$$

where $\Delta_{STD} C_{N_{\alpha_{B_{att}}}}$ is the reduction of attached flow boat-tail load due to the sting interference effect on the flow separation (geometry) at $\alpha = \alpha_o$ and $\theta = \delta_S = 0$.

The moment derivatives are, of course, simply obtained as $\partial C_m = -\xi \partial C_n$

The rod interference can be derived simply as follows (see Fig. 48). Neglecting the effects of boundary layer crossflow, or lumping those effects at the oscillation center (the rod), the location of the rod wake on the base (or aft body) can be expressed as

$$\bar{\xi}_R (t) = \frac{\partial \bar{\xi}_R}{\partial \alpha} \tilde{\alpha}_R (t - \Delta t_R) \tag{27}$$

85
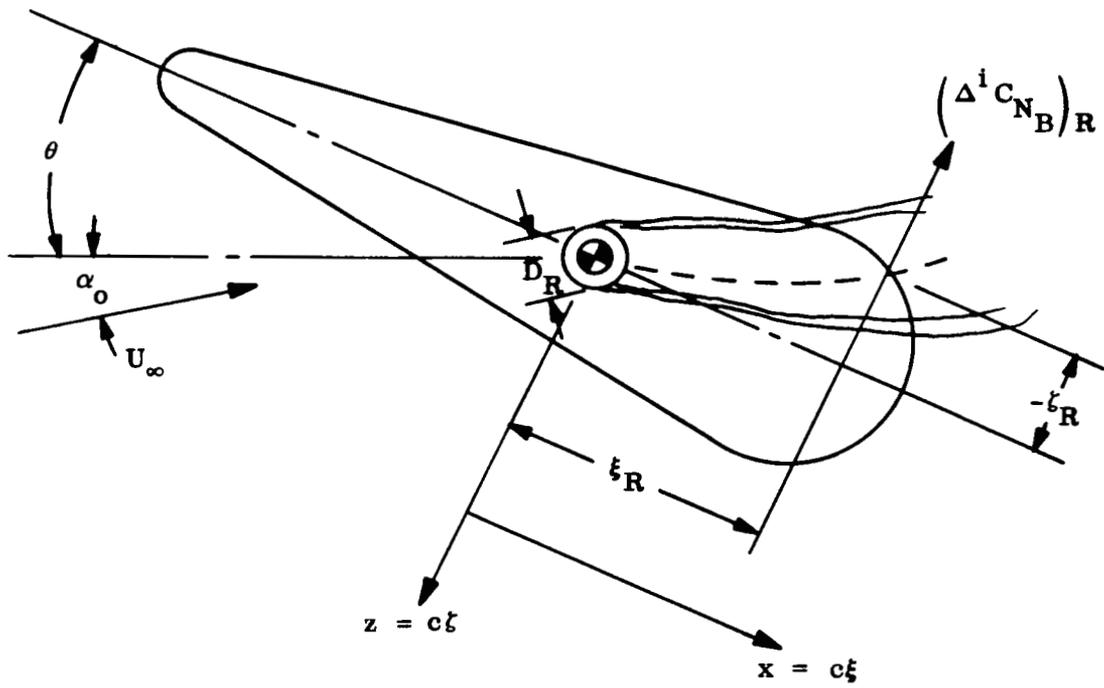
Fig. 48 Rod Interference Loads

where

$$\tilde{\alpha}_R = \alpha_o + \theta$$

$$\Delta t_R = c\,\bar{\xi}_R/U_e \quad *$$

The rod wake causes a reduction of dynamic pressure Δq which has the following interference effect on the base force.

$$\left[\Delta^i C_{N_B}(t)\right]_{RD} = \frac{\left(\frac{\partial \Delta^i C_{N_B}}{\partial \bar{\xi}_R}\right)_R \frac{\partial \bar{\xi}_R}{\partial \alpha} \tilde{\alpha}_R (t - \Delta t_R)}{\partial \bar{\xi}_R} - \Delta_{RD} C_{N_{B_{att}}} \tag{28}$$

or in derivative form

$$\left(\Delta^i C_{N_{B_\theta}}\right)_{RD} = -\Delta_{RD} C_{N_{\alpha_{B_{att}}}} + \left(\Delta^i C_{N_{\alpha_B}}\right)_R$$

$$\tag{29}$$

$$\left(\Delta^i C_{N_{B_{\dot\theta}}}\right)_{RD} = -\xi_{B_a} \Delta_{RD} C_{N_{\alpha_{B_{att}}}} - \left(\Delta^i C_{N_{\alpha_B}}\right)_R \xi_R U_e/U_\infty$$

where

$$\Delta_{RD} C_{N_{\alpha_{B_{att}}}} = \text{reduction of attached flow boat-tail load due to the dynamic}$$
$$\text{pressure reduction caused by the rod wake.}$$

$$\left(\Delta^i C_{N_{\alpha B}}\right)_R = \text{effect of local dynamic pressure reduction, i.e.,}$$

---

*Even if $\alpha_o \neq 0$, α_o is assumed small throughout this report, allowing small angle approximations.

$$\left(\Delta^i C_{N_{\alpha_B}} \right)_R = \left(\frac{\Delta \bar{q}}{q_\infty} \right) \overline{C}_p \frac{\partial S_{R_N}}{\partial \bar{\zeta}_R} \frac{\partial \bar{\zeta}_R}{\partial \alpha} \qquad (30)$$

where

$\Delta \bar{q}/q_\infty$ = effective (integrated) reduction of local dynamic pressure over the rod wake interaction area.

$\overline{C}_p$ = effective (integrated) pressure coefficient over the rod wake interaction area without the rod.

S_{R_N} = effective (integrated) normal force producing horizontal projection of the rod wake interaction area

$\bar{\zeta}_R$ = centroid of rod wake interaction area

In addition to these direct (first order) effects of the rod wake, the rod wake may also interact with the base wake. A change in base wake geometry may well result (Refs. 40 and 41). It is, of course, also possible that the rod wake will couple with both the boundary layer buildup effect and the effect of upstream communication from the base wake recompression. It seems reasonable to believe that Eqs. (28) through (30) could include the changes in boundary layer buildup effects, i.e., one can assume that the superimposition principle is applicable. The coupling with the base wake effect could at $\alpha = 0$ be assumed to consist mainly in a change of basic wake configuration, without introduction of any additional mathematics. At non-zero trim angles α_o, however, or at large oscillation amplitudes, the rod wake may introduce an additional communication link for the wake recompression effect. That is, the rod wake "opens up" the upstream communication. This effect might be appreciable in hypersonic low density flow, when the effect on the viscous rod wake is augmented by the rod shock induced entropy wake. However, if we concentrate the area of interest to transonic Mach numbers, Eqs. (28) through (30) should suffice to give a satisfactory first account of the rod interference. As was pointed out earlier, the rod interference is probably negligible for low angles-of-attack and oscillation amplitudes.

88

3.3 CORRECTION FOR SUPPORT INTERFERENCE

Although it is possible to compute the aerodynamic damping of a bulbous based body, given sufficient static information, obtaining the necessary static results is another matter. For example, even with detailed force distributions it is impossible to determine how much of the load at separation is the result of forebody viscous effects $\left(\Delta_\delta^i C_{m_B}\right)$ and how much is due to upstream wake effects $\left(\Delta_w^i C_{m_B}\right)$. With the right combination of static and dynamic results, it is theoretically possible to predict the free flight dynamics. By measuring the support interference loads statically (the technique used for the Langley tests), one can eliminate the interference loads from the dynamic results (providing sufficient time lag information is available) thereby providing an estimate of free flight aerodynamic damping characteristics. Care must be taken to keep the support system small so as not to have too great an effect on the convection velocity or the base flow separation geometry. Subtracting the interference derivatives, Eqs. (22) through (30), from the measured results would then give the corrected interference-free derivatives.

In applying this technique to the Langley results, an anomaly between the static and dynamic measurements for the static stability parameter immediately becomes apparent. Because of the different measuring techniques (Fig. 26) the static moment coefficient equivalent to the static stability parameter from the forced oscillation tests is

$$
C_{m_\alpha} - \bar{\omega}^2 C_{m_{\dot{q}}} = \left(C_{m_\alpha}\right)_{\delta_S = 0} + \left(C_{m_{\delta_S}}\right)_{\alpha = 0}
$$

Good agreement was obtained between this value and the measured quantity where the support interference was small but it quickly degenerated when the support interference increased (compare Figs. 49 and 33). This is the result of the support asymmetry and the large nonlinear and asymmetric sting flare interference. Where the support interference is the largest, it is also discontinuous and complicated by hysteresis effects,
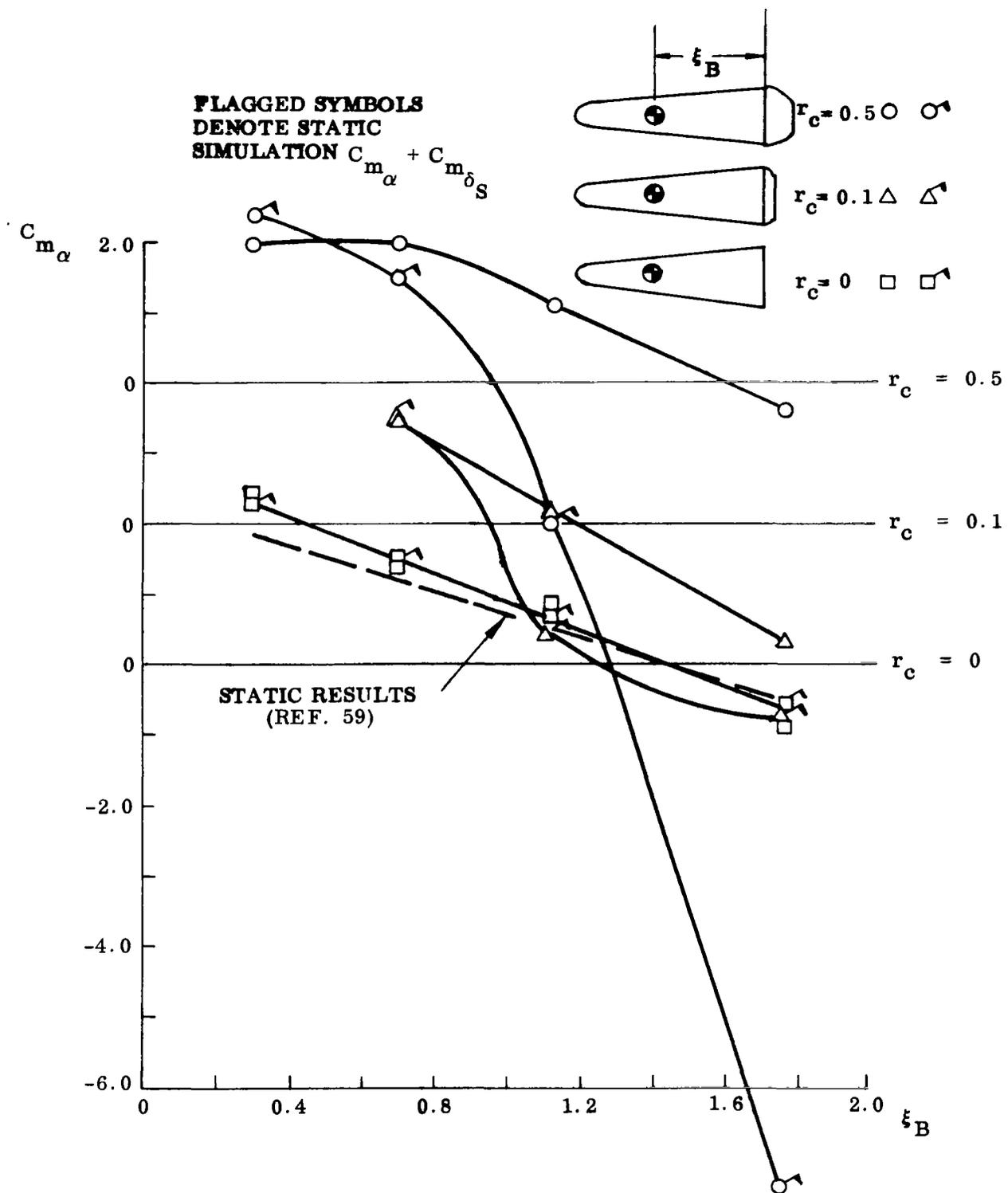
Fig. 49 Comparison of Static Stability Parameter $\left(C_{m_\alpha}\right)$ Measured with with Forced Oscillation and Conventional Static Force Techniques, M = 0.26

and poor agreement results at $M = 0.26$ and 0.6 for the hemispherical base, compare Fig. 5 with Figs. 32 and 46). The wake is unstable and will not remain centered on the sting flare. The initial asymmetry is enough to flip the wake to one side, where it remains throughout the oscillation. Thus, the dynamic results are better simulated by assuming a $C_{\overline{m}_\alpha}$ and $C_{\overline{m}_{\delta_S}}$ outside the range where the derivatives are discontinuous. Much better agreement with the dynamic results is obtained when these biased wake effects are considered in selecting the interference moment $C_{m_{\delta_S}}$ to be used when correcting for support interference (Fig. 50). That is, $C_{\overline{m}_\alpha} + C_{\overline{m}_{\delta_S}}$ must be matched with $C_{m_\alpha} - \overline{\omega}^2 C_{m_{\dot{q}}}$ to determine the correct $C_{m_{\delta_S}}$ to use when correcting for support interference. Thus, in Fig. 51 $C_{\overline{m}_\alpha}$ for $\delta_S = -2$ deg and $C_{\overline{m}_{\delta_S}}$ for 1 deg $< \alpha < 2$ deg was used for $0 < \alpha < 5$ deg and $C_{\overline{m}_\alpha}$ for $\delta_S = 0$ and $C_{\overline{m}_{\delta_S}}$ for $0 < \alpha < 1$ deg was used for $\alpha > 6$ deg.

The Langley results for the hemispherical base model were corrected for sting interference effects in this manner (Fig. 52). The results show a definite undamping trend relative to the flat base despite the large experimental uncertainty. However, the undamping does not increase consistently for more forward rotation centers as one would expect. This is probably the result of assuming constant recirculation velocity within the wake (i.e., the upstream convection velocity was assumed to equal the maximum recirculation velocity with a free wake*). While assumption of constant upstream convection velocity is valid for a cylindrical sting, it is certainly not valid for the flared sting, since the recirculation velocity will increase with the proximity to the sting flare relative to what it would be on a cylinder sting or in the free wake.

The quasi-steady technique shows promise as a means for accounting for support interference effects, but it by no means presents a universal solution to the problem. As illustrated by the foregoing discussion, the interference effects are complicated by such things as support asymmetry, thereby requiring much interpretation of the static results before they can be used in an estimation of the free flight dynamics. Some means of predicting and measuring the wake convection velocities is also needed before

---

*It was also assumed that $(\xi_B - \xi_W) \approx 3.3$ (the distance between the flat based model traveling edge and the sting asymmetry, (Fig. 30) and also that $\overline{U}_d = U_\infty$
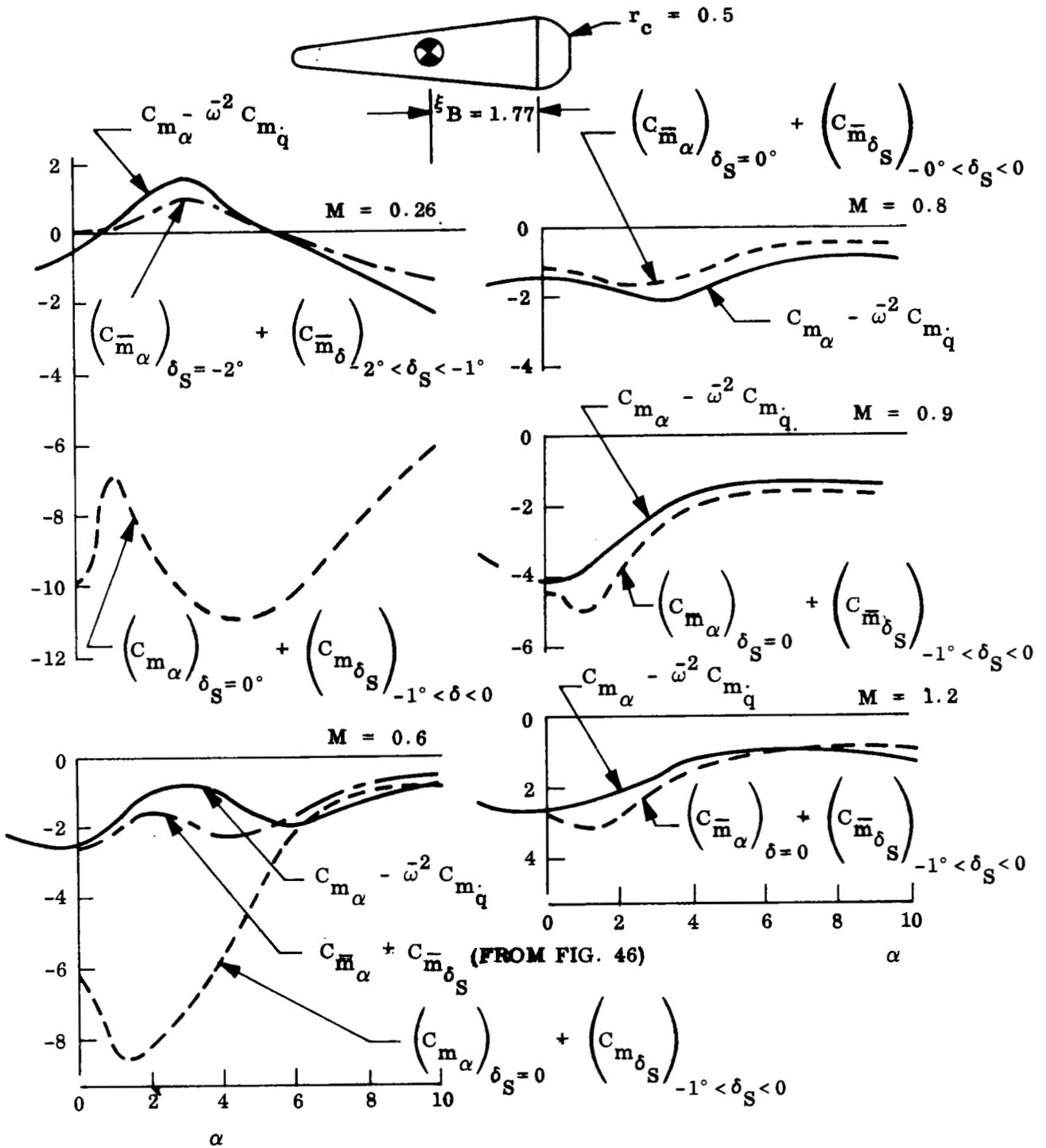
Fig. 50 Correlation of Static Stability Results

$\delta_S < 0°$

U_∞

$\Delta^i C_N$

δ_S - EFFECT DOMINATES
WAKE STICKS TO LEEWARD

REGION OF
WAKE FLIPPING

$\delta_S = 0$

$\delta_S = -1°$

$\delta_S = -2°$

C_m

0.12

0.08

0.04

-0.04

-0.08

$\alpha + \delta_S$

10

9

8

7

6

5

4

3

2

1

α

α

U_∞

$\Delta^i C_N$

α - EFFECT DOMINATES
WAKE FLIPS TO WINDWARD
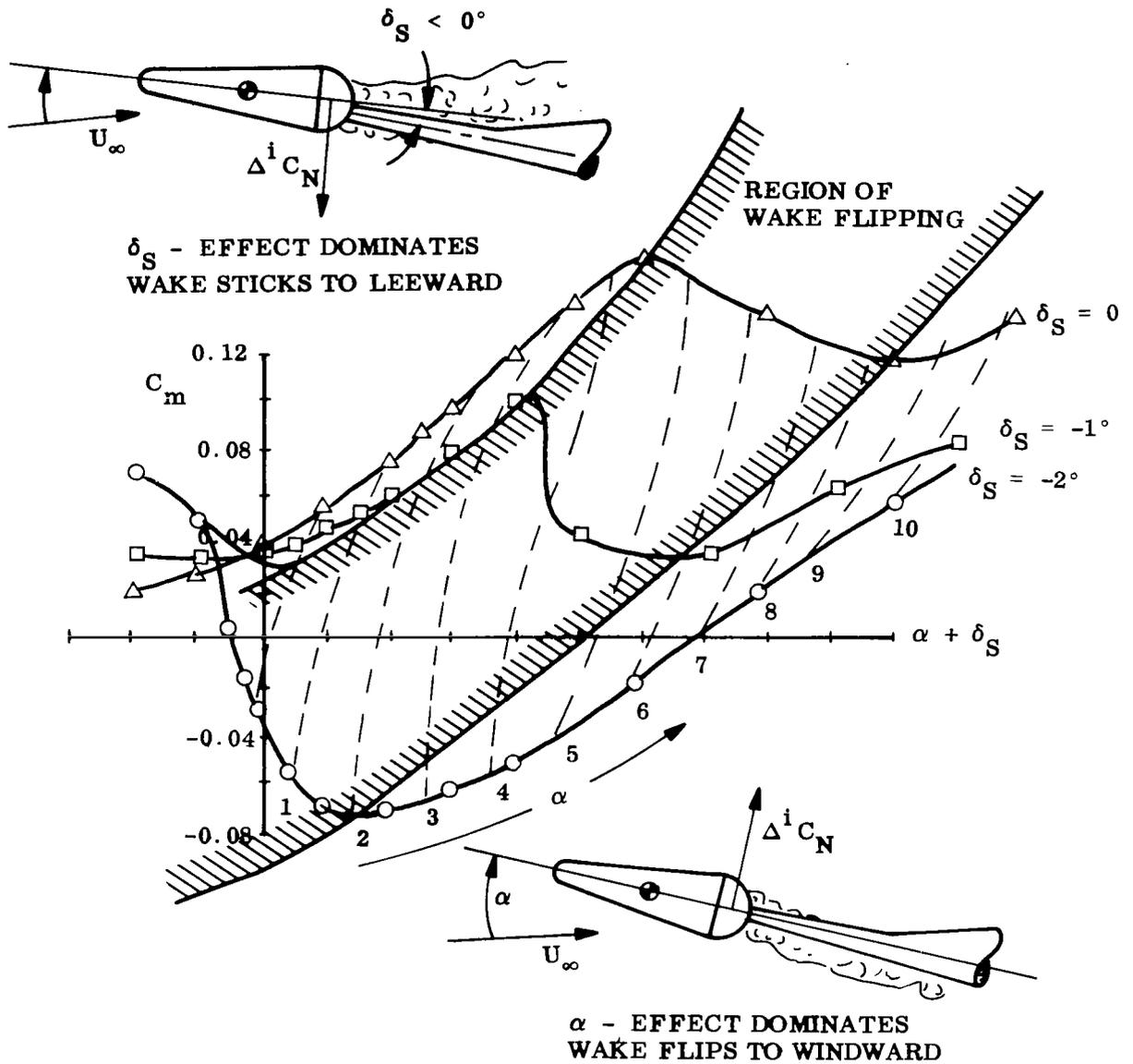
Fig. 51 Unsteady Flow Characteristics, Hemispherical Base, M = 0.6 , ξ_B = 1.77
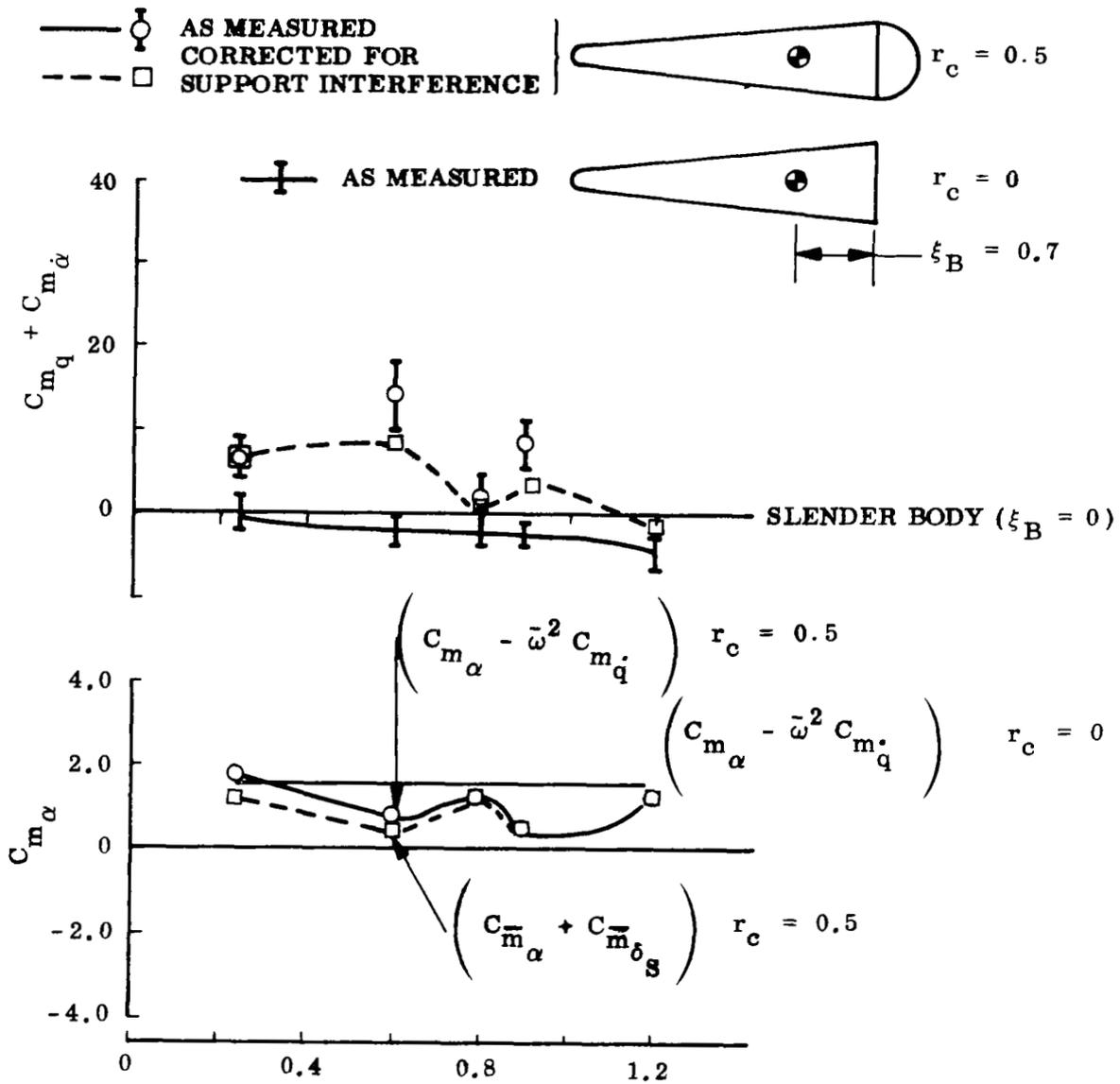
Fig. 52a Damping of Hemispherical Based Body with Support Interference
Effects Eliminated, $\alpha = 0$, $\xi_B = 0.7$

94
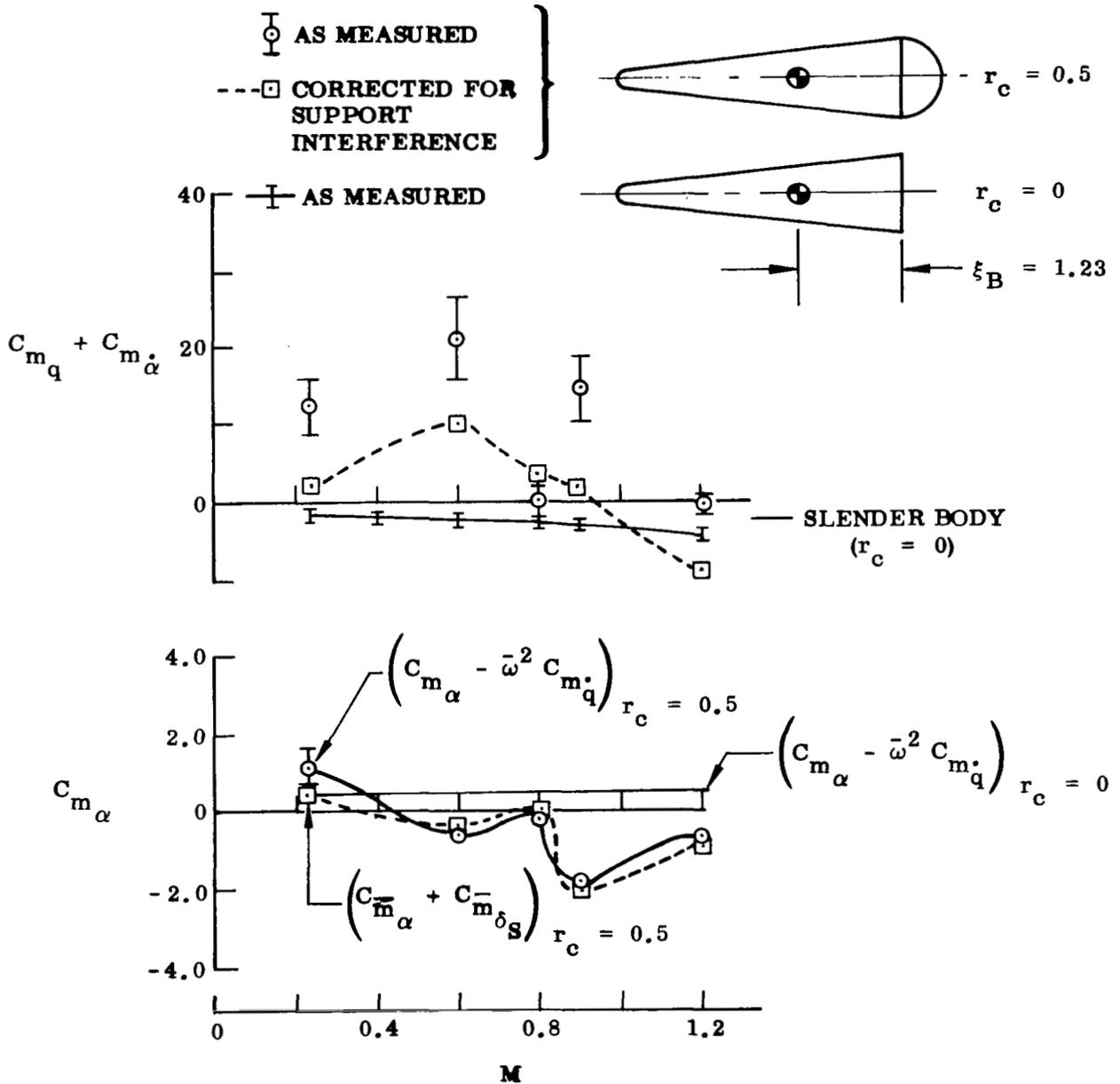
Fig. 52(b) Damping of Hemispherical Based Body with Support Interference Effects Eliminated, $\alpha = 0$, $\xi_B = 1.23$
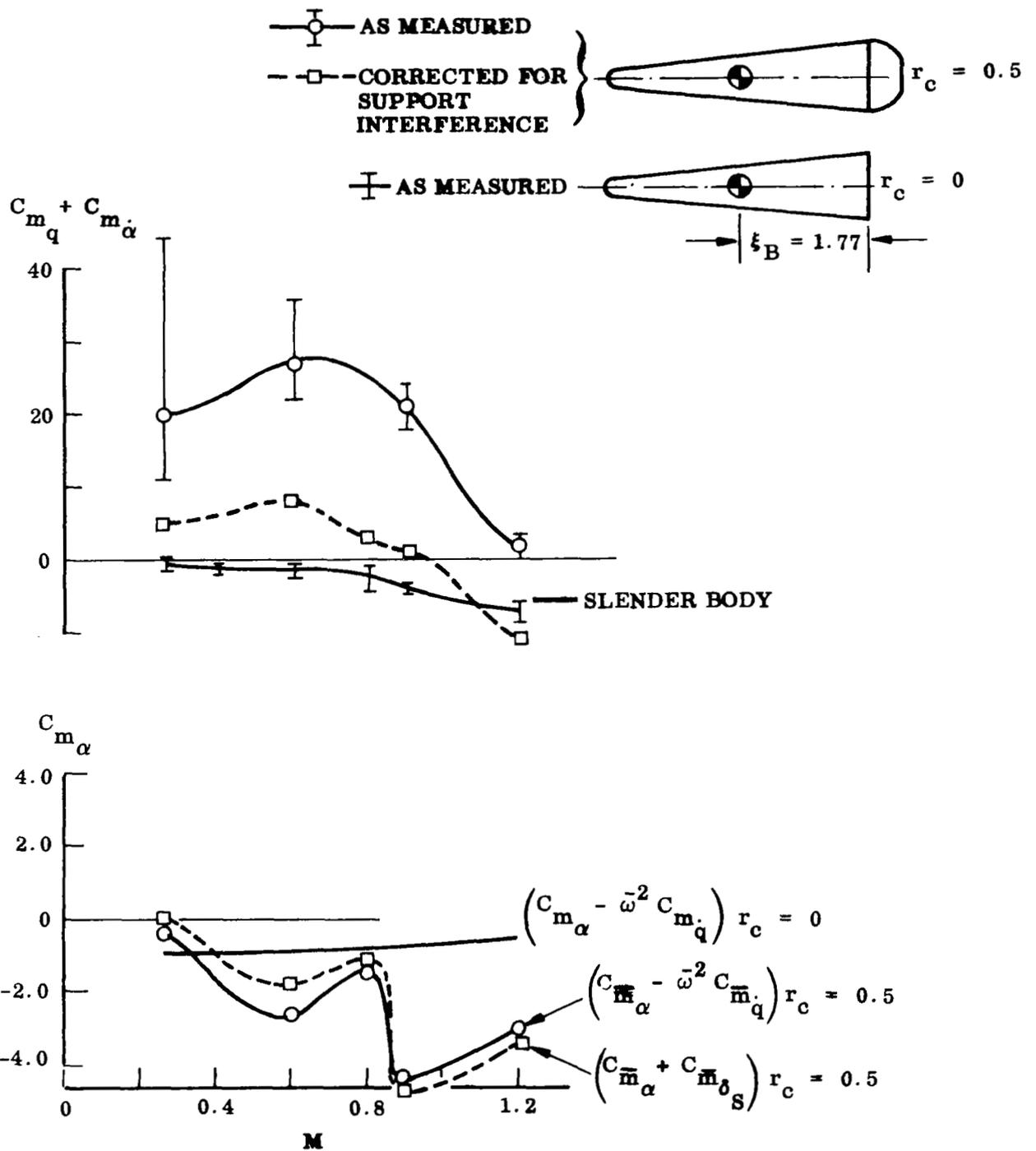
Fig. 52(c) Damping of Hemispherical Based Body with Support Interference Effects Eliminated, $\alpha = 0$, $\xi_B = 1.77$

96

support interference can be confidently accounted for, and even then, the application will be limited to configurations where the wake configuration and communication velocities do not differ too much from free wake values. Thus, much more research is needed before the effects of support interference on the dynamics of bulbous based bodies can be accounted for analytically.

Section 4

CONCLUSIONS

Much, if not all, of the anomalous behavior and poor dynamic stability of bulbous-based reentry bodies can be attributed to the effects of separated flow. Flow separation has the most drastic impact on the dynamic vehicle characteristics because of the time lag in the separated flow-field response to body cross flow perturbations. The time lag is also responsible for the observed reversal between static and dynamic effects of separation (i.e., statically-stabilizing effects are dynamically destabilizing, and vice versa). On blunt reentry capsules undamping effects are realized at supersonic speeds when the forebody wake begins to attach on the bulbous base. On slender reentry vehicles, undamping occurs at subsonic and transonic speeds for rounded bulbous-based geometries as a result of upstream communication from the wake recompression region. These latter effects will recur for hypersonic low density flows where upstream communication effects again become important. Since it is difficult to devise a support system that does not affect the wake flow, these configurations are plagued with support interference. An analytic means for eliminating the unwanted, and sometimes dangerously unconservative, effects of sting interference has been proposed which relates the static and dynamic effects of separation through quasi-steady theory. The fundamental assumption involved, which of course limits applicability, is that the support system does not alter the time lag within the wake too drastically. It remains yet to establish the limits of applicability of this technique.

Section 5
RECOMMENDATIONS FOR FUTURE STUDY

The various experimental results obtained on vehicles with bulbous bases vividly demonstrate that base roundness (convexity) has a profound effect, especially on vehicle dynamics. It is clear that the complexity of the flow pattern precludes any theoretical solutions for the unsteady aerodynamic effects of bulbous bases. Quasi-steady methods have been used to establish a relationship between the unsteady and the static characteristics. This technique may provide a means for correcting dynamic results for the effects of support interference. However, further research is necessary to develop the quasi-steady technique into an effective tool. It is suggested that static stability, dynamic stability, and time lag measurements be obtained on each of the three types of support system* (transverse rod, cylindrical sting, flared sting), and that support size be varied to determine the acceptable maximum size for quasi-steady application**.

Measurements of both the downstream and upstream time lags could be obtained from sting mounted forced oscillation tests by observing the fluctuating pressures at separation and re-attachment***. The phase lag between these pressure measurements and the model motion will define the convection velocities. The time lags so obtained will increase as support size is decreased, approaching the free wake value. Thus,

---

*It is further suggested that only symmetric support systems be used to avoid the difficulties inherent in asymmetric systems.
**The acceptable support size will of course vary with configuration.
***This technique is contingent upon the availability of acceleration insensitive transducers. This problem might be simplified by placing the rotation center at the center of the base radius, ensuring that all accelerations will be normal to the transducer axis. Flow visualization studies using oil flow and Schlieren could help determine optimum locations for the pressure transducers.

an indication of acceptable support size could be obtained. This information, coupled with static measurements of the support interference loads, will provide the necessary input data to the quasi-steady analysis. A similar approach would also be used for the transverse rod support.

It is further suggested that the wake be probed to obtain velocity profile measurements, aimed at developing a technique for predicting the convection velocities.

In summary, the following empirical information is needed to develop the quasi-steady technique to the point where it may be used to obtain interference-free dynamic stability measurements:

- Further forced oscillation dynamic stability measurements for the three support types (cylindrical sting, flared sting, and transverse rod support).
- Fluctuating pressure measurements concurrent with the forced oscillation data to define the wake convection velocity and maximum acceptable support size.
- Wake velocity profiles to correlate with the convection velocities.

It is felt that these results could define conclusively the source of the bulbous base instabilities and provide a technique for correcting experimental results for support interference.

Appendix A
NOMENCLATURE

c   reference length, m (c = maximum diameter or cylinder diameter on flared bodies)

D   diameter, m

d_S sting diameter, m (Fig. 39)

H   total pressure, kg/m^2

L   lift, kg/m^2 Coefficient, $C_L = L/\left(\rho_\infty U_\infty^2/2\right) S$

L_c dimensionless shoulder length (Fig. 22)

L_S sting length (Fig. 38)

M   Mach number

M   pitching moment, kg-m. Coefficient $C_m = M/\left(\rho_\infty U_\infty^2/2\right) Sc$

N   normal force, kg; Coefficient $C_N = N/\left(\rho_\infty U_\infty^2/2\right) S$

p   static pressure, kg/m^2; Coefficient $C_p = (p - p_\infty)/\left(\rho_\infty U_\infty^2/2\right)$ or $P = (p - p_\infty)/H_\infty$

q   pitch rate, rad/sec

R   Radius of curvature, m

R_c Reynolds number based on ref. length c

R_L Reynolds number base on vehicle length

r   radius, m

r_c dimensionless radius ($r_c = r/c$)

S   reference area, m^2 ($S = \pi c^2/4$)

t   time, sec

U   velocity, m/sec

w	upwash velocity, m/sec (Fig. 43)
x	axial coordinate, m (Fig. 44)
z	vertical coordinate, m (Fig. 44)
z_S	translatory sting displacement, m (Fig. 47)
α	mean angle of attack, rad or deg
$\bar{\alpha}$	projection of angular envelope $(\alpha + i\beta)$
$\Delta\alpha$	amplitude of pitch oscillation, rad or deg
β	angle of yaw, rad or deg
δ_S	sting deflection, rad or deg (Fig. 47)
Δ	difference
ζ	dimensionless z-coordinate $(\zeta = z/c)$
θ	pitch oscillation angle, rad or deg
θ_b	base surface slope (Fig. 46)
θ_c	cone half-angle, rad or deg
ξ	dimensionless x-coordinate $(\xi = x/c)$
ρ	air density, $kg\text{-}sec^2/m^4$
ϕ	wake displacement angle, rad or deg (Fig. 45)
ω	oscillation frequency, rad/sec
$\bar{\omega}$	reduced frequency $(\bar{\omega} = \omega c/U_\infty)$

Subscripts

A	Due to axial force (couple)
a and att	Attached flow
b	Base
B	Flat base trailing edge

B_s	Base separation
B_u	Upstream of base
c	Induced curvature
d	Downstream communication
e	Boundary layer edge
L	Limit of nonlinearity
N	Nose
p	Base plunging effect
R	Rod
RD	Dynamic rod interference
SC	Cylindrical sting
SF	Sting flare
SH	Cone cylinder shoulder
STD	Dynamic sting interference
STS	Static sting interference
TR	Boundary layer transition
u	Upstream communication
w	Wake communication effect
δ	Boundary layer build-up effect
∞	Undisturbed flow
1	Cone fore body (Fig. 44)
2	Cone aft body (Fig. 44)

Superscript

i   induced, e.g., $\Delta^{i}C_N$ = separation induced normal force coefficient

−   barred symbols, e.g. $C_{\bar{m}_\delta}$ indicated effective (weighted) average over a certain range

Differential Symbols

P_ξ $\partial P/\partial \xi$

$\dot{\alpha}$ $\partial \alpha/\partial t$

C_{m_α} $\partial C_m/\partial \alpha$

$C_{m_{\dot{\alpha}}}$ $\partial C_m\left/\partial \left(\dfrac{\dot{\alpha}c}{U}\right)\right.$

C_{m_q} $\partial C_m\left/\partial \left(\dfrac{qc}{U}\right)\right.$

$C_{m_{\dot{q}}}$ $\partial C_m\left/\partial \left(\dfrac{\dot{q}c^2}{U^2}\right)\right.$

C_{m_θ} $\partial C_m/\partial \theta$

$C_{m_{\dot{\theta}}}$ $\partial C_m\left/\partial \left(\dfrac{c\dot{\theta}}{U}\right)\right.$

$C_{\bar{m}_\theta}$ and $C_{\bar{m}_{\dot{\theta}}}$ are effective or integrated mean values for finite amplitudes ($\Delta \alpha \neq 0$ see Ref. 6)

REFERENCES

1. National Aeronautics and Space Administration, "Normal Force and Pitching Moment Characteristics for Two Blunt-Nosed Re-entry Type Bodies from M = 2.4 to M = 4.0," by C. E. DeRose, NASA Memo 2-4-59A, Feb 1959

2. -----, "Stability of Ballistic Reentry Bodies," by J. D. Bird and D. E. Reese, Jr., NASA RM L58E02a, Aug 1958

3. -----, "Wind-Tunnel Investigation of the Static and Dynamic Stability Characteristics of a 10° Semivertex Angle Blunted Cone," by W. R. Wehrend, Jr., NASA TN D-1202, Jan 1967

4. -----, "A Wind-Tunnel Investigation of the Effect of Changes in Base Contour on the Damping in Pitch of a Blunted Cone," by W. R. Wehrend, Jr., NASA TN D-2062, Nov 1963

5. Ballistic Research Laboratories, "Some Instability Problems with Re-entry Shapes," by MacAllister, BRL Memo Report No. 1224, Aug 1959

6. Lockheed Missiles & Space Company, "Separated Flow Effects on the Dynamic Stability of Blunt-Nosed Cylinder-Flare Bodies," by L. E. Ericsson, LMSC-667991, Contract NAS 8-5338, Sunnyvale, Calif., Dec 1965

7. -----, "Dynamics of Separated Flow Over Blunt Bodies," by L. E. Ericsson and J. P. Reding, LMSC 2-80-65-1, Contract NAS 8-5338, Sunnyvale, Calif., Dec 1965

8. L. E. Ericsson and J. P. Reding, "Analysis of Flow Separation Effects on the Dynamics of a Large Space Booster," J. Spacecraft and Rockets, 2, 1965, pp. 481−490

9. National Research Council of Canada, "Effect of Flare on the Dynamic and Static Moment Characteristics of a Hemisphere-Cylinder Oscillating in Pitch at Mach Numbers from 0.3 to 2.0," by J. G. LaBerge, Aeronautical Report LR-295, Jan 1961

10. National Aeronautics and Space Administration, "Some Static, Oscillatory, and Free-Body Tests of Blunt Bodies at Low Subsonic Speeds," by J. H. Lichtenstein, L. R. Fisher, S. H. Scher, and G. F. Lawrence, NASA Memo 2-22-59L, Apr 1959

11. -----, "Free-Flight Measurements of Static and Dynamic Stability of Models of the Project Mercury Re-entry Capsule at Mach Numbers 3 and 9.5," by S. C. Sommer, Barbara J. Short, and D. L. Compton, NASA TM X-373, Aug 1960

12. -----, "Damping in Pitch and Static Stability of Blunt Cone-Cylinder Flare Models and Manned Reentry Capsule Models for Various Angles of Attack at a Mach Number of 2.91," by H. S. Fletcher, NASA TM X-539, Jul 1961

13. -----, "The Damping in Pitch and Static Stability of Six Supersonic-Impact Ballistic Configurations and Three High-Drag Reentry Capsules at a Mach Number of 6.83," by H. S. Fletcher, NASA TM X-349, Jan 1961

14. -----, "Damping in Pitch and Static Stability of Supersonic Impact Nose Cones, and Manned Reentry Capsules at Mach Numbers from 1.93 to 3.05," by H. S. Fletcher and W. D. Wolhart, NASA TM X-347, Nov 1960

15. -----, "Damping in Pitch and Static Stability of a Group of Blunt-Nose and Cone-Cylinder Flare Models at a Mach Number of 6.83," by H. S. Fletcher and W. D. Wolhart, NASA Memo 5-6-59L, May 1959

16. -----, "Damping in Pitch and Static Stability of a Group of Blunt Bodies at Mach Numbers from 0.60 to 0.95," by H. S. Fletcher, NASA TM X-194, Dec 1959

17. -----, "Transonic Wind-Tunnel Measurements of the Damping in Pitch and Oscillatory Longitudinal Stability of Several Reentry Vehicles Having Low Lift-Drag Ratios," by R. A. Kilgore and W. C. Hayes, Jr., NASA TM X-609, Oct 1961

18. -----, "Low Subsonic Static and Dynamic Stability Characteristics of Two Blunt 120° Cone Configurations," by R. J. Bendura, NASA TN D-3853, Feb 1967

19. -----, "The Damping in Pitch of Bluff Bodies of Revolution at Mach Numbers from 2.5 to 3.5," by B. H. Beam and C. E. Hedstrom, NASA TM X-90, Oct 1959

20. J. P. Reding and L. E. Ericsson, "Loads on Bodies in Wakes, " J. Spacecraft and Rockets, 4, 1967, pp. 511—518

21. Lockheed Missiles & Space Company, "Forces Induced on Bodies in Free Wakes and Three-Dimensional Cavities," by J. P. Reding, LMSC-667990, Contract NAS 8-5338, Sunnyvale, Calif. , Dec 1965

22. Sandia Corporation, " A Compilation of Longitudinal Aerodynamic Characteristics Including Pressure Information for Sharp- and Blunt-Nose Cones Having Flat and Modified Bases, by A. D. Foster, SANDIA SC-R-64-1311, Jan 1965

23. -----, "Base and Surface Pressure Variation with Mach Number on a Right Circular Cone," by J. D. Iversen, SANDIA SCTM 202-56-51, 12 Sep 1956

24. Arnold Engineering Development Center, "Characteristics of Steady-State Pressures on the Cylindrical Portion of Cone-Cylinder Bodies at Transonic Speeds," by J. E. Robertson and H. L. Chevalier, AEDC TDR-63-104, Aug 1963

25. Lockheed Missiles & Space Company, "Steady and Unsteady Terminal Shock Aerodynamics on Cone-Cylinder Bodies," by L. E. Ericsson, LMSC L-87-67-2, Contract NAS 8-20354, Sunnyvale, Calif. , Oct 1967

26. L. E. Ericsson and P. Woods, "Aeroelastic Considerations in a Slender, Blunt-Nose Multistage Rocket," Aerospace Eng. , Vol. 21, 1962, pp. 42—51

27. L. E. Ericsson, "Aerolastic Instability Caused by Slender Payloads," J. Spacecraft and Rockets, 4, 1967, pp. 65—73

28. Lockheed Missiles & Space Company, "The Aerolastic Characteristics of the Saturn IB Launch Vehicle with Biconic Payload Shroud," by L. E. Ericsson, N. J. French, and R. A. Guenther, LMSC M-37-67-1, Contract NAS 8-20354, Sunnyvale, Calif. , Apr 1967

29. National Aeronautics and Space Administration, "Dynamic Directional Stability Characteristics for a Group of Blunt Reentry Bodies at Transonic Speeds," by H. G. Wiley, R. A. Kilgore, and E. R. Hillje, NASA TM X-337, Oct 1960

30. Arnold Engineering Development Center, "Dynamic Stability Tests of the Advanced Mark 6 Re-Entry Vehicle at Mach 10," by L. K. Ward and A. E. Hodapp, AEDC TDR 62-198, Oct 1962

31. L. K. Ward, "Influence of Boundary-Layer Transition on Dynamic Stability at Hypersonic Speeds," Transactions of the Second Technical Work Shop on Dynamic Stability Testing, Vol. II, Paper 6, 20-22 Apr 1965

32. F. R. Hama, "Experimental Studies on the Lip Shock," AIAA Paper No. 67-29, AIAA 5th Aerospace Sciences Meeting, New York, N. Y., 23–26 Jan 1967

33. L. E. Ericsson and J. P. Reding, "Ablation Effects on Vehicle Dynamics," J. Spacecraft and Rockets, 3, 1966, pp. 1476–1483

34. National Aeronautics and Space Administration, "Boundary-Layer Measurements in Accelerated Flows Near Mach 1," by H. L. Wesoky, NASA TN D-3882, Mar 1967

35. L. E. Ericsson and J. P. Reding, "Effect of Boundary Layer Transition on Vehicle Dynamics," AIAA 7th Aerospace Sciences Meeting, New York, N. Y., Jan 20–22, 1969

36. J. W. Cleary, "Effects of Angle of Attack and Nose Bluntness on the Hypersonic Flow Over Cones," AIAA Paper No. 66-414, AIAA 4th Aerospace Science Meeting, Los Angeles, Calif., 27–29 Jun 1966

37. E. J. Softley, B. C. Graber, and R. E. Zempel, "Experimental Observation of Transition of the Hypersonic Boundary Layer," Paper 68–39, AIAA 6th Aerospace Sciences Meeting, New York, N. Y., Jan 22–24, 1968

38. Lockheed Missiles & Space Company, "Preliminary Experimental Investigation of Separated Flow Loads on Cone Cylinder Flare Bodies," by R. A. Guenther and J. P. Reding, LMSC L-87-67-1, Contract NAS 8-20354, Sunnyvale, Calif., Feb 1967

39. L. E. Ericsson, "Effect of Nose Bluntness on the Hypersonic Unsteady Aerodynamics of an Ablating Reentry Body," J. Spacecraft and Rockets, 4, 1967 pp. 811–813

40. Jet Propulsion Laboratory, "Optical Free-Flight Wake Studies," by Bain Dayman, Jr., Technical Report No. 32-364, Nov 1, 1962

41. Lockheed Missiles & Space Company, "Partial Simulation of Elastic-Body Dynamics for the Upper-Stage Apollo-Saturn Launch Vehicle, by J. Peter Reding LMSC M-37-67-4, Contract NAS 8-20354, Sunnyvale, Calif., Dec 1967

42. W. G. Clay, R. E. Slattery, and R. R. Stevens, "Interactions Between a Hypersonic Wake and a Following Hypersonic Projectile," AIAA J. Vol. 1, Apr 1963, pp. 974−975

43. National Aeronautics and Space Administration, "An Investigation of the Static and Dynamic Aerodynamic Characteristics of a Series of Blunt-Nosed Cylinder Flare Models at Mach Numbers from 0.65 to 2.20," by D. E. Reese, Jr., and W. R. Wehrend, Jr., NASA TM X-110, Jan 1960

44. D. M. Jecmen, J. P. Reding, and L. E. Ericsson, "An Application of Automatic Carpet Plotting to Wind-Tunnel Data Reduction," J. Spacecraft and Rockets, 4, 1967, pp. 408−410

45. Lockheed Missiles & Space Company, "Carpet Plot Program" by D. M. Jecmen, LMSC-805634, Jan 1967

46. J. P. Reding, R. A. Guenther, L. E. Ericsson, and A. O. Leff, "Experimental Evidence of the Nonexistence of Axisymmetric Separated Flow," to be submitted for publication as a Technical Note in the AIAA Journal.

47. Hypersonic Sting Interference. Private communication, Otto Walchner, ARL, Jun 3, 1968

48. James T. Clay and O. Walchner, "Nose Bluntness Effects on the Stability Derivatives of Cones in Hypersonic Flow," Trans. of the Second Technical Work Shop on Dynamic Stability Testing, Volume 1, Paper 8. Arnold Engineering Development Center, Arnold Air Force Station, Tennessee, Apr 20−22, 1965

49. National Aeronautics and Space Administration, "An Experimental Evaluation of Aerodynamic Damping Moments of Cones with Different Centers of Rotation," by W. R. Wehrend, Jr., NASA TN D-1768, Mar 1963

50. Lockheed Missiles & Space Company, "Effect of Sting Stiffness on Measured Derivatives for Model Describing Pitch Oscillations of Low Reduced Frequencies," by L. E. Ericsson, DP/M-TN-27, LMSD-800385, Dec 1960

51. Arnold Engineering Development Center, "Transonic Static and Dynamic Stability of Several Saturn IB and Saturn V Upper Stage Configurations," by R. L. Lowndes and T. O. Shadow, AEDC TR-66-125, Tullahoma, Tenn. Jun 1966

52. California Institute of Technology – Jet Propulsion Laboratory, "Simplified Free-Flight Testing in a Conventional Wind Tunnel," by B. Dayman, Jr., CIT-JPL TR 32-346

53. W. W. Speaker and C. M. Ailman, "Static and Fluctuating Pressures in Regions of Separated Flow," AIAA Preprint 64-456, AIAA 4th Aerospace Sciences Meeting, Los Angeles, Calif., 27–29 Jun 1966

54. A. L. Kistler and W. S. Chen, "The Fluctuating Pressure Field in a Supersonic Turbulent Boundary Layer," Jet Propulsion Laboratory, California Institute of Technology, TR 32-277 Aug 1962

55. Lockheed Missiles & Space Company, "Some Thoughts About Dynamically Destabilizing Effects Caused by Separated Flow on Hammerhead Boat-Tails at Transonic Speeds," by L. E. Ericsson, LMSC TM-57-11-27, Dec 1961

56. P. Wood and L. E. Ericsson, "Aerodynamic Considerations in a Slender Blunt-Nose, Miltistage Rocket," Aerospace Engineering, 21, pp. 42–51 May 1962

57. National Aeronautics and Space Administration, "Wind-Tunnel Investigation of a Balloon as a Towed Decelerator at Mach Numbers from 1.47 to 2.50," by J. T. McShera and J. W. Keyes, NASA TND-919, Aug 1961

58. National Advisory Committee for Aeronautics, "Heat Transfer and Recovery Temperatures on a Sphere with Laminar, Transitional, and Turbulent Boundary Layers at Mach Number of 2.00 and 4.15," by I. E. Beckwith and J. J. Gallagher, NACA TN 4125, Dec 1957

59. National Aeronautics and Space Administration, "Aerodynamic Characteristics of Spherically Blunted Cones at Mach Numbers from 0.5 to 5.0," by R. V. Owens, NASA TND-3088, Dec 1965